UNIVERSITY OF SOUTHAMPTON

FACULTY OF PHYSICAL SCIENCES AND ENGINEERING

Electronics and Computer Science

Doping Controlled Resistive Switching Dynamics in Transition Metal Oxide Thin Films

by

Maria Trapatseli

Supervisor: Professor Themistoklis Prodromakis

Thesis for the degree of Doctor of Philosophy

August 2018

UNIVERSITY OF SOUTHAMPTON

ABSTRACT

FACULTY OF PHYSICAL SCIENCES AND ENGINEERING
Electronics and Computer Science

Doctor of Philosophy

DOPING CONTROLLED RESISTIVE SWITCHING DYNAMICS IN TRANSITION METAL OXIDE THIN FILMS

by Maria Trapatseli

Transition metal oxide thin films have attracted increasing attention due to their potential in non-volatile resistive random access memory (RRAM) devices, where such thin films are used as active layers in metal-insulator-metal (MIM) configurations. Titanium dioxide is one of the most celebrated oxides among the ones that exhibit resistive switching behaviour due to its wide band gap, high thermal stability, and high dielectric constant. RRAM devices with various materials as active layers, have demonstrated very fast switching performance but also huge potential for miniaturisation, which is the bottleneck of FLASH memory. Nevertheless, these devices very often suffer poor endurance, physical degradation, large variability of switching parameters and low yields. In most cases, the physical degradation stems from high electroforming and switching voltages. Doping of the active layer has been often employed to enhance the performance of RRAM devices, like endurance, OFF/ON ratio, forming voltages, etc. In this work, doping in TiO_{2-x} RRAM devices was used to engineer the electroforming and switching thresholds so that device degradation and failure can be delayed or prevented. Al and Nb were selected with basic criteria the ionic radius and the oxidation state. The doped RRAM devices, showed improved switching performance compared to their undoped counterparts. Alternative approaches to doping were also investigated, like multilayer stacks comprising Al_2O_{3-y} and TiO_{2-x} thin films. Furthermore, Al:TiO_{2-x}/Nb:TiO_{2-x} bilayer RRAM devices were fabricated, to prove whether a diode behaviour of the p-n interface inside the RRAM was feasible. The latest would be a particularly interesting finding towards active electronics.

Contents

List of Figures

List of Tables

List of Acronyms

AFM	Atomic Force Microscopy
ARXPS	Angle-Resolved X-ray Photoelectron Spectroscopy
C-AFM	Conductive Atomic Force Microscopy
ALD	Atomic Layer Deposition
CMOS	Complementary Metal Oxides
DOS	Density of States
DRAM	Dynamic Random Access Memory
DUT	Device Under Testing
ECM	Electrochemical Metallization Memory
EOT	Equivalent Of Thickness
FeRAM	Ferromagnetic Random Access Memory
FIB	Focused Ion Beam
HRS	High Resistive State
LRS	Low Resistive State
MIM	Metal-Insulator-Metal
MOCVD	Metal Organic Chemical Vapor Deposition
NAND	Negated AND or NOT AND gate
PLD	Pulsed Laser Deposition
PPR	Programming Pulse Ramp
PPT	Programming Pulse Train
ReRAM	Redox-based Random Access Memory
RRAM	Resistive Random Access Memory
SEM	Scanning Electron Microscopy
STEM	Scanning Tunnelling Microscopy
TMO	Transition Metal Oxide
VCM	Valence Change Memory
XPS	X-ray Photoelectron Spectroscopy

Acknowledgements

As the author of this thesis, I would like to thank my PhD advisor Dr Daniela Carta for her help and guidance in delivering this thesis. Her help was particularly appreciated for reviewing my papers and giving me always the best advice that successfully led to a rich publication list in highly reputable journals. I am grateful to Dr Ali Khiat for the knowledge transfer for the RRAM device fabrication and to Dr Alex Serb for the guidance with the electrical characterisation of the devices as well as for the fruitful discussions. Their feedback on my manuscripts was crucial and increased their quality but also was a very good lesson for improving my technical writing. I would also like to thank my fellow PhD student Simone Cortese for the exchange of ideas and the useful discussions related to device physics. I wouldn't have made it to the end without the dedication and support of my closest friends and fellow PhD students: Dimitrios Alanis, Isha Gupta, Marilena Rizou, Ilaria Sanzari and Eleni Chatzikuriakou. This journey was not an easy one and there were several occations where my limits were tested. I will be forever greatful to my parents and especially to my mother, Eirini and my sister, Flora for being on my side in all moments of this journey. I would also like to thank my supervisor Prof Prodromakis for showing me trust and for his daily input and guidance during this PhD programme. Finally, the financial support of the EPSRC EP/K017829/1 and EU-FP7 RAMP funds is gratefully acknowledged.

To my grandparents, Maria, Flora and Dimitris for having faith in me. I would not have made it without your unconditional love and support.

Chapter 1

Introduction

1.1 Motivation

Titanium dioxide thin films have been extensively studied for their application in nano-electronics [1, 2, 3], energy [4, 5, 6], photocatalysis [7], and storage [8, 9, 10]. More recently, TiO_2 thin films were also employed in resistive random access memory (ReRAM) cells, serving as active layers sandwiched between two metal electrodes in metal–insulator-metal (MIM) stacks [8]. Due to their simple structure, ReRAM cells can be easily incorporated into single devices or crossbar arrays, of various sizes and shapes. These devices have shown good performance in power consumption, high density integration and high speed operation [10]. Although these devices have shown the capacity to become competitive in the field of future nano–electronics, they still encounter low yields and failure [11, 12].

Common reasons of failure are: poor endurance [13], physical degradation [14, 15], large variability of switching parameters [16] and low yields. Poor endurance is what makes the two resistive states no longer possible to be distinguished, even after few tenths of cycles only. Physical degradation refers to physical changes on the device architecture, such as bumps, cracks or bubble-like features, usually on the top-electrode. Examples of such physical degradation are shown in figure 1.1. These can be a result of high power operation, but often they show up in the beginning of the device operation and they slowly proliferate until the device is unresponsive to any kind of input. Large variability is a major obstacle to a mass production of such devices, as often they show significant variability of switching voltages or switching behaviour. This variability can be also related to variability in active layer thickness, inhomogeneous oxide/metal deposition and varying electrode length. Poor yields are often occurring for no obvious reason, but in many cases are associated with a fabrication step, such as, post-fabrication annealing which can lead in electrode shorting.

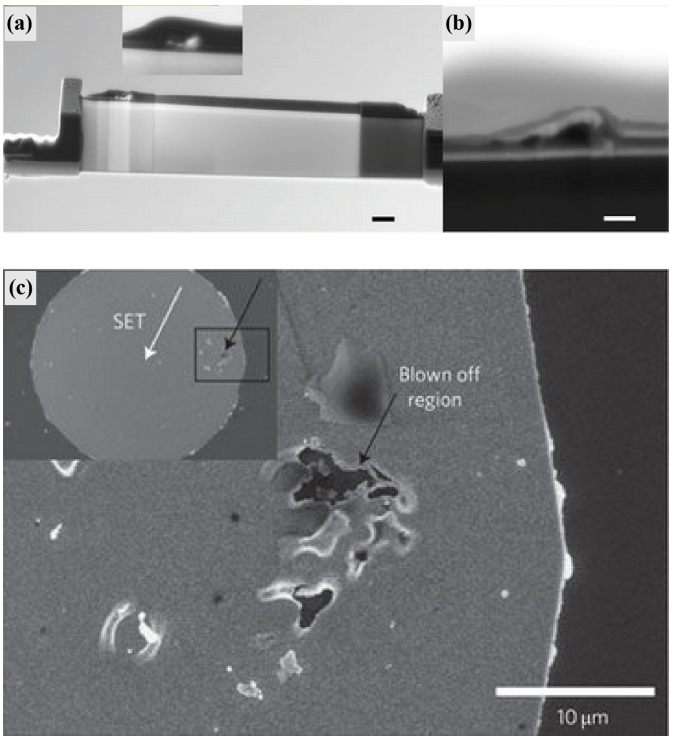

Figure 1.1: Examples of physical deformations on device structures (a), (b) by Carta *et al.* and (c) by Kwon *et al.*

The term soft breakdown (SB) [17], is often used to describe the initiation of the device operation and it is associated with the formation of conductive filaments (CFs) inside the device active layer [18]. When a soft breakdown occurs, an abrupt increase of current is observed and the device can toggle between a high resistive state (HRS) and a low resistive state (LRS) with the application of an appropriate electrical stimulus. However, no major physical deformation of the top electrode is observed. The hard breakdown (HB), is caused by high voltages and is generally responsible for the device failure due to physical deformations emerging on the device structure [19].

Devices operating in SB regime maintain their last assumed state through subsequent low-voltage (below switching threshold) sweeps. When applying very high voltage or when performing a large number of switching cycles the device enters the HB region and finally fails. In HB, the device may still be able to switch electrically, but this is accompanied by the formation and proliferation of protrusions on the top electrode, similar to those in figure 1.1. The protrusions accumulate irreversibly until the device fails completely, that is, becomes unable to switch electrically. These dramatic events can cause permanent failure of devices. The identification and control of the SB and HB voltage thresholds could benefit the device operation in a way so that switching commences in a "safe" for the device voltage range.

The switching dynamics and the SB and HB voltage thresholds could be realised as

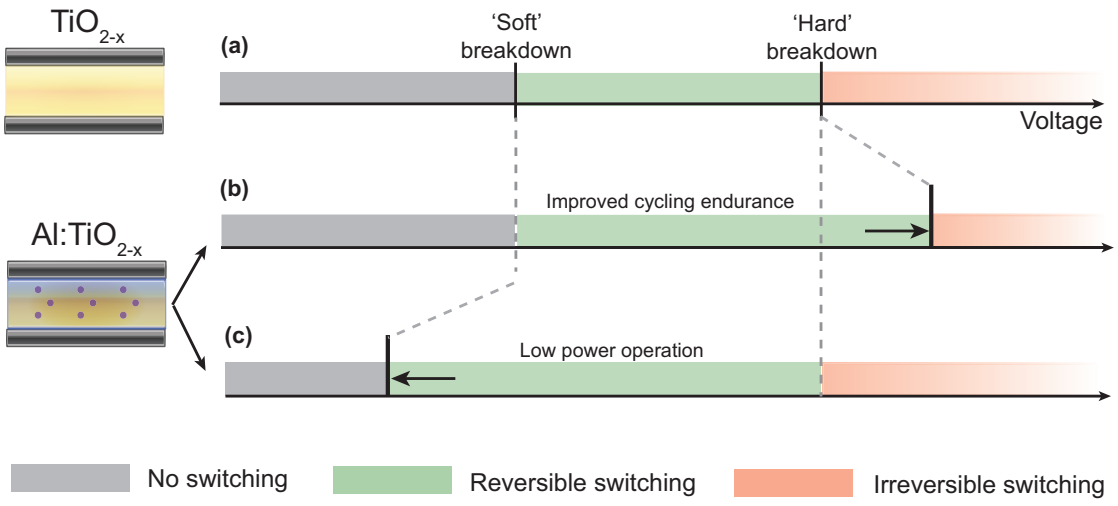

Figure 1.2: (a) Concept of resistive switching dynamics in TiO_{2-x}-based RRAM cells and (b), (c) a suggestion of their SB and HB voltage threshold modification with doping.

in figure 1.2. Three major areas can be identified: a neutral zone (shown in gray) corresponding to application of very low voltages that are not sufficient to alter the devices resistance, a "reversible switching" zone (shown in green) corresponding to a higher voltage range where the device operates reliably and an irreversible switching zone at higher voltages where switching causes irreversible changes to devices architecture and leads to permanent failure. Figures 1.2b, c display the potential improvement in device performance with doping. The active layer can be engineered to lower the SB voltage threshold (key for low-power operation) and to increase the HB voltage threshold (key for enhanced endurance and reliability) [17, 20, 21]. The electroforming that does not create visible changes in the device topography is considered a soft-breakdown, but a high-voltage electroforming that creates visible physical deformation of the device is considered a hard-breakdown.

In this context, this thesis was built around the optimisation of the device switching parameters, mainly switching thresholds, to prevent failure and increase the device reliability and switching repeatability.

1.2 Research Objectives

So far, SB and HB thresholds could only be identified in device level by conventional switching, fact that made the monitoring of the oxide impossible. Studying the resistive switching (RS) phenomena in thin film level is often preferred as it makes it easier to interpret the changes in topography and resistivity. At the beginning, a major part of this work was invested in identifying the SB and HB regimes without the requirement

of a finished solid-state RRAM device. This was realised through Conductive Atomic Force Microscopy (C-AFM) measurements on TiO_{2-x} thin films, where the AFM tip played the role of an active layer. Although electrical stimulation of thin films using C-AFM can not be considered directly comparable to resistance switching in thin films, the effect was very similar and useful information was collected concerning the SB and HB breakdown regimes. This part was successfully published in Journal of Physical Chemistry C [22].

Following that stage, the focus turned towards TiO_{2-x} ReRAM devices and engineering their switching thresholds via doping with Al. Al was selected with oxidation state and ionic size criteria. The objective was, firstly, to develop doped and undoped TiO_{2-x} ReRAM devices and secondly, to perform back-to-back electrical characterisation and demonstrate the improvement of the devices' switching dynamics. Intermediate steps towards that direction, involved TiO_{2-x} oxide thin films deposition by reactive sputtering and elemental characterisation by X-ray Photoelectron Spectroscopy (XPS). Devices with desired Al % at. were selected and tested back-to-back with their undoped counterparts, to verify the improvement in switching performance.

In the next stage, an alternative approach to doping was followed and ultra -thin Al_2O_{3-y} buffer layers were incorporated between TiO_{2-x} thin films. The purpose was to investigate whether Al is incorporated in the TiO_{2-x} thin films and if it is improving the switching dynamics, by decreasing the electroforming (EF) and switching voltages. Moreover, the mechanism of switching was studied and a possible explanation on the effect the ultra-thin Al_2O_{3-y} layers have on the device's switching mechanism.

Finally, the last stage involved an effort in making the ReRAM devices showing a diode-like behaviour. Such a contribution which is still missing from the literature, would realise ReRAM cells in more applications, like amplifiers and switches. Based on the argument that Al would induce a p-type conductivity in TiO_{2-x}, Nb was selected as a n-type dopant. TiO_{2-x} thin films individually doped with Al and Nb, were deposited by reactive sputtering and characterised by XPS. Characterisation of the type of carriers was not possible by Van der Pauw method, due instrument limitations. Bilayer devices comprising Al- and Nb-doped thin films were fabricated and tested for their switching characteristics. The DC electrical tests did not validate a diode-like behaviour but a typical for ReRAM abrupt electroforming and hysteretic I-V signature. The Nb-doped and bilayer devices exhibited improved switching with lower electroforming and switching voltages. Some preliminary retention tests were also carried out to evaluate their capability of maintaining the resistance states.

Overall, this work was developed around amorphous TiO_{2-x} as a model oxide for ReRAM applications. The aim was to prove that engineering of the active layer using foreign elements (dopants) and alternative methods, is feasible and can have a positive impact on the device performance without additional sophisticated processing. Furthermore,

TiO_{2-x} was an ideal oxide to study stages of the resistive switching mechanism by engineering its chemical composition, as it is easy to deposit under room temperature, stable when combined with foreign elements and maintains a uniformity when deposited on other oxides, such as Al_2O_{3-y} thin films.

1.3 Report Outline

The thesis outline is as follows:

(a) In chapter 2, the state-of-art in RRAM devices is summarised with respect to the employed materials as active layers. Additionally, it comprises the most recent progress in TiO_2 RRAM devices doped with foreign elements, methods of fabrication and performance improvements. Also, the chapter briefly discusses the use of C-AFM as a method for studying the resistive switching phenomena on oxide thin films.

(b) In chapter 3, the fabrication and testing of TiO_2 ReRAM devices doped with Al, are presented. The effect of Al doping in the devices' switching dynamics is discussed.

(c) In chapter 4, Al_2O_{3-y} thin films are incorporated in TiO_2 ReRAM devices as an alternative aproach to doping. Results from the electrical characterisation of the devices are presented and insight on the switching mechanism is provided.

(d) In chapter 5, the fabrication and characterisation of bilayer ReRAM devices comprising TiO_2 thin films with Al and Nb dopants, respectively, is presented and discussed. The aim was to create oxide interfaces that behave like diodes. Typical ReRAM device characterisation is carried out and discussed.

(e) Finally, chapter 6 summarises all contributions of this work and potential future research.

Chapter 2

Resistive Random Access Memory (RRAM)

This chapter gives a brief introduction about non-volatile RRAM. It also includes a classification of the state-of-art RRAM devices with respect the active layer material. Finally, the most recent advances of doping in RRAM devices is presented towards the end of the chapter, along with a brief report in C-AFM studies for RRAM applications.

2.1 Introduction

Leon Chua reported in 1971 the existence of the memristor, postulated as the fourth fundamental circuit element after the resistor, the capacitor and the inductor [23]. The memristor behaves like a memory device as when the electric power is disconnected, it remembers the most recent resistance until it is connected again. The memristors attracted again the interest of the scientific community after 2000 when Beck *et al.* [24] reported reproducible switching effects in perovskite thin oxide films with notable potential in non-volatile memory applications. A RRAM device can be considered as a specific type of memristor because it displays memristive behaviour: ie. it can toggle between two or more resistance states when appropriate electrical stimulus is applied. The term RRAM first appeared in a paper by Zhuang *et al.* [25] in 2002 where they reported a 64-bit RRAM array fabricated by a CMOS process. Two key papers regarding non-volatile RRAM came out in the following years from Baek *et al.* [26] and Strukov *et al.* [27] respectively. The first reported the development of fully CMOS compatible and highly scalable RRAM devices and it was the first advanced work regarding RRAM with binary transition metal oxides (TMOs). The second presented a physical model of a two-terminal electrical device that behaves like a perfect memristor and this was the first time that memristor concept was applied to RRAM devices.

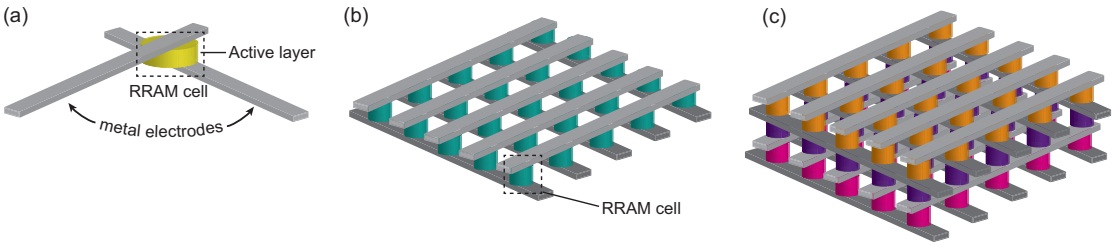

Figure 2.1: Three RRAM cell architectures with different densities:(a) a standalone crossbar (b) a crossbar array and (c) a 3D-stack of crossbar arrays.

The RRAM memory cell has a capacitor-like configuration (Figure 2.1a) with an insulating or semiconducting oxide layer sandwiched between two metal electrodes. The oxide layer that is initially in a high resistive state (HRS) can switch to a low resistive state (LRS) under the application of an electric field. More precisely, the oxide layer can toggle between two or more distinct resistive states when appropriate bias is applied. The switching from a HRS to a LRS is called SET operation, while the opposite is called RESET. The switching behaviour can be categorized either as unipolar (non-polar) or bipolar [28]. When both SET and RESET occur at the same voltage polarity, then the switching is called unipolar. Alternatively, when SET occurs in reverse voltage polarity from that of RESET then the switching is called bipolar [29]. The mode of switching can be influenced by various factors like the electrode and/or the active layer material.

RRAM devices can be developed in different structures in order to increase the density of the devices. The most frequently used ones, standalone crossbars and crossbar arrays, are illustrated in Figure 2.1a,b. However, the need for higher density leads to the development of 3-D stacked arrays like the one in Figure 2.1c. The electrodes are preferably made from noble metals like Cu, Ru, Ag, Ir, Pt and Au, due to their non-corrosive, non-oxidizing and non-reactive nature along with the high diffusivity and solubility of oxygen in them [30]. However, in many cases electrodes are made from materials like Al, Ti, Ni, W and TiN depending on the active layer oxide [31] and the RRAM system that has to be achieved. In some systems, the electrode metal is "active", as it diffuses in the active layer and actively becomes part of the resistance switching process, like Al and Ni. In some other systems the electrode metal is inert and does not diffuse or react, like Ti, Au and Ru.

Regarding the active layer, there is a wide variety on the elements that are used to form either complex (perovskite) or binary oxides. The binary oxides that have attracted much interest in the latest years are transition metal oxides like: TiO_x, ZrO_x, HfO_x, VO_x, NbO_x, TaO_x, WO_x, NiO_x, FeO_x, MnO_x, ZnO_x, CuO_x, poor metal oxides like: AlO_x, GaO_x, BiO_x, SnO_x, Metalloid oxides like: SiO_x, GeO_x and SbO_x. Rare earth metal oxides like: TO_x, CeO_x, SmO_x, EuO_x, GdO_x, PrO_x, ErO_x, DyO_x and NdO_x have been also studied lately for their resistive switching behaviour. From perovskite

oxides, $SrTiO_3$ (STO), $Pr_{0.7}Ca_{0.3}MnO_{0.3}$ (PCMO), $Ba_{0.7}Sr_{0.3}TiO_3$ (BSTO), $SrZrO_3$, $BiFeO_3$ and $SrRuO_3$ are the most commonly used ones in RRAM devices [9, 32]. The early transition metals are particularly good candidates for RRAM applications because they form a variety of oxygen-deficient phases and facilitate the resistance switching mechanism (such Ti, Ta and Nb). Table 2.1 highlights the oxides with the state-of-art RRAM performance.

2.2 State-of-art RRAM devices

Non-volatile memories should display features such as low cost and high density, low switching speed, low operation energy, great endurance and retention characteristics. The attributes that a competitive RRAM device should have assuming memory applications, are presented in the following paragraphs. Table 2.1 summarises RRAM devices comprising transition metal oxides (including some non-TMO oxides) with the most outstanding performance for future memory applications.

Table 2.1: Summary of the state-of-art in RRAM devices, classified according to their endurance, retention, low power, OFF/ON ratio, speed and CMOS compatibility.

Modality	*Year*	*Author*	*Material*	*Attribute*
Endurance	2011	Lee *et al.*[33]	TaO_x	$>10^{12}$ switching cycles
	2010	Yang *et al.*[34]	TaO_x	1.5×10^9 switching cycles
	2008	Wei *et al.*[35]	TaO_x	10^9 cycles
	2014	Stevens *et al.*[36]	TaO_x	10^5 cycles
	2010	Lai *et al.*[37]	WO_x	10^8 cycles
	2011	Kim *et al.*[38]	WO_x	10^7 cycles
	2013	Zhou *et al.*[39]	HfO_x	$>10^6$ cycles
	2013	Cheng *et al.*[40]	TiO_x	10^6 cycles
Retention	2008	Wei *et al.*[35]	TaO_x	$>10^3$ hours at 150°
	2011	Chien *et al.*[41]	WO_x	10 years at 150°
	2010	Lee *et al.*[42]	HfO_x	$>10^6$ s at 200°
	2013	Zhou *et al.*[39]	HfO_x	$>10^4$ s at 25°
Low power	2012	Pickett *et al.*[43]	NbO_x	100 fJ
	2012	Zhang *et al.*[44]	HfO_x	$50nA/0.18\mu W 1.25nA/1.625\mu W$
	2010	Lee *et al.*[42]	HfO_x	operation current $< 200\mu A$
	2011	Chien *et al.*[41]	WO_x	reset/set at 1.8 V/-1 V
OFF/ON ratio	2014	Zhong *et al.*[45]	SiC	10^6
	2013	Wu *et al.*[46]	AlO_x	10^5
Switching Speed	2012	Pickett *et al.*[43]	NbO_x	set/reset at 700 ps/2.3 ns
	2011	Torrezan *et al.*[47]	TaO_x	set/reset at 105 ps/120 ps
	2011	Lee *et al.*[33]	TaO_x	$<10ns$
	2010	Lee *et al.*[42]	HfO_x	$<10ns$
CMOS Compatibility	2012	Zhang *et al.*[44]	HfO_x	PVD deposited active layer
	2011	Huang *et al.*[48]	SiO_x	PECVD deposited active layer
	2011	Chien *et al.*[41]	WO_x	RTO of the W plug
	2011	Hermes *et al.*[49]	TiO_x	reactive sputtering of TiO_x
	2008	Wei *et al.*[35]	TaO_x	RF reactive sputtering of TaO_x

A RRAM cell can be switched between HRS and LRS frequently, but each operation can introduce permanent damage, normally referred to as degradation. Endurance, also called electric fatigue, is the number of SET/RESET cycles that can be endured before HRS and LRS are no longer distinguishable. In order for RRAM to compete FLASH memory that shows a maximum number of write cycles between 10^3 and 10^7, it has to demonstrate at least equal endurance or preferably a better one [31]. A data retention time of >10 years is essential for non-volatile memories. This retention time must be kept at thermal stress up to 85°C and small electrical stress such as a constant stream of

read pulses [31]. The high current level is directly related to the high energy consumption for each switching cycle. Hence, lower operation voltages are preferred as this makes the device more efficient from the perspective of power consumption.

In RRAM devices, a good indication of the data capacity is given by the distinction between the two resistive states. In other words, the higher the ON/OFF resistance ratio is, the larger the memory window and the better performance the device will have. High switching speed can be advantageous for a non-volatile RRAM. CMOS compatibility is an important issue, especially when it comes to hybrid CMOS/memristor circuits. A process is considered to be CMOS compatible when the materials involved are already available in a CMOS process and when the temperatures employed are within the CMOS thermal budget (typically $\sim$ 400 °C). Concerning RRAM devices, they have to operate within a bearable range of voltages for CMOS, which is below 3.3 V in order to consider them as CMOS compatible. As the memory devices become smaller, the oxide thin film thickness subsequently becomes smaller which makes them more sensitive to the electrostatic field strength. Therefore, the operation voltage needs to lower even more to ensure more reliable operation.

2.3 Doping of active layer in RRAM devices

The introduction of controlled amounts of impurity dopants into semiconductors has been extensively used in nanoelectronics in order to alter the properties of a material and make it suitable for a specific application. Doping bulk materials like powders can be straightforward, while doping thin films can be more complicated because of the difficulty to control thickness and dopant gradient distribution [50]. Many research groups exploited doping in order to adjust the band gap of metal oxides (particularly TiO_text2) and improve its photocatalytic performance [51, 52, 53]. Other research groups employed doping as an effective approach to modify the electronic properties of oxide materials which is crucial in nanoelectronics [54, 55, 56]. It has been demonstrated that doping can be beneficial for non-volatile memories as it can enhance the endurance and the switching stability of the devices. One of the causes of the switching instability in RRAM devices is the random formation of conductive filaments [16, 57]. Doping has demonstrated the capacity to reduce the variability and switching voltages in HfO_2 and ZrO_2 RRAM devices [58, 59]. Hence, investigating doping effect on the behaviours of intrinsic defects is believed to shed light on the mechanism of the doping influence on resistive switching and provide possible solutions for controlling RRAM performance.

There are two key methods of doping, diffusion and ion implantation [60]. During diffusion, the dopant atoms are introduced on or near the surface of the film either by deposition from gas phase of the dopant or from a doped oxide source. As a process, diffusion is the net movement of a substance (an atom, ion or molecule) from an area

of high concentration to an area of low concentration. Usually, it is a very slow process and it can take days or even months for a dopant to distribute evenly in a material. The dopant atoms must be highly "soluble" in a particular material to make the doping process feasible.

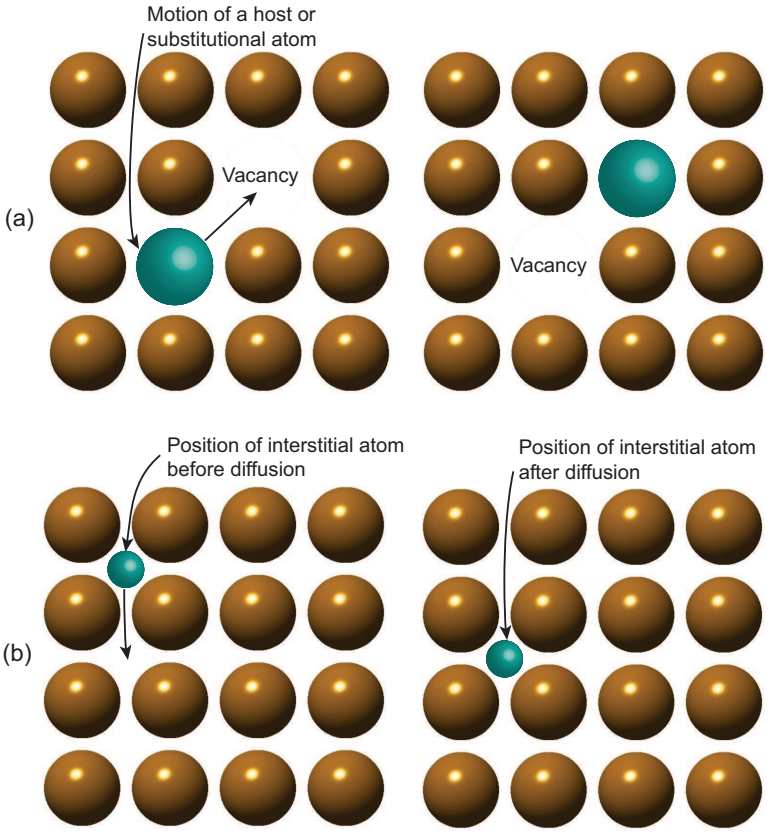

Figure 2.2: Two dimentional representation of (a) the substitutional mechanism and (b) the interstitial mechanism.

There are several parameters that can affect the "solubility" of the solute atoms (dopants) in the solvent (host material) and these are: the ionic size factor, crystal structure, electronegativity and valency [61]. The size of the dopant atoms can be very critical for the stability of the host lattice. Dopants with very small ionic radii compared to the host atoms can have a negative impact on lattice stability and dopants with very large ionic radii can cause lattice distortions. Temperature is a factor that can play an interesting role in a post-doping phase (for example during annealing) as it can give rise to diffusion phenomena. More precisely, atoms vibrate more intensely around their equilibrium positions and consequently bonds can break and new ones can be formed. With increased addition of impurity atoms, crystal systems tend to form solid solutions and/or a new second phase depending on the concentration of dopant and the temperature of the system [61].

Regarding the diffusion, there are two mechanisms as shown in Figure 2.2, the substitutional mechanism (a) and the interstitial mechanism (b) [61]. In the substitutional mechanism, a substitutional atom jumps into a vacancy and leaves another vacancy behind. Likewise, the motion of atoms can be described as motion of vacancies. In the interstitial mechanism, an atom moves by hopping between interstitials. Therefore, dopant atoms can be accommodated either in interstitials or in host atom vacancies and the doping is called interstitial and substitutional respectively. The main two defect types are Frenkel and Schottky. A Frenkel defect is formed when an atom from the crystal lattice migrates from its position and gets into an interstitial position, leaving a vacancy behind. The Schottky defect is formed when a lattice ion leaves its lattice position and a vacancy is created in this site.

In this work where Al and Nb atoms have been used as dopants in amorphous TiO_{2-x} thin films, it is not certain what kind of defects are formed. Although the oxide is amorphous due to low temperature deposition, short order periodicity in the lattice is assumed. The oxidation state of Al is 3+ (4+ for Ti) and its relative charge is 1-, therefore the charge of two Al ions would be compensated with one oxygen vacancy (2- charge). Likewise, the oxidation state of Nb is 5+ and its relative charge 1+, therefore the charge of two Nb ions would be compensated with one oxygen interstitial (2+ charge).

2.3.1 Doping of binary and perovskite oxides

Doping of functional oxides for RRAM applications became extremely popular during the last 5 years and a large number of publications emerged concerning the enhancement of switching behaviour, endurance and retention. Most of these publications involve doping of thin films with Reactive Sputtering and Atomic Layer Deposition (ALD) [54, 55, 62, 63, 64, 65, 66, 67]. However, there are a few reports on doping of thin films with Electrodeposition [68], sol-gel [69] and aqueous solution methods [56].

2.3.1.1 Thin film doping using Reactive Sputtering

Huang *et al.* [70] developed Cu-doped SiO_x (30 nm thick) RRAM devices with reactive sputtering, where the Cu concentration (1.5–5.0 % at.) was controlled by adjusting the co-sputtering power. Using the same method, Tsai *et al.* [64] prepared Sn-doped SiO_x (30 nm thick) RRAM devices and observed that the electrical current conduction in LRS changed from Ohmic conduction to hopping conduction. Lin *et al.* [62] fabricated Cu-doped SiO_x (10 nm thick) RRAM devices with reactive sputtering and reported better stability in resistive switching because of the Cu ions present in the SiO_x film that acted as oxygen ion traps. Chang *et al.* [54] developed RRAM devices with Zr:SiO_x(6 nm)/C:SiO_x(14 nm) bilayer as insulating film, deposited with reactive sputtering. The

Zr and C content in the SiO_x films were 7.9 and 7.49 % at. respectively. The bilayer devices compared to Zr:SiO_x devices exhibited better stability and switching performance. Chang *et al.* [65] fabricated Ti:SiO_x (∼10 nm thick) RRAM devices with reactive sputtering and after treating them with $SCCO_2$, they observed carrier hopping conduction by means of the ion migration. Li *et al.* [63] reported that the stability and resistive switching characteristics of Ti-doped (2 % at.) ZnO based RRAM devices were improved. The reason for this improvement according to authors is that oxygen vacancies are formed around the Ti atoms that assist with the conductive filament formation and rupture. In higher dopant concentrations (5%) the Ti atoms act as scattering centers and obstruct the conductive filament formation which results in higher switching voltages and poorer endurance of the RRAM cell. The 50 nm thick films were deposited by reactive sputtering and the Ti concentrations attempted were 1, 2 and 5 % at. They also observed that by increasing the atomic Ti concentration, HRS and LRS resistances increased, RESET current decreased and endurance was improved.

2.3.1.2 Thin film doping using Atomic Layer Deposition (ALD)

Congedo *et al.* [55] prepared Al-doped HfO_x thin films via ALD for non-volatile charge trapping memories and they discovered that dielectric constant k, increased to 32 ± 1 in the Al-doped samples compared to 16 ± 1 in the undoped HfO_x samples. Additionally, the stacks with Al-doped layers exhibited better program speed (10^6 s) in higher program voltages (20 V) and lower equivalent of thickness (EOT) values. Spiga *et al.* [67] reported the development of ALD grown Al-doped ZrO_x thin films for incorporation in volatile and non-volatile memory devices and high-performance transistors. The devices with the doped thin films displayed higher dielectric constant compared to the undoped ones, higher thermal stability and trapping potential with a band of trap energy levels in the range of 1.4–1.9 eV above the valence band. Lamagna *et al.* [66] reported that in the ALD deposited Al-doped ZrO_x thin films for $In_{0.53}Ga_{0.53}As$ integration, Al atoms are responsible for stabilizing the cubic/tetragonal phases and for the high dielectric constant which is double compared to the one of pure Al_2O_3.

2.3.1.3 Thin film doping using Electrodeposition, Sol-Gel and Aqueous Solution methods

Younis *et al.* [68] reported that the RRAM devices with Ti-doped ZnO (2 % at.) thin films deposited by electrodeposition exhibited improved switching performance with HRS/LRS ratio equal to 14 compared to the undoped ones. Sol-gel was utilized by Xu *et al.* [69] for the deposition of V-doped ZnO thin films to be implemented in RRAM devices. The devices demonstrated both unipolar and bipolar switching behaviour and enhanced endurance and retention characteristics. Yao *et al.* [56] developed Ga-doped ZnO nanorod thin films (220 nm thick) with an aqueous solution method. The thin films

were incorporated in RRAM devices that exhibited stable unipolar resistive switching behaviour. Another report regarding RRAM devices with La-doped ZnO thin films deposited by aqueous solution method was published by Xu *et al.* [71]. The authors argued that doped devices, exhibited superior unipolar switching behaviour compared to the undoped ones and that the top electrode could play a key role on whether the resistive switching would be unipolar or bipolar.

2.3.1.4 Theoretical calculations for doped thin films

There are also few papers with theoretical calculations for the doped thin films where they attempt to predict what will be the effect of doping on the oxygen vacancies, the band energy structure of the doped lattice crystal and the possible energy states that will be introduced from the presence of the dopant atoms. First–principles calculations was performed by Zhang *et al.* [58] and they predicted that trivalent metal (such as Al, La) doping in ZrO_2 thin films would control the formation of oxygen vacancies and the resistive switching behaviour.

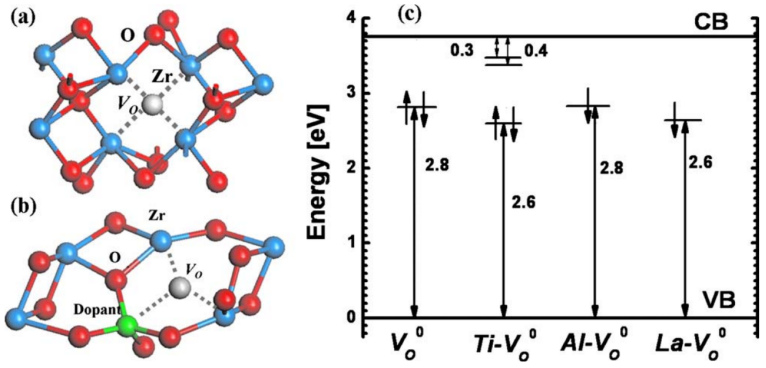

Figure 2.3: Graphical representation of a V_O in (a) undoped ZrO_2 and (b) in doped ZrO_2. (c) Single electron energy levels of neutral V_O in doped and undoped ZrO_2.

They also reported that Al and La doping in ZrO_2 reduced the formation energy of oxygen vacancies (Figure 2.3c) fact that could be attributed to Coulomb interactions of dipoles between dopants and oxygen vacancies. After experimental demonstration, the Al doping in ZrO_2 enhanced significantly the uniformity of the resistive switching, the range of forming voltages became narrower, and the dispersion of R_{HRS} and R_{LRS} has been significantly reduced.

2.3.2 Doping of TiO_2

The resistive switching mechanism in RRAM devices varies depending on the dielectric properties (band gap or trap energy level), the properties of the interface between the metal and the oxide and the fabrication conditions (annealing ambient and temperature). It has been suggested the dominant mechanism can be originating from a thermal effect, an ionic effect or an electronic effect inside the switching layer [31, 72]. According to Waser et al. [29], a typical resistive switching behaviour stemming from a thermal effect is triggered by a dielectric breakdown caused by electroforming. During this process, filaments in the dielectric are formed and modified by Joule heating. The composition of these filaments in the case of transition metal oxides is believed to be insulator material in the form of sub-oxides [73].

The resistive switching mechanism is still under dispute. However, there is a large number of reports with experimental proofs that resistive switching is carried out with the formation of conductive paths [9, 10, 28, 29, 30, 63, 12, 74]. Concerning the TiO_2 RRAM, most researchers believe that oxygen vacancies are responsible for the conducting filament formation, while some others believe that Ti interstitials are responsible for this phenomenon [75, 76]. In this work, it is assumed that oxygen vacancies play the key role in the conducting filament formation. According to this hypothesis, oxygen ions are driven away from their lattice sites due to the strong electric field and migrate towards one of the electrodes, leaving an oxygen vacancy behind them. The oxygen vacancy formation is represented by the following equation [77]:

$$O_o \leftrightarrow \frac{1}{2}O_2(\text{gas}) + V_o^{\cdot\cdot} + 2e^- \tag{2.1}$$

O_o indicates an oxygen ion on a lattice site and $V_o^{\cdot\cdot}$ represents an oxygen vacancy with double positive charge. In case oxygen ions are electrochemically oxidised to form O_2 gas, the remaining oxygen vacancies in the lattice are compensated by electrons (two electrons fully compensate one oxygen vacancy) and the oxide is therefore reduced.

Figure 2.4 is a graphical representation of the filament formation in a TiO_2-based RRAM cell where (i) is the pristine state, (ii) is the oxygen vacancy formation after the application of positive bias on the TE and (iii) the oxygen gas formation. Conducting filaments are formed and annihilated repeatedly with every switching cycle. However, it is unlikely that the system returns 100% to its initial state. In cases of devices with poor endurance and after a large number of switching cycles, oxygen tends to escape through the TE. The HRS and LRS become less distinguishable, the RRAM cell degrades and finally fails permanently [10]. The physical composition of the conductive filaments is believed to be reduced oxide, from the oxygen vacancies created when oxygen ions are drifting away from their lattice sites and compensated by electrons.

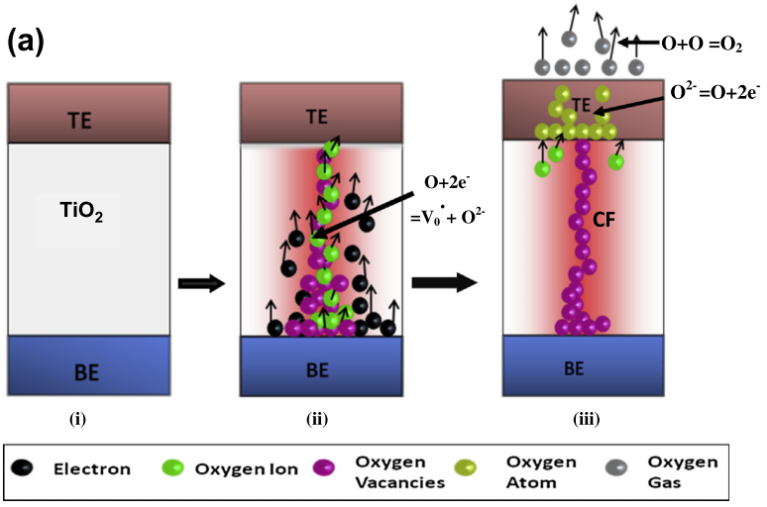

Figure 2.4: (a) Illustration of conducting filament formation during electroforming. Red area indicates Joule heating: (i) Pristine State (ii) after applying positive voltage on top electrode, filament is formed by oxygen vacancies towards Cathode (iii) oxygen atoms are accumulating in the TE and O_2 gas is generated from the TE.

This process occurs in both doped and undoped RRAM devices. However, when dopants are introduced into the crystal lattice, additional defects are formed and contribute to the electroforming and switching processes in various ways. The defects can be either Frenkel or Schottky types, depending on the host oxide, the ionic radii of the dopants and the deposition/doping method [78]. Schottky defects like oxygen vacancies in TiO_{2-x} can be spontaneously created during the thin film deposition. However, additional oxygen vacancy defects can be created when introducing foreign elements in TiO_{2-x}, as it has been suggested by Zhao *et al.* [79].

More precisely, it has been demonstrated by Zhao *et al.* [79] with DFT calculations that dopants could be classified for their doping effect according to their valency. Apparently, they chose Zr and Hf with the same number of valence electrons with Ti, Sr and Al with less valence electrons than Ti and V, Cr, Co, Ni and Cu with more valence electrons than Ti. Figure 2.5 shows which dopants increased or decreased the band gap and whether they introduced new states or not and they correlated this information with the valence electron configuration of each dopant.

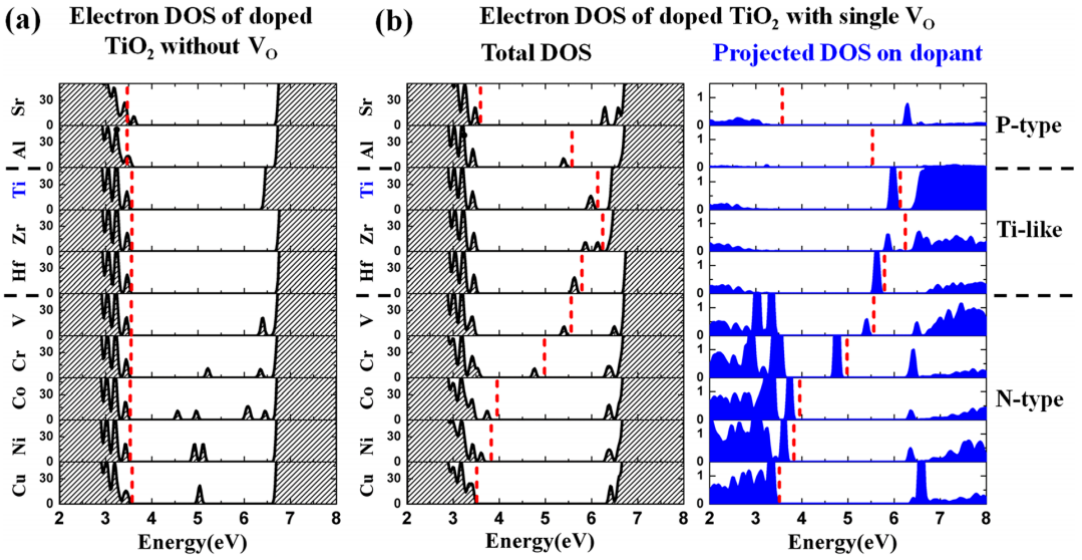

Figure 2.5: Electron DOS calculated for the TiO_2 supercells with the 9 kinds of dopants, (a) without oxygen vacancy and (b) with one oxygen vacancy next to the dopant. (b) shows both the total DOS and projected DOS on the dopant. The undoped case (Ti) is plotted as a reference. The Fermi levels of each system are indicated by red dashed lines.

Zhao and his co–workers also came across to the conclusion that most dopants decrease the formation energy of oxygen vacancies which directly leads to forming voltage and current reduction. Another very interesting outcome was the fact that dopants attracted oxygen vacancies that clustered around them and in that way they created constrains on the conductive paths. The Ti interstitial formation is described from the following equations using Kröger-Vink notations [77]:

$$2O_o + Ti_{Ti} \leftrightarrow Ti_i^{\cdots} + 3e^- + O_2, \tag{2.2}$$

$$2O_o + Ti_{Ti} \leftrightarrow Ti_i^{\cdots\cdot} + 4e^- + O_2, \tag{2.3}$$

where O_o represents an oxygen ion sitting in an O lattice site, Ti_{Ti} is a Ti ion sitting in a Ti lattice site and $Ti_i^{\cdots}$ and $Ti_i^{\cdots\cdot}$ are Ti interstitials with 3+ and 4+ charge. This work is focused on the TiO_2 doping as this is an oxide that has been studied thoroughly during the last 10 years for its resistive switching behaviour. Moreover, there is a decent number of studies with respect to the TiO_2 bulk and surface structure and properties like the ones from Diebold [77] and Grant [80]. TiO_2 owns significant advantages like wide band gap, high thermal stability, high dielectric constant and it can adopt both unipolar and bipolar switching behaviours [8]. As an oxide, it is easily deposited and it demonstrates a variety of oxygen deficient crystal phases and some of them are known as

"Magneli phases" and are expressed as Ti_nO_{2n-1} [81]. The formation of Magneli phases is described by the following equation [12]:

$$nTiO_2 \; + \; 2e^- \; \leftrightarrow \; Ti_nO_{2n-1} \; + \; O^{2-} \tag{2.4}$$

The non-stoichiometry results from the insufficient supply of oxygen during the deposition and that makes it an ideal oxide to study the resistive switching phenomena with [10]. Figure 2.6a,b displays the phase diagrams for the O-Ti system. Phase diagrams like the ones depicted in Figure 2.6 are very useful when studying an oxide because they can assist in predicting the resulting phase after deposition or after annealing.

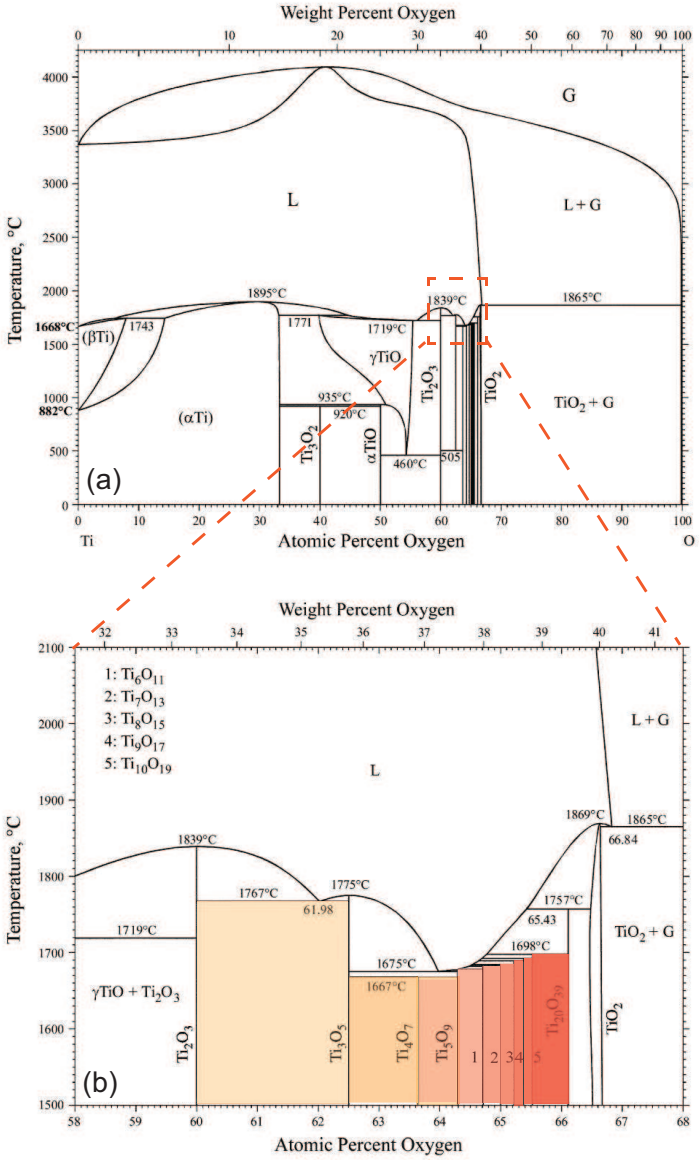

Figure 2.6: (a) O–Ti phase diagram and (b) its zoomed version in the area of 58-68 at.% of oxygen. The shaded areas highlight the Magneli phases.

Valency is a strong criterion when choosing the candidate dopant for an oxide. More precisely, the ionic radius of the dopant is of great significance. If dopants with greater ionic radius are used to dope crystal lattices where the host atoms have smaller ionic radius, distortion of the lattice is very possible to occur. This lattice distortion is undesirable in this case as it might have impact on the surface roughness of the thin film. The dopants atoms in TiO_{2-x} were selected with ionic criteria but the electronic effect was also taken into consideration. More precisely, Al is expected to introduce oxygen vacancies as it has a 3+ oxidation state, compared to 4+ of the Ti if it replaces Ti in the host sites, enabling this way p-type conductivity. On the other side, Nb is expected to enable n-type conductivity in TiO_{2-x} due to its 5+ oxidation state. The Al and Nb atoms are likely to replace Ti atoms at host sites, if during the sputtering deposition the substitution of Ti atoms is thermodynamically preferred. In an opposite case, it is unlikely that the dopant atoms will be forced in Ti interstitials however this possibility cannot be excluded. The oxidising atmosphere during the deposition is likely to cause oxidation of the dopant atoms and therefore result in the deposition of a mixed oxide phase of Al/Ti and Nb/Ti. Equations 2.5 and 2.6 describe the substitution of Ti by Al and Nb using Kröger-Vink notations.

$$nTiO_2 \xrightarrow{Al_2O_3} 2Al'_{Ti} + V_o^{\cdot\cdot} + 3O_o^x \tag{2.5}$$

$$nTiO_2 \xrightarrow{Nb_2O_5} 2Nb^{\cdot}_{Ti} + O_i'' + 5O_o^x \tag{2.6}$$

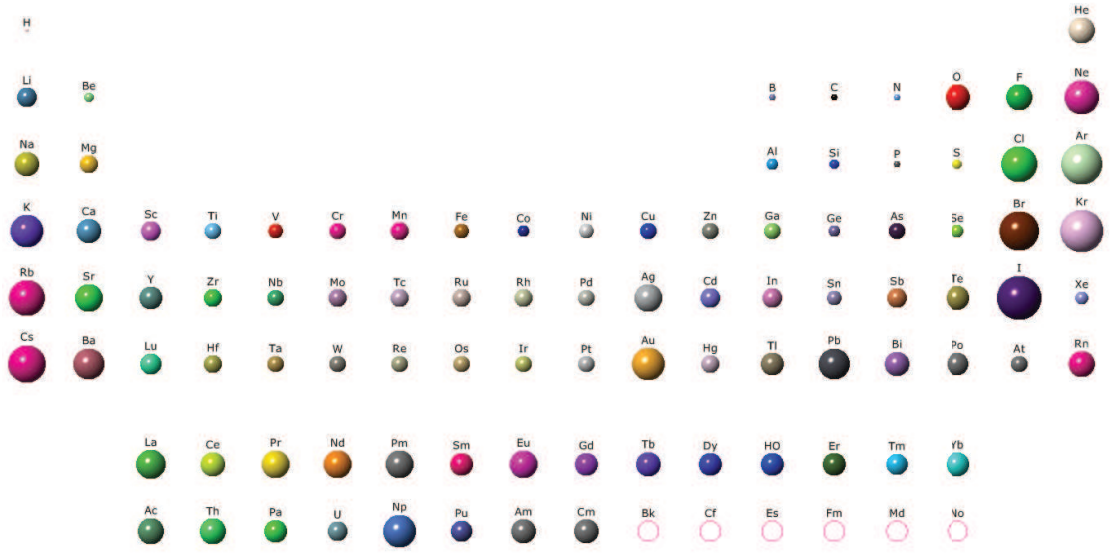

Figure 2.7: The ionic radii sizes for all the elements of the periodic table. The data used for this table were taken from Shannon.

Figure 2.7 displays all the elements of the periodic table with a sphere that represents their ion size. One can easily observe that the Ti and Al ions have comparable ionic

radii. The actual values of the ionic radii of Ti, O and Al are displayed in Table 2.2 for all the possible coordinations.

Table 2.2: The ionic radii of the Ti, Al and O ions from Shannon. The numbers in brackets indicate the coordination.

	Ionic radii (*Å*)
Ti^{+2}	0.86
Ti^{+3}	0.57
Ti^{+4}	0.42(IV), 0.52(V), 0.605(VI), 0.74(VIII)
Al^{+3}	0.39(IV), 0.48(V), 0.535(VI)
O^{-2}	1.35(II), 1.36(III), 1.38(IV), 1.4(VI), 1.42(VIII)

In literature, doping of TiO_{2-x} thin films has been performed with a variety of techniques including DC and RF Reactive Sputtering [82, 52, 83], Atomic Layer Deposition (ALD), Pulsed Laser Deposition (PLD) [84] and sol-gel [51]. Bulk TiO_{2-x} has been doped with Metal Oxide Chemical Vapor Deposition (MOCVD) and solid-state mixing methods [50, 85]. However, the majority of these papers concern electrochromic and photocatalytic applications. Huang *et al.* [86] prepared Cu-doped TiO_2 thin films with DC reactive sputtering that next incorporated in RRAM devices. The devices containing the doped thin films exhibited better endurance of 1000 cycles and lower SET voltage of –0.7 V compared to 400 cycles and –1.5 V of the undoped devices. This was a strong proof that the presence of the Cu atoms inside the TiO_2 lattice enhanced the resistive switching performance of the device. Zhong-Wen *et al.* [84] fabricated 15% at. Cr-doped TiO_x thin films with Pulsed Laser Deposition (PLD). The RRAM devices incorporating these layers exhibited bipolar resistive switching and very high electric–pulse induced resistance ratio along with low threshold voltages. Liu *et al.* [87] developed Gd-doped TiO_2-based RRAM devices with sol-gel that exhibited unipolar resistive switching behaviour. The literature review on doped RRAM devices is summarized in Table 2.3 and their most interesting resistive switching characteristics are highlighted for comparison.

Since TiO_{2-x} is an oxide with a non-trivial chemistry, it is believe that its full potential hasn't been realized yet. There have been only a few reports [84, 86, 87] concerning doped TiO_{2-x}-based RRAM devices, where the authors claimed an improved endurance and resistance ratio. Thus, doping engineering of the TiO_{2-x} RRAM has not been fully exploited yet (especially with reactive sputtering).

2.4 C-AFM for studying resistive switching in thin films

The fact that resistive switching phenomena occur at the nanoscale, creates the need to observe and study these dynamics in oxide thin films, in very constrained areas.

Table 2.3: Comparison of existing doped RRAM devices in terms of their resistive switching characteristics.

Oxide	*Method*	*Remarks*	*Reference*
Al-AlO_x	RF magnetron sputtering	The multi-layered devices exhibited better endurance than the single layered ones	Song *et al.* [88]
Cu-AlO_x	Plasma oxidation	10^2 cycling endurance 10^4 s retention at 85°C $V_{SET}/V_{RESET} = +1.9\ V/+0.6\ V$ 10^5 Ω resistance window	Wu *et al.* [46]
Cu-TiO_x	DC magnetron sputtering	10^3 cycling endurance $V_{SET} = +0.7\ V$ compared to +1.5 V for the undoped devices	Huang *et al.* [86]
Cr-TiO_x	PLD	$V_{SET}/V_{RESET} = -2\ V/+2\ V$	Zhong-Wen *et al.* [84]
Gd-TiO_x	sol-gel	typical unipolar RS behavior	Liu *et al.* [87]
Al-ZnO_x	RF magnetron sputtering	300 cycling endurance $V_{SET}/V_{RESET} = +0.5\ V/-0.5\ V$ 80% transparency	Xu *et al.* [89]
La-ZnO_x	chemical solution dep.	10^4 s retention at 85°C $V_{SET}/V_{RESET} = +1.5\ V/-1.5\ V$	Xu *et al.* [71]
Ti-ZnO	electrodeposition	>2000 s retention at 25°C $V_{SET}/V_{RESET} = +2.9\ V/-3.0\ V$	Younis *et al.* [68]
V-ZnO	sol-gel	10^4 s retention at 85°C $V_{SET}/V_{RESET} = -1.5\ V/-2.0\ V$ $R_{HRS}/R_{LRS} \sim 10^3$	Xu *et al.* [69]

Conductive atomic force microscopy (C–AFM) is an ideal technique for this purpose as it offers simultaneous in situ recording of spatial topography and current distributions with a nanometer scale lateral resolution roughly equal to the end radius of the tip [90, 91, 92, 93]. Scanning Tunnelling Microscopy (STM) has also been used for nanoscale electrical characterization of thin films as it has advantage over other methods due to the atomic scale resolution [94, 95]. In STM the tip is in close proximity from the surface, thus adding a resistive component in the tip-sample system [90]. In C-AFM the tip is in physical contact with the oxide layer, resulting in a setup which is closer to the MIM configuration. However, even C–AFM measurements can be affected by additional resistive components such as adsorbates or impurities on both tip and sample surfaces. The main advantage of C–AFM over STM is the fact that C–AFM measurements can be performed under different atmospheres and in ambient conditions.

So far, C–AFM characterization of TiO_{2-x} thin films designed for RRAM applications has been mainly used for the evaluation of conductive filaments [96, 97], the identification of switched areas [98] and for the investigation of the RS mechanism at the very early stage of electroforming [99]. Two main methodologies have been reported for studying TiO_2 thin films using C–AFM. The first consists of switching the RRAM cell, delaminating the

top electrode using techniques such as focused ion beam (FIB) [100], wet etching [96, 101], mechanical cleaving [97, 98, 102], AFM etching [93], and finally, scanning the bare oxide film using a C–AFM tip. However, by using this approach the oxide film can be affected during the electrode removal process. The second method consists of switching in situ the bare film by using the C–AFM tip as a nanosized top electrode [92, 103, 104, 105]. Most C–AFM studies on TiO_2 refer to thicknesses in the range of 25-60 nm [97, 99, 101]. However, downscaling the physical thickness of the film is crucial for achieving low voltage switching, which is extremely important for low-power applications [96]. In the present work, we have investigated the switching dynamics of a 10 nm thick titanium dioxide thin film deposited by reactive sputtering on $Si/SiO_2/Ti/Pt$ supports following the second approach, that is, by switching the films in situ using a C–AFM tip as a top electrode.

Chapter 3

Engineering the switching dynamics of TiO_x RRAM with Al doping

3.1 Introduction

A wide range of oxides has been successfully employed in RRAM cells so far, with some of them (like TaO_x and HfO_x) demonstrating exceptional results in cycling endurance [33], retention [35] and switching speed [42]. However, very often RRAM devices suffer from low yields, degradation [14, 15] and large variability of the switching parameters of identical cells [16]. Previously, it has been shown that device electroforming and/or resistive switching at high voltages can create irreversible protrusions on the top electrode [12, 22, 106] that accumulate and eventually cause permanent device failure, also known as "hard-breakdown"; an irreversible process. The useful operating regime for RRAM devices exploits a reversible "soft-breakdown" mechanism and it is naturally bound above the switching threshold of the device (V_T) and below HB (V_{HB}) [17].

The need for preventing RRAM failure has created a lot of interest towards engineering the active layers by incorporating foreign elements. TiO_x is an oxide that has been studied a lot for its electrochromic behaviour, it has been doped with several elements and there has been a lot of effort for understanding its chemistry. Besides other applications, it has been extensively studied as a model oxide exhibiting RS due to its intrinsic variety of possible crystal phases [77] and associated richness of switching dynamics. Although different RS mechanisms have been suggested [31, 29], a universal model that explains most of these proposed mechanisms is still missing. Several studies suggest that TiO_{2-x} reduced phases play a critical role in the switching mechanism of TiO_x-based RRAM. Recent characterisation studies based on electron microscopy combined

with *in-situ* switching suggested that highly conductive nanofilaments (CFs) comprising reduced phases (Ti_nO_{2n-1}) [81], also called *Magnéli* phases could be responsible for the RS in TiO_{2-x} [12, 107, 19]. Conductive Atomic Force Microscopy (C-AFM), is among others, a commonly employed technique for studying the RS phenomena at the nanoscale, like CF formation [22, 108, 109, 110, 101], due to its high lateral resolution and capacity to simultaneously record electrical and topographical changes emerging during electrical stimulation.

The stochastic nature of CF formation process during EF and RS due to spontaneous local redox processes [31] is often associated to the variability of switching in RRAM cells. It has been suggested that the RS dynamics of TiO_x-based RRAM devices can be engineered by incorporating dopants of a suitably chosen oxidation state. Zhao *et al.* published a relevant theoretical study regarding the effect of dopants with different oxidation states on the electronic structure of rutile TiO_2, concluding that most of them could reduce the energy required for EF and also reduce the CF formation variability [79]. Huang *et al.* suggested that Cu doping in TiO_{2-x} RRAM improved the cycling endurance and lowered the SET voltage [86]. It has also been reported that doping TiO_{2-x} with trivalent elements like La, Ga, Co, Cr and Al is ensuring a more consistent CF formation thus enhancing device reliability [10]. Aditionally, Zhang *et al.* published a relevant study on ionic doping of ZrO_2 RRAM and concluded that trivalent ion (Al or La) doping could significantly reduce the oxygen vacancy formation energy and therefore reduce the EF voltages and improve the variability of RS [58].

In this chapter, Al was used as a dopant in TiO_x-based RRAM cells to engineer the RS dynamics of the devices. For this study, TiO_x and Al:TiO_x thin films were deposited by reactive sputtering and characterised by XPS for the doping concentration as well as for their chemical state by X-ray Photoelectron Spectroscopy (XPS). The SB threshold voltages of the undoped and Al-doped TiO_x thin films were first evaluated by C-AFM measurements. The effect of Al doping on EF and RS is investigated by voltage pulse sweeping RRAM devices comprising the same active layer configurations. Device characterisation is performed by a custom-made testing system and algorithm (biasing parameter optimiser by Serb *et al.* [111]) in an automated manner.

3.2 Reactive sputtering of Al-doped and undoped TiO_x thin films

10 nm thick TiO_x and Al:TiO_x films were deposited via reactive sputtering on a 6″ Si substrate comprising SiO_2(200 nm)/Ti(5nm)/Pt(200 nm) layers, from a Ti metal target. The sputtering (Helios XL, Leybold Optics) settings for both layers were: 8 sccm O_2 and 35 sccm Ar at the Ti cathode operating at 2 kW and 15 sccm O_2 at the plasma beam source operating at 2 kW. For the deposition of the Al:TiO_x layer, an Al target

was fitted on the second magnetron which was operated at 50 W without any additional O_2 flow supplied at that cathode. At all times the plasma levels were lambda controlled at a setpoint of 365 mV. The thickness and the refractive index of the thin films were evaluated by Spectroscopic Ellipsometry (Woolham M-2000) using the Cody-Lorentz model.

3.3 Device fabrication and testing overview

TiO_x and Al:TiO_x RRAM devices were independently fabricated on 6″ Si wafers with a 200 nm SiO_2 layer grown by dry oxidation and a 5 nm Cr bottom electrode-adhesive layer deposited via electron-beam evaporation. The electrodes and active layers were patterned by optical lithography. The bottom electrodes (5 nm Pt) and the top electrodes (4 nm Pt) were deposited by electron-beam evaporation followed by lift-off. The active layers were deposited as described in section 3.2. The finished devices had a standalone configuration with $50 \times 50\ \mu m^2$ device area. The devices were electroformed using the algorithm presented in [112] and switched using a custom-made testing routine [111]. The as mentioned algorithms were implemented via a custom-made PCB-based system for device testing and characterisation [113].

3.4 Al:doped and undoped TiO_x thin film chemical composition evaluation with XPS

XPS was used to evaluate the composition of TiO_x and Al:TiO_x thin films. The XPS spectra were recorded using a Thermo Scientific Theta Probe Angle-Resolved X-Ray Photoelectron Spectrometer (ARXPS) system with a monochromated Al Kα X-ray source (hv = 1486.6 eV) operating at a base pressure of 2×10^{-9} mbar. Data were collected over an area of approximately $400 \times 400\ \mu m^2$ and with a pass energy of 200 and 50 eV for survey and core level spectra, respectively. The X-ray source was operated at 6.7 mA emission current and 15 kV anode bias and photoelectrons were collected over a cone of ±30° with the lens mounted at 40° in respect to the sample surface. A 180° double focusing hemispherical analyzer with two-dimensional ARXPS detector are part of this system. C 1s core level at 285 eV was used as reference for charge shift correction. All data were analyzed using the Avantage software package.

Figure 3.1(a) displays the survey spectra of the TiO_x and Al:TiO_x thin films. In both thin films, Ti 2s, O 1s, Ti 2p, Ti 3s, Ti 3p and O 2s peaks were present. The C 1s peak at 285.0 eV present in both thin films due to exposure to air, has been used for charge shift correction. Al 2s and Al 2p core levels at binding energies 118.5 eV and 74.0 eV, respectively, were detected only in the Al:TiO_x thin film, as shown in

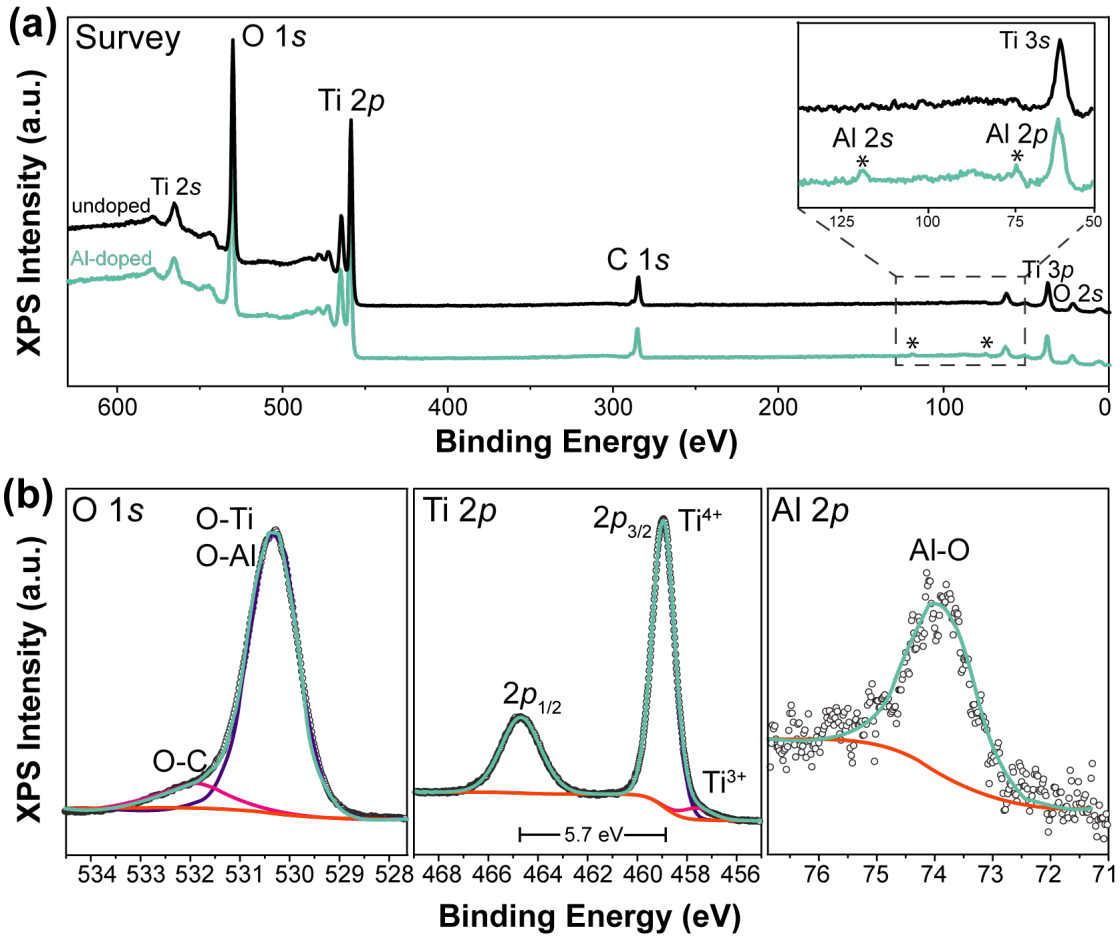

Figure 3.1: (a) XPS survey spectra of the TiO_x and Al:TiO_x thin films; Inset shows the position of Al 2s and Al 2p photoemission peaks. (b) fitted O 1s, Ti 2p and Al 2p core level spectra recorded from the Al:TiO_x thin film.

the inset of Figure 3.1(a). Figure 3.1(b) exhibits in detail the main resulting core levels from the photoemission of the Al:TiO_x thin film. The O 1s core level, comprised two peaks, one at 530.3 eV associated with lattice oxygen (O-Ti and O-Al bonds) and one at 531.9 eV assigned to non-lattice oxygen (O-C bonds). The Ti 2p core level with its spin-orbit components 1/2 and 3/2 was detected at 464.7 eV and 459.0 eV respectively. The $2p_{1/2}$ component comprised two peaks, one at 459.0 eV ascribed to Ti^{4+} cations and a smaller one at 457.5 eV ascribed to small population of Ti^{3+} cations. The presence of Al 2p core level at $\sim$ 74.0% eV binding energy is ascribed to Al^{3+} cations with oxygen coordination and it is characteristic of samples with AlO_x composition [114]. After appropriate background subtraction, fitting and normalisation of the recorded spectra, the Al concentration in the Al:TiO_x thin film was found to be $\sim$ 4% at., taking into account only the cations Ti and Al in the quantification. All of the detected energies coincide with average reference energies from the NIST X-ray Photoelectron Spectroscopy Database [115].

3.5 Identification of switching thresholds in thin film level via C-AFM

C-AFM measurements were performed on TiO_x and Al:TiO_x thin films using a Bruker MultiMode Nanoscope V system equipped with a current sensing C-AFM module at room temperature and atmospheric pressure. Conductive Pt/Ir coated Si tips with a cantilever spring constant of 0.2 N/m and nominal radius of 12 nm were used (Bruker, SCM-PIC) with the current sensitivity being set at 1 nA/V. Before performing the C-AFM measurements on the films, the conductivity of the tip was confirmed by scanning a conductive reference sample. In order to minimize the tip wear, a minimum set point of 0.1 V was applied. The DC voltage bias was applied between the bottom electrode and the tip with the latter connected to virtual ground. Therefore, all voltages mentioned in the text should be interpreted as voltage applied on the bottom electrode.

The SB threshold voltage of TiO_x and Al:TiO_x has been identified by performing sets of read-write-read scans over the thin film with the C-AFM tip being in contact acting as a top electrode. The spatial topography and current distribution has been recorded for every scan. The protocol for the SB threshold voltage has been previously reported [22] and it included sets of read-write-read C-AFM scans over pristine areas of the oxide layer with an appropriate voltage. The read scan was performed over a 5×5 μm^2 area to assess the pristine state of the oxide, without affecting it, followed by a write scan with higher voltage over a 2×2 μm^2 area to electrically stress the oxide and a final read scan similar to the initial one. When changes in lateral current distribution (but not in topography) were observed at the final read scan, the voltage of the write scan was considered as SB threshold voltage. It should be noted, that the voltage used for the read scans, was selected as the most appropriate because it was high enough to read current above the noise level but low enough to make sure it would not affect the resistance of the thin film.

Figure 3.2(a)-(b)-(c) displays a set of read-write-read scans (lateral current distributions) recorded from a pristine area of the 10 nm undoped TiO_x thin film. The initial (a) and final (c) read scans were performed on 5×5 μm^2 areas with 5.0 V and the intermediate write scan (b) was performed on 2×2 μm^2 areas with 6.5 V. After the final read scan, the topography of the inner 2×2 μm^2 square was unaffected whereas the lateral current distribution appeared lower. Therefore, 6.5 V was identified as the SB threshold voltage being the lowest voltage at which the current change was observed. We repeated this protocol for the Al:TiO_x thin film and the resulting set of read-write-read scans is shown in Figure 3.2(d)-(e)-(f), where change in current was consistently observed after a write scan with 6.0 V. Hence, 6.0 V was identified as the SB threshold voltage for the Al:TiO_x thin film, which is lower than the one for the TiO_x thin film by 0.5 V. Since these C-AFM scans were carried out on pristine areas of the thin films, these operations can be more appropriately correlated with EF in thin film level. These results are very encouraging

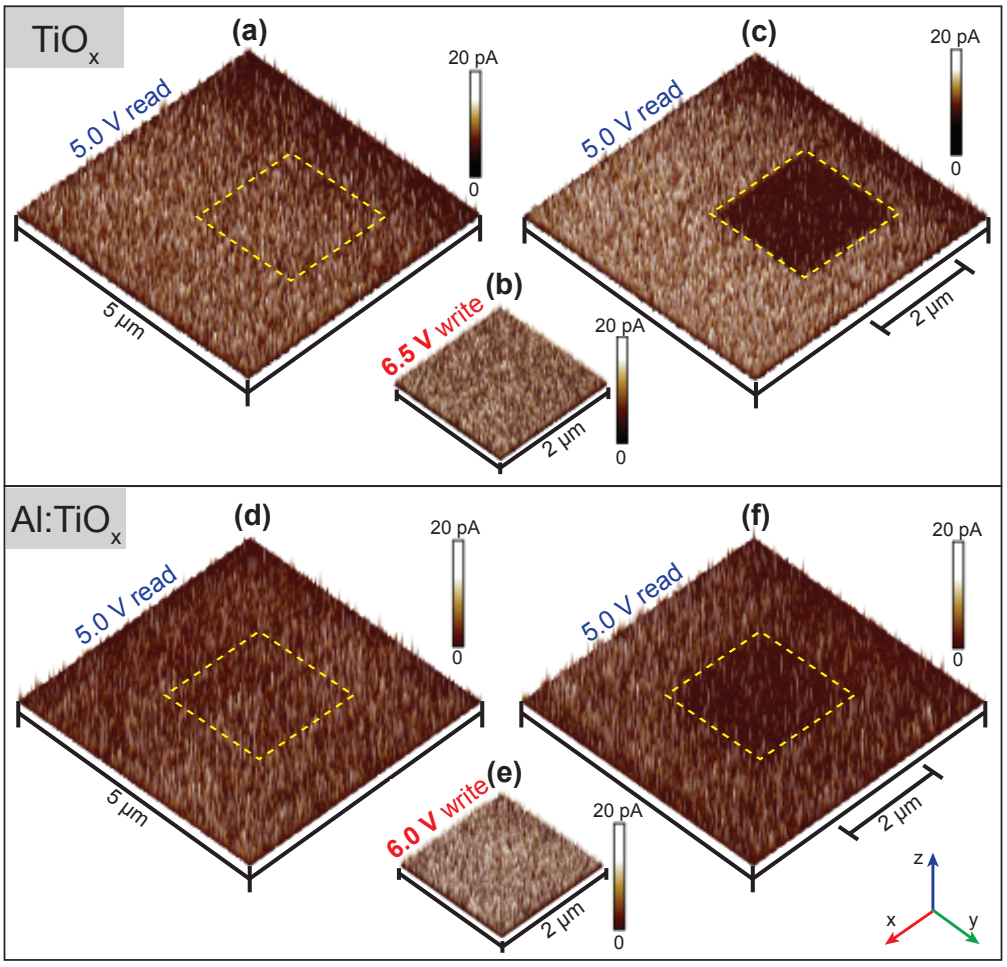

Figure 3.2: Set of read-write-read C-AFM scans recorded from (a-c) the TiO_x and (d-f) Al:TiO_x thin films, displaying the SB threshold voltages 6.5 V and 6.0 V, respectively. The dashed squares indicate the position of the write scan. The scans of each set, were carried out in chronological order.

as they show that Al doping has the potential to decrease the EF voltages and/or the RS threshold voltages. C-AFM was then used to induce switching in the TiO_x and Al:TiO_x thin films.

The conventional switching of devices was replicated in thin films by using the C-AFM tip as top electrode and by applying bias between the tip and the Pt bottom electrode (Figure 3.3(a)). Typical current-voltage (I-V) characteristics obtained from arbitrary points of the TiO_x and Al:TiO_x thin films are shown in Figure 3.3(b). Both I-V characteristics comprise two SET operations, meaning that the applied potential increases temporarily the conductivity. After the removal of the bias, the oxide rests again in HRS, indicating that the states are volatile. We observed this behaviour with every sample measured with this C-AFM setup and it could be attributed to the fact that C-AFM scans are carried out in ambient conditions. The asymmetry of the I-V loops, could be attributed to the size asymmetry between the Pt bottom electrode and the C-AFM tip. The switching setup of standalone devices using a conventional probe station,

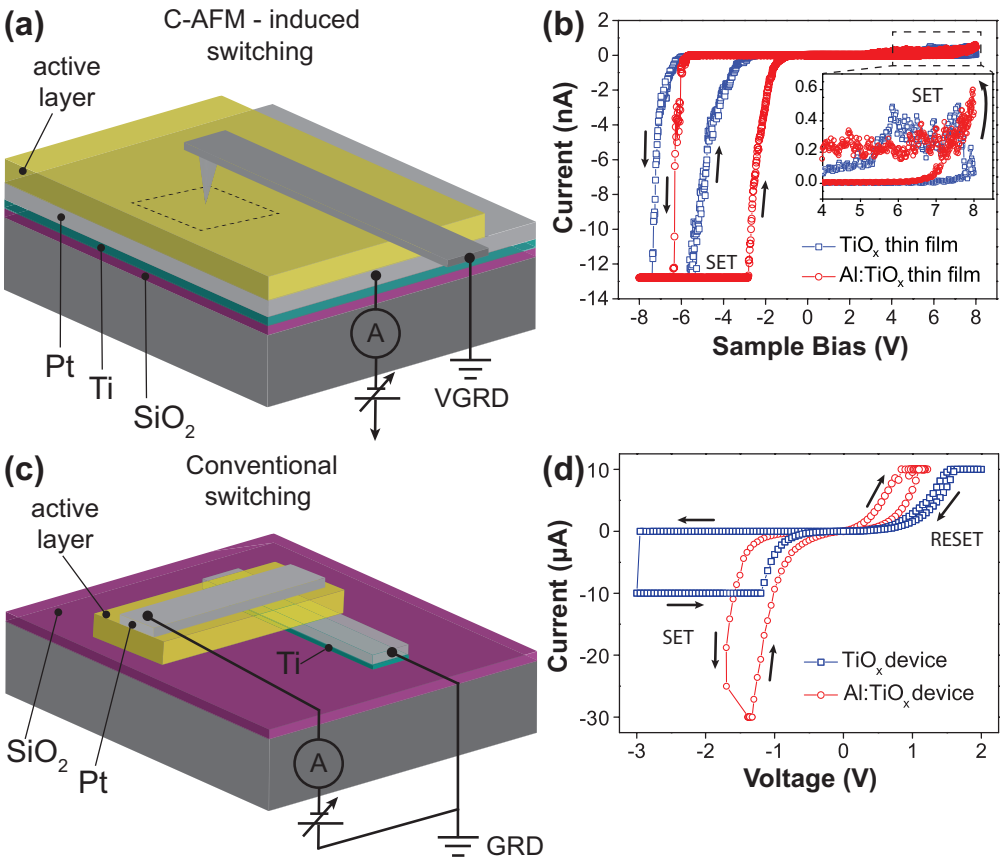

Figure 3.3: (a) The experimental setup of C-AFM induced switching of an oxide thin film, paired with (b) typical C-AFM I-V characteristics from a TiO_x and an Al:TiO_x thin films. In I-V characteristics acquired with a C-AFM probe, both positive and negative voltage sweeps result in a SET. (c) shows the conventional switching of a RRAM standalone device, paired with (d) typical I-V characteristics where SET and RESET are achieved. In both cases, the I-Vs show the positive impact of Al doping in TiO_x RRAM devices.

paired with typical I-V characteristics obtained during voltage sweeping, are shown in Figure 3.3(c),(d). In both cases, there is an indication of a positive effect of Al addition to the Al:TiO_x thin film and Al:TiO_x device, as they exhibit lower voltages compared to their undoped equivalents. On the basis of this promising result, we have performed an accurate device testing, using pulsed stimulation. This was done because the finely time-controlled pulses allow a highly improved degree of control over the device's under test (DUT) resistive state.

3.6 Unoped and Al:doped TiO_x RRAM device electro-forming using a pulsed voltage ramp scheme

The TiO_x and Al:TiO_x thin films were transferred into RRAM devices that were tested using the same EF scheme [112]. The scheme was a ramp of write pulse trains (comprising 10 pulses each) with negative polarity, in which the write pulse voltage (V_w) was ranging from 1-8 V, the write pulse duration (T_w) from 100-1000 μs and the write pulse amplitude step was 0.2 V. The resistance change between each write pulse train was assessed by intermediate read pulse trains (comprising 5 pulses each) with amplitude 0.1 V. The algorithm applied additional write pulse trains until the resistance of the DUT dropped below a given threshold (resistance tolerance band, $\varepsilon = 10\%$ of the last measured resistance). A total of 20 TiO_x and 20 Al:TiO_x-based standalone crossbar devices were tested, however, EF was successful in only 17 devices from each set.

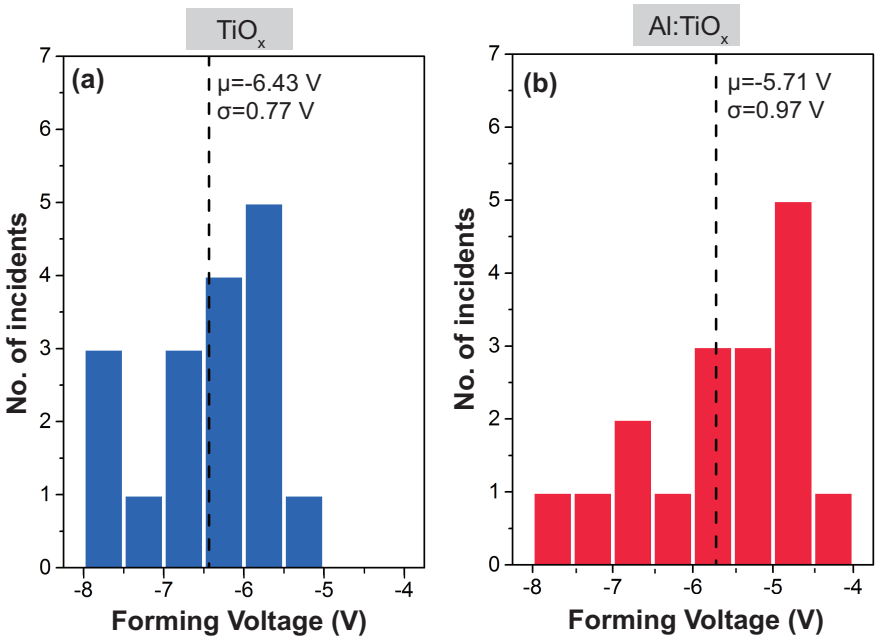

Figure 3.4: Histograms of EF voltages of 17 (a) TiO_x-based and (b) Al:TiO_x-based devices. μ and σ denote the mean (dashed line) and standard deviation values.

Figure 3.4(a),(b) displays the histograms of EF voltages for each set of 17 devices. The dashed line represents the mean forming voltage which was 6.43 V for the TiO_x and 5.71 V for the Al:TiO_x devices, with a standard deviation of 0.77 V and 0.97 V respectively. The average forming voltage of the doped devices is overall lower compared to the one of the undoped devices, in agreement with the trend observed previously via C-AFM measurements.

3.7 Undoped and Al:doped TiO_x RRAM device resistance switching evaluation using pulsed voltage sweeping

Following an EF step, the devices were tested using a biasing parameter optimiser presented in [111]. Table 3.1 summarises all the EF and switching parameters involved in the device testing. The biasing protocol required an initial write pulse amplitude V_{init}, a write pulse amplitude step V_{step}, a maximum allowed write pulse amplitude V_{max}, a write pulse duration T and a number of switching cycles in RS stage. The algorithm applied ramps of write pulse trains (comprising 10 write pulses each) of increasing amplitude, with intermediate read pulse trains (comprising 5 read pulses each) of 0.1 V that assess the resistance change of the device between each write pulse train. Each ramp is accounted as a cycle and therefore Figures 3.5 and 3.6 are depicting a total of 6 cycles in each panel. Once a resistance tolerance band ε, here set at 10% of the last measured value, was exited, the algorithm would apply a ramp of reverse polarity. The value of ε practically determines the minimum operating OFF/ON ratio ($R_{OFF/ON}$) of the DUT, which therefore becomes a controllable operation parameter. However, for this study, ε has been fixed at 10%. A 30 kΩ series resistance was used in all cases to protect the devices from high currents.

Table 3.1: EF and switching parameters involved in the device testing.

	Parameter	Description (unit)	Value	
Electroforming	V_w	Write pulse amplitude (V)	1-8	
	$V_{w,step}$	Write pulse amplitude step (V)	0.2	
	T_w	Write pulse duration (μs)	100-1000	
	SR	Series resistance (k)	100	
Switching	V_r	Read pulse amplitude (V)	0.1	
	M	No. of read pulses per resistance assessment	5	
	N	No. of write pulses per train	10	
	ε	Resistance tolerance band (%)	10	
	V_{init}	Initial write pulse amplitude (V)	1	
	V_{step}	Write pulse amplitude step (V)	0.1-0.5	
	V_{max}	Max. write pulse amplitude (V)	4	
	T	Write pulse duration (ms)	0.1	

Figure 3.5(a),(b) exhibits a typical analog switching behaviour of TiO_x and Al:TiO_x-based devices. Both devices were able to cycle in this fashion repeatedly for a large number of cycles. With a V_w step of 0.1 V, the switching voltages of the TiO_x-based device were +1.8 V/-1.4 V compared to the improved switching voltages of +1.2 V/-1.0 V for the Al:TiO_x-based device. Figure 3.6(a),(b) portrays a typical binary switching behaviour from TiO_x-based and Al:TiO_x-based devices. Likewise, both devices were able to cycle repeatably for for a large number of cycles. V_{step} was 0.5 V and 0.3 V for the TiO_x- and Al:TiO_x-based devices, respectively. The switching voltages of the TiO_x-based device were +1.8 V/-1.4 V compared to the improved switching voltages of +1.2 V/-1.0 V of the Al:TiO_x-based device. In both cases of analog and binary switching, the positive pulse ramps induced a resistance increase and the negative pulse ramps induced

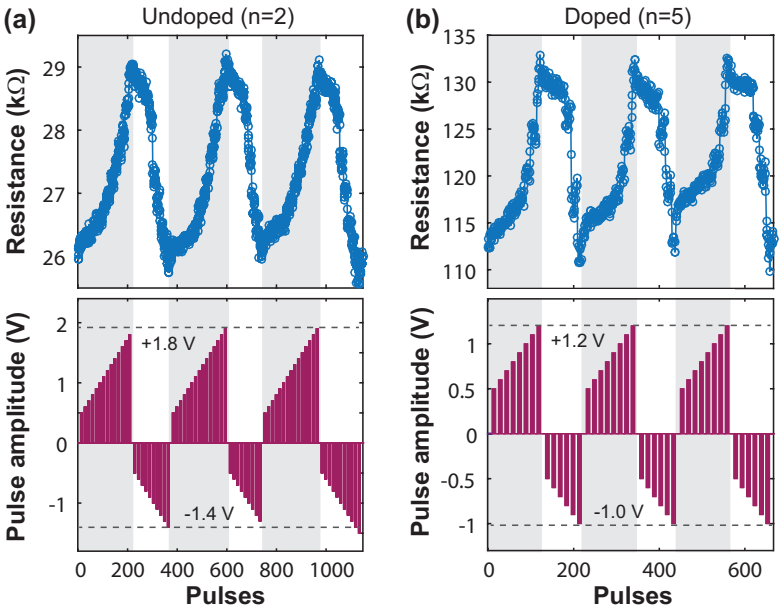

Figure 3.5: Typical analog mode of resistance switching of (a) TiO_x- and (b) Al:TiO_x-based devices.

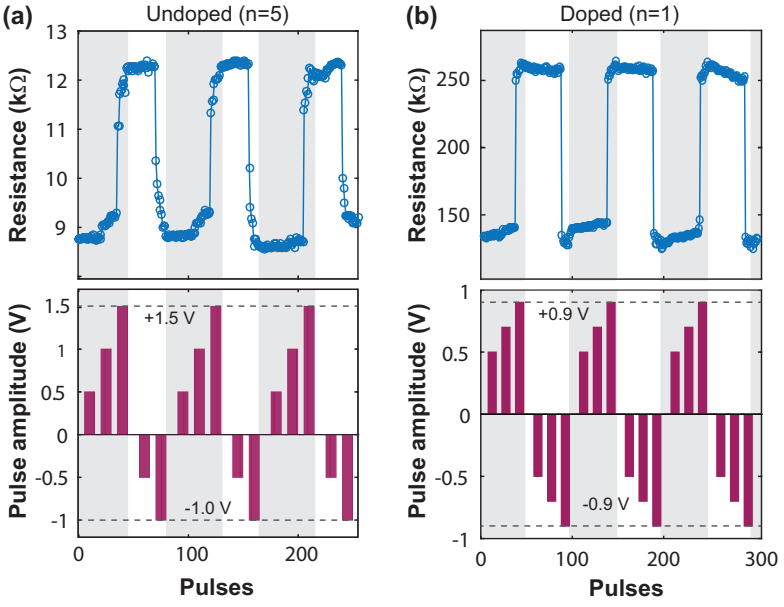

Figure 3.6: Typical binary mode of resistance switching of (a) TiO_x and (b) Al:TiO_x-based devices.

a resistance decrease. Interestingly, the majority of the TiO_x-based devices were able to form and cycle in a resistance range of 5-30 kΩ, while their Al-doped counterparts were forming and cycling in a resistance range of 100-300 kΩ. The fact that the Al:TiO_x-based devices operate within a higher resistance range could have a positive impact in crossbar arrays, where the line resistance becomes less significant.

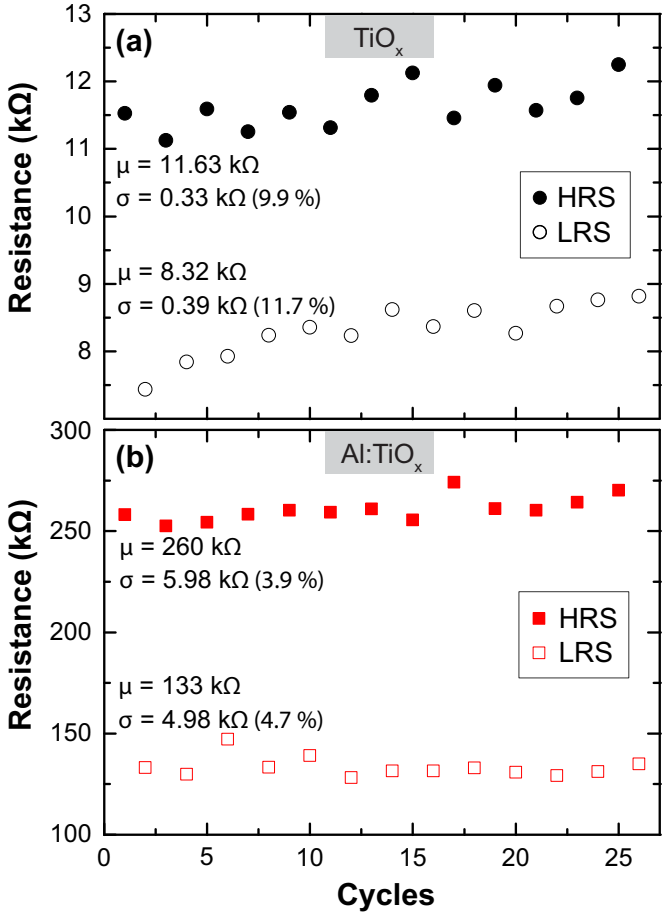

Figure 3.7: Uniformity of HRS and LRS states from typical (a) TiO_x and (b) Al:TiO_x-based devices.

Figure 3.7(a),(b) portrays the first 25 cycles of typical undoped and Al-doped TiO_x devices, respectively. The plotted resistance values, are the ones measured exactly after the resistance tolerance band was exited. The resistance mean (μ) and standard deviation (σ) were calculated for each device and for each resistance state. The relative standard deviation, c, has been calculated by the formula $100\% \times \sigma/\Delta\mu$ to compare the variability of the devices, without taking into account the resistance operation range of each device. Although both devices maintain a well-defined resistance window, c is 3.9 % and 4.7 % for the Al:TiO_x device compared to 9.9 % and 11.7 % for the TiO_x device.

Table 3.2: Comparison table for the TiO_x- and Al:TiO_x-based devices.

Comparison feature	**TiO_x**	**Al:TiO_x**
EF voltage mean (V)	-6.43	-5.71
EF voltage st. deviation (V)	0.77	0.97
Switching voltage (analog) (V)	+1.8/-1.0	+1.2/-1.0
Switching voltage (binary) (V)	+1.5/-1.0	+0.9/-0.9
Operational resistance range (kΩ)	5-30	100-300
Relative standard deviation (%)	9.9%-11.7%	3.9%-4.7%

Table 3.2 summarises all the results arisen from the comparison of the TiO_x- and Al:TiO_x-based devices. We note here that the history dependence of RRAM cells between consecutive write pulse trains or between consecutive single pulses, allow us to extract information on switching voltage due to the collective effect of the total number of write pulses that were sent to the device.

3.8 Discussion

The device behaviour can be explained by considering the formation of a conductive filament within the TiO_x layer, a well-known phenomenon in TiO_x RRAM devices [12, 116]. The initial electroforming step required to switch the devices, for both doped and undoped films, corroborates the filamentary picture. The undoped device I-V characteristic, is shown in blue in Figure 3.3 (d): after the SET operation, the low resistive state shows an exponential I-V relation. This trend can be related to oxide-based conduction mechanisms (Poole-Frenkel or trap assisted tunneling), typical when a thin oxide layer is found between the filament tip and the electrode. On the contrary, a fully connected filament could result in a metallic-like LRS. Therefore, it is reasonable to assume that the tip of the filament is not connected with the electrode, as previously reported in similar systems [117]. The modulation of the gap distance d_0 can explain the coexistence of abrupt and analog switching: the electric field forces the movement of the ions closer or farther from the electrode, changing the width d_0 and consequently the resistive state. The higher the write pulse amplitude and hence the electric field experienced by the device, the bigger the gap modification achieved. This mechanism is depicted in Figure 3.8. The filament is graphically represented as a sequence of blue spheres, suggesting that it comprises reduced oxide. The filament rupture is likely to occur at one of the Schottky contacts. Particularly the top electrode contact with the oxide is expected to be different as this contact was created under high temperature conditions, during the Pt evaporation on the active layer. It is possible that during this Pt evaporation and under vacuum, reduction of the first layers of the oxide occur and defects (oxygen vacancies) are created at the interface. These defects and other interface discontinuities/flaws are likely to play a key role during the resistance switching, acting as centres of filament rupture.

The Al doping seems not to affect the device's working mechanism, as the I-V curve of the doped device in Figure 3.3 (d), has a similar exponential trend in current for the LRS. This trend can be related to a partially connected filament, as in the undoped devices. Additionally, the electroforming is still required, thus pointing towards filamentary switching. Therefore, we assume that the mechanism remains unchanged in respect to the undoped film. The notable difference lies in the resistance operational range, which is generally higher for the Al doped devices, as shown in Figures 3.5 and 3.6. The presence of the Al $2p$ peak at 73.9 eV binding energy in the XPS spectrum,

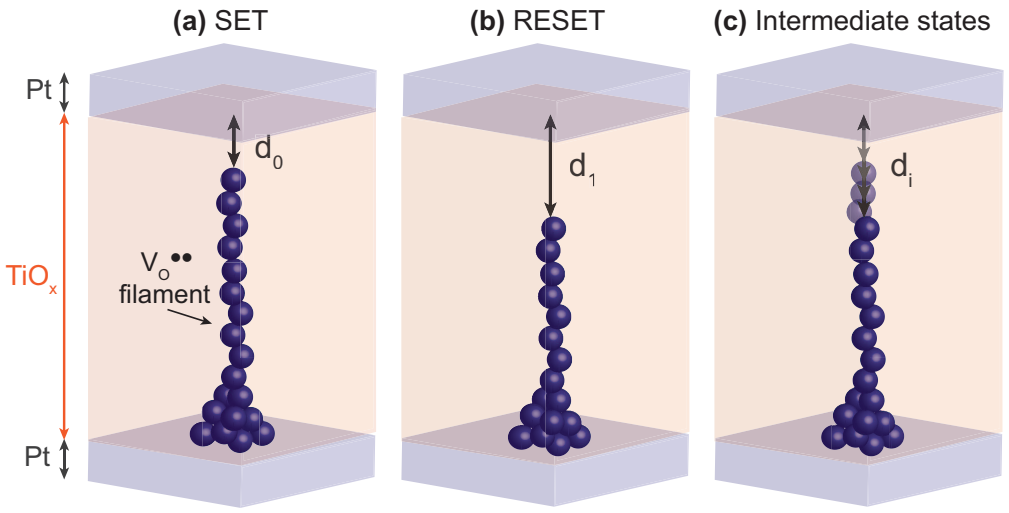

Figure 3.8: Concept of the filamentary mechanism in our TiO_x and TiO_x devices, depicting the aligned oxygen vacancies in the following configurations (a) SET, (b) RESET and (c) intermediate states.

suggests that Al ions are surrounded by O anions. The Al-O bonds, are likely to be uniformly distributed in the thin film due to the simultaneous sputtering deposition from the Ti and Al targets. Their presence could explain the increase in the resistance range between undoped and doped TiO_x by locally modifying the electronic structure, which is known from [79]. In addition, they could act as scattering centres for charge carriers thus possibly resulting in an increased resistance. It may also be possible that the initial filament growth could be affected by the presence of Al ions.

In addition, the reduction of the EF and switching voltages in the Al:TiO_x could be possibly attributed to the reduction of the oxygen vacancy formation energy as shown with DFT calculations [79]. According to a relevant work concerning HfO_2 (with similar valence electron configuration with TiO_x), weak p-type dopants like Al, are more likely to produce larger reduction of oxygen vacancy formation energy and more stable filaments [118].

3.9 Summary

In this chapter, it was demonstrated that Al-doping improves the switching characteristics of TiO_x-based RRAM cells. The Al:TiO_x-based devices were electroformed on average at -5.7 V compared to -6.4 V for the undoped devices. Both doped and undoped devices could support both analog and binary switching, subject to the pulsing scheme, in a repeatable manner for a large number of cycles. The majority of Al:TiO_x-based devices were operating in the 100-300 kΩ resistance regime and the switching voltages were typically of +1.2 V/ -1.0 V. The TiO_x devices were operating at higher potentials,

typically at +1.8 V/ -1.4 V (in analog mode) and +1.5 V/ -1.0 V (in binary mode). The relative standard deviation of resistance states was improved for doped devices. The device operation is realised through a filamentary mechanism, which didn't change with the Al doping. The valence difference between the Al and Ti could be the key for the reduction of the oxygen vacancy formation energy, therefore lowering the EF and switching voltages. These results are encouraging for the TiO_x RRAM optimisation, however, more in depth investigation has to be carried out to unravel the full potential of Al doping.

Chapter 4

Impact of ultra-thin Al_2O_{3-y} films in the performance of TiO_{2-x} RRAM

4.1 Introduction

Failure of RRAM devices and reliability issues have been discussed in the previous chapters. Engineering of the active layer by doping or addition of thin oxide buffer layers, are approaches that have been often adopted to tackle these issues. In chapter 3, reduction of switching and EF voltages in TiO_{2-x} RRAM devices by Al doping, due to possible reduction of oxygen vacancy formation energy triggered by the 4+ and 3+ oxidation states of Ti and Al, was demonstrated. In this chapter, a strategy that combines the two approaches is adopted; ultra-thin Al_2O_{3-y} buffer layers were incorporated between TiO_{2-x} thin films taking into account both 3+/4+ oxidation states of Al/Ti cations.

The addition of complementary oxide thin films [119, 120, 121] in RRAM has attracted a lot of interest lately, not only because of good performance indicators but also due to the simplicity of the device fabrication, which doesn't demand additional fabrication steps or sophisticated device architectures. In a study by Goux *et al.*, Al_2O_3 thin films were used in combination with the main active layer (HfO_2) for lower operation currents and switching voltage tuning [119]. Wang *et al.* used trilayer $Al_2O_3/HfO_2/Al_2O_3$ structures in RRAM devices, to improve the resistive switching characteristics by filament formation/rupture at the Al_2O_3/HfO_2 interfaces [122]. Wu *et al.* deposited a AlO_δ barrier layer on Ta_2O_{5-x}/TaO_y to enhance the switching performance with >10 μA switching current, $> 10^{11}$ cycling endurance and stable multilevel states [123].

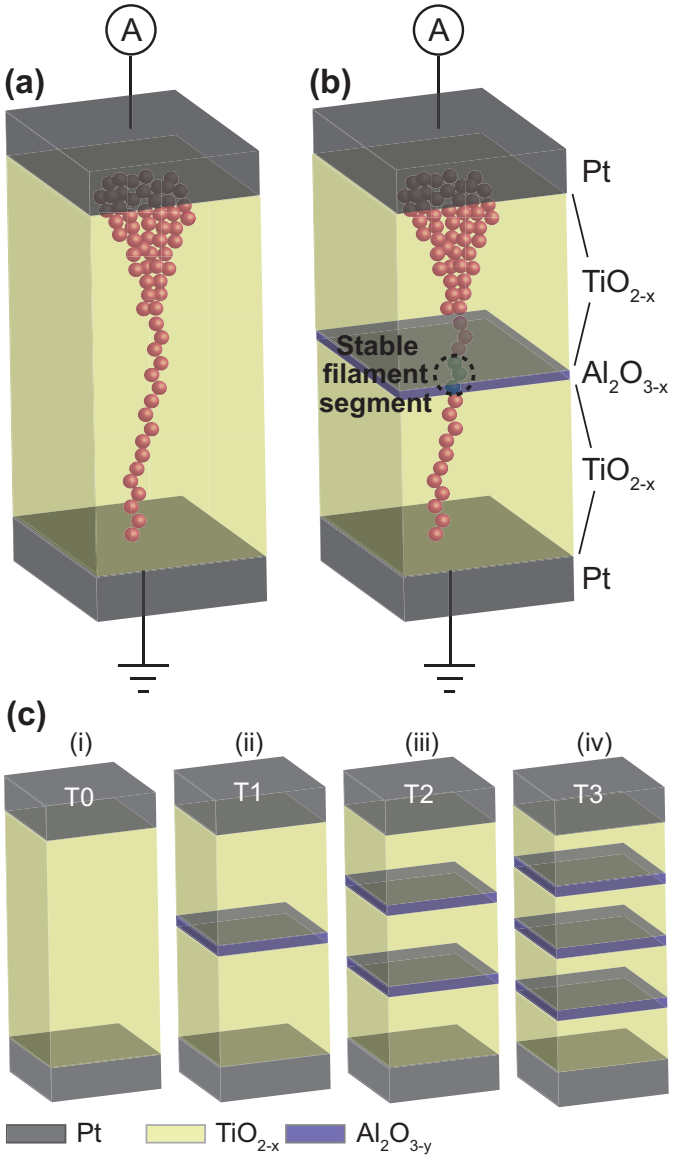

Figure 4.1: (a)Conceptual sketch of the filament formation in a TiO_{2-x}-based RRAM device and (b) in a $TiO_{2-x}/Al_2O_{3-y}/TiO_{2-x}$-based device, depicting a stable filament segment formed in the Al_2O_{3-y} layer. (c) Portrays the four different RRAM active layer configurations that were developed for this work.

In the present chapter, a different approach was followed, by incorporating thin Al_2O_{3-y} layers between TiO_{2-x} thin films. Figure 4.1 (a) displays a possible role of the Al_2O_{3-y} layers in the filament formation. A systematic study on these RRAM structures was carried out to investigate the effect of the Al_2O_{3-y} layers in the devices' EF, SET/RESET voltages as tested with DC voltage sweeping and pulsed voltage sweeping. Cycling endurance measurements were performed to examine the devices' robustness. The chapter is organised as follows. Section 4.5 includes the experimental details concerning the fabrication and characterisation of the Al_2O_{3-y} and TiO_{2-x} thin films as well as the RRAM devices featuring these layers. In section 4.3, the materials chemistry of the thin films is investigated with XPS surface measurements on individual Al_2O_{3-y} and TiO_{2-x}

thin films. In section 4.4, AFM scans on the Al_2O_{3-y} thin films were carried out to validate their continuity. XPS depth profiling was performed on the multilayer stacks to investigate the state of Al_2O_{3-y} layers in the stacks. Section 4.6.1 contains the RRAM device electrical characterisation with DC voltage sweeping and section 4.6.2 the characterisation with pulsed voltage sweeping. Section 4.6.3 includes the cycling endurance testing process and results. Finally, section 4.7 discuses the results and gives insights on the switching performance.

4.2 Reactive Sputtering of TiO_{2-x} and Al_2O_{3-y} thin films

TiO_{2-x} and Al_2O_{3-y} multilayer stacks were deposited by reactive sputtering (Helios XL, Leybold Optics) from Ti and Al metal targets (99.99% purity), on p-type Si chips cleaned in methanol and isopropanol. The settings during the TiO_{2-x} thin film deposition were 8 sccm O_2 and 35 sccm Ar at the Ti cathode, operating at 2 kW. The Al_2O_{3-y} thin films were deposited at 100 W power, with 15 sccm O_2 at the Al cathode and 25 sccm Ar at the plasma beam source. The thin films were deposited subsequently one after the other, without breaking the vacuum, to ensure better adhesion and better quality of the interfaces. The thickness of the TiO_{2-x} thin films was 11±1 and 23±1 nm and the thickness of the Al_2O_{3-y} thin films was approximately ∼2 nm, but the total thickness of each thin film stack was maintained 44-46 nm for fair comparison between RRAM devices comprising this thin film stacks as active layers. Figure 4.1 (c) depicts the 4 different stack configurations comprising the TiO_{2-x} and Al_2O_{3-y} thin films.

Table 4.1: Nominal thickness of the oxide thin films that compose the multilayer stacks.

	T0	**T1**	**T2**	**T3**
TiO_{2-x}	46 nm	23 nm	11 nm	11 nm
Al_2O_{3-y}		2 nm	2 nm	2 nm
TiO_{2-x}		23 nm	23 nm	11 nm
Al_2O_{3-y}			2 nm	2 nm
TiO_{2-x}			11 nm	11nm
Al_2O_{3-y}				2 nm
TiO_{2-x}				11 nm

Table 4.1 is listing the nominal thickness of the thin films used to compose the multilayer stacks. The thickness of each layer was evaluated by Spectroscopic Ellipsometry (Woollam M-2000) using the Cody-Lorentz model and the total thickness of each stack by Contact Profilometry (KLA-Tencor P11).

4.3 XPS characterisation of intermediate TiO_{2-x}, Al_2O_{3-y} thin films, and multilayer stacks

Thin film elemental characterisation was carried out using a Thermo Scientific Theta Probe Angle-Resolved X-ray Photoelectron Spectrometer with an Al Kα X-ray source (hv=1486.6 eV), operating at 2×10^{-9} mbar. The X-ray source operated at 6.7 mA emission current and 15 kV anode bias. Core level and survey spectra were collected over an area of 400×400 μm^2 with pass energy of 200 and 50 eV, respectively. XPS depth profile measurements were carried out using an argon ion gun operating at 1kV/1μA, etching an area of 2×2 mm^2 with each etching step lasting 40 s. Photoelectrons were collected at a base pressure of 5×10^{-7} mbar after every etching phase, from the exposed by the ion gun surface, until the whole stack was etched through and Si was the only detectable element. C 1s core level due to adventitious carbon, was always present in the spectra and was used for charge shift correction. All spectra were collected and analysed with the Avantage data system.

Figure 4.2 (a) displays the XPS survey spectra recorded from two reference TiO_{2-x} and Al_2O_{3-y} thin films deposited on Si, 23 nm and 2 nm thick, respectively. The TiO_{2-x} thin film survey (red), displays the following peaks from photoemission: O 2s, Ti 3p, Ti 3s, C 1s, Ti 2p and Ti 2s. The Ti 2p peak is a doublet, and can be ascribed to 4+ oxidation state, indicating that the TiO_{2-x} thin film is near-stoichiometric. The Al_2O_{3-y} thin film survey (black) exhibited the following peaks from photoemission: O 2s, Al 2p, Si 2p, Al 2s, Si 2s, C 1s, and O 1s. Due to the high surface sensitivity of XPS, Si 2s and Si 2p peaks were detected in the survey spectrum and are associated to Si phototoelectrons from the Si substrate. As XPS photoelectrons can be extracted only from the top ~5 nm of the sample, the presence of the Si peaks is another proof of the Al_2O_{3-y} thin film thickness. Due to the very low intensity of the peaks ascribed to Al, the stoichiometry of the Al_2O_{3-y} thin film was not assessed at this point.

Figures 4.2(b), (c) and (d) portray the Al 2p core level depth profiling spectra that were recorded from the samples T1, T2 and T3 accordingly. Grey-shaded squares are indicating the positions of the Al 2p peaks in each set of selected XPS spectra. The minimum allowed ion gun energy of 1kV/1μA and small etching step of 40 s were used to ensure that the intermediate Al_2O_{3-y} layers will not be etched through. Although the Al_2O_{3-y} layers are ultra-thin and despite the inter-diffusion between the subsequently deposited layers during sputtering, Al 2p core level is still detectable, confirming that the stack configuration is maintained. It is possible that a mixed phase of the two oxides could be formed at each interface, but due to the low deposition temperature we believe that a compound comprising both Al and Ti is unlikely. However, this argument cannot be currently confirmed due to the limitations of this technique. Another observation from the XPS depth profiling spectra was that Ti 2p intensity was minimum when the

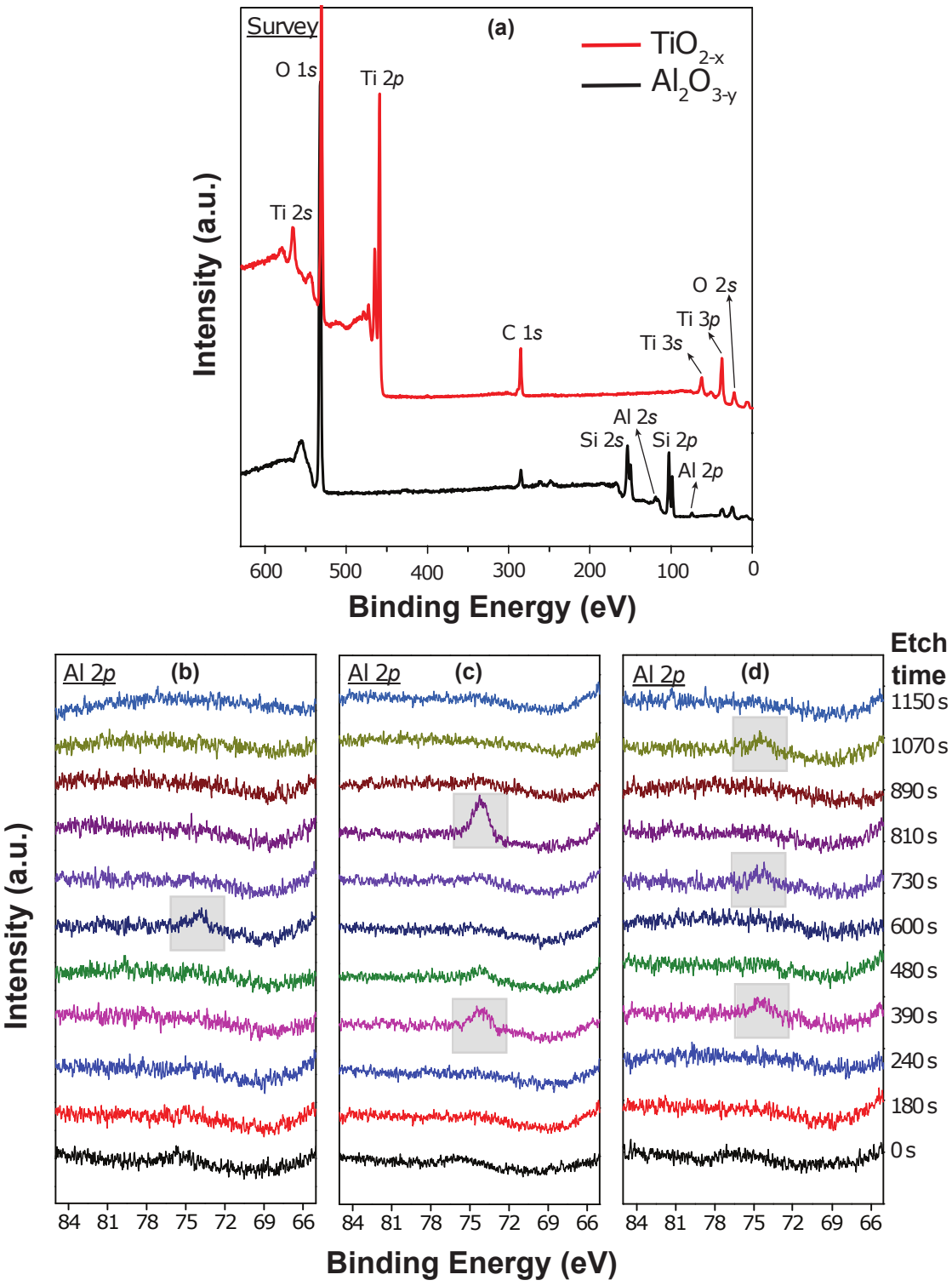

Figure 4.2: (a) XPS survey sprectra from single TiO_{2-x} and Al_2O_{3-y} thin films deposited on Si substrates, (b), (c) and (d) Al $2p$ XPS depth profile core level spectra from T1, T2 and T3 multilayer stacks, accordingly.

Al $2p$ was maximum. Similarly, the Al $2p$ peak was completely disappearing when etching in the TiO_{2-x}.

4.4 Assessment of the Al_2O_{3-y} thin film continuity

AFM measurements in contact more were carried out on Al_2O_{3-y} thin films using a Bruker MultiMode Nanoscope V system. The Al_2O_{3-y} thin films under study, were deposited on TiO_{2-x}, to emulate as much as possible the conditions as when the Al_2O_{3-y} thin films are part of the multilayer stacks. Si tips with a cantilever spring constant of 0.2 N/m and nominal tip radius <10 nm were used (BudgetSensors, Contact-G). Figure 4.3 displays the topography of the Al_2O_{3-y}, as realised from (a) a 0.5 μm, (b) a 1.0 μm and (c) 5.0 μm scan. The scans were substantially proved that the Al_2O_{3-y} thin films were amorphous and continuous, without visible pinholes or islands.

4.5 Multilayer RRAM Device Fabrication

RRAM devices were fabricated on Si/SiO_2(200 nm)/Ti(5 nm) supports. The electrodes and active layer were patterned by Optical Lithography. 10 nm Pt bottom and top electrodes were evaporated in an Electron-beam Evaporator followed by lift-off. The active layers were deposited by reactive sputtering as described in detail in section 4.2.

4.6 Multilayer RRAM Device Electrical Characterisation

40×40 μm^2 standalone RRAM devices were electrically characterised with a Keithley SCS-4200 Semiconductor Device Analyser. During the electroforming (EF) and DC I-V sweeps, the bias was applied on the top electrode, while the bottom electrode was connected to the ground. The devices were also characterised with pulsed voltage sweeping using ArC ONE^{TM}, a custom-made PCB-based system for device testing and characterisation [113]. The devices were electroformed and tested for switching using the algorithms presented in [112] and [111] accordingly, as well as for endurance.

4.6.1 DC Voltage Sweeping of Multilayer RRAM Devices

The finished 40×40 μm^2 standalone RRAM devices comprising the active layers T0-T4, were tested with DC voltage sweeping to assess their switching characteristics. The resistance of the pristine devices was in the range of GOhms and they needed an electroforming step to start switching repeatably between two resistive states.

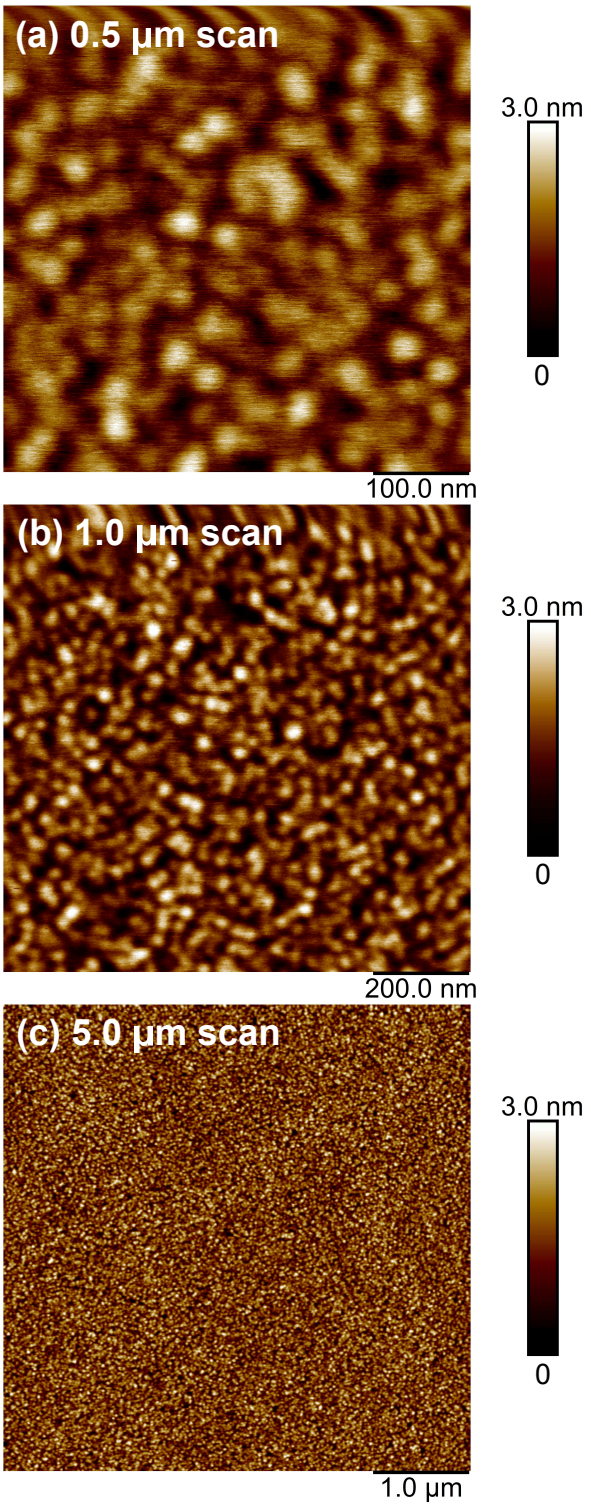

Figure 4.3: AFM topographies of an TiO_{2-x}/Al_2O_{3-y} thin film deposited on TiO_{2-x}, with scan size (a) 0.5 μm, (b) 1.0 μm and (c) 5.0 μm.

Figure 4.4 (a) portrays the box plots (n=10) of the devices with respect the number of Al_2O_{3-y} layers they comprise. The whiskers resemble the minimum/maximum values, the "x" markers the 5% and 95% percentiles, the upper/lower horizontal lines of each box the 25% and 75% percentile, the inner horizontal line the median and the square

marker the mean. The mean EF voltage increases slightly from -5.0 V to -5.2 V, -5.4 V and -5.3 V for the the devices comprising 1, 2 and 3 Al_2O_{3-y} layers, respectively, probably due to the very good insulating properties of Al_2O_{3-y}. However, EF voltage distribution is decreased in all devices that contain Al_2O_{3-y} layers, indicating that the addition of Al_2O_{3-y} layers can reduce the variability of EF voltages.

Figure 4.4 (b) displays the mean SET and RESET voltage plots from devices (n=5) that switched repetitively, with the whiskers indicating the standard deviation. The mean SET voltage dropped from 2.53 V for the T0 devices to 2.30 V, 2.18 V and 2.29 V for the devices T1, T2 and T3, accordingly. The SET standard deviation decreased for the T1 and T2 devices but deteriorated for the T3 devices. Similarly, the mean RESET voltage decreased from -2.00 V for the T0 devices to -1.53 V, -1.74 V and -1.66 V for the T1, T2 and T3, respectively. The RESET voltage standard deviation, follows a similar trend with the SET equivalent and decreases for devices T1, T2 and T3 but not with a clear trend. Among all configurations comprising Al_2O_{3-y} layers, T3 is possibly the one with the worst SET/RESET performance. Figures 4.4 (c), (d), (e) and (f) portray DC I-V characteristics from T0, T1, T2 and T3 devices after EF. Each panel displays three I-V characteristics, all from well behaved devices that switched repetitively. It can be observed, that devices of the same configuration had very similar switching behaviour, but this behaviour was found to vary among different configurations.

A typical EF step for every device configuration is displayed as inset in Figures 4.4 (c), (d), (e) and (f) and it is not revealing any particular difference associated with the number of Al_2O_{3-y} layers in the devices. Following the EF which was performed in negative polarity (and altered the device resistance from the pristine state to HRS), the voltage was swept from 0 to 3 V and back to 0 with 10^{-4} A current compliance, switching the devices from HRS to LRS. The devices' resistance switched back to HRS when the voltage was swept from 0 to -3 V and back to 0 with 10^{-3} A current compliance. SET was observed during a positive voltage sweep and RESET during a negative voltage sweep. Both the I-V characteristics exhibited a non-linear dependence between voltage and current. This suggests that either the filament does not have metallic properties, or that it is incomplete or not fully connected. SET usually emerged as an abrupt transition (with an exception in the case of T2 as shown in Figure 4.4 (e)), therefore, lower current compliance was used to protect the device from an unwanted hard-breakdown (HB). During hard-breakdown, the current dependence in the LRS was linear, possibly suggesting a fully connected filament to the electrode. Overall, devices T1 and T2 show improved SET and RESET voltages, small variability of I-V characteristics among different devices, at the expense of slightly higher EF voltage compared to T0 (4% and 8% for T1 and T2. respectively).

4.6.2 Pulse Voltage Sweeping of Multilayer RRAM Devices

Testing RRAM devices with DC voltage sweeping is known to induce device degradation rendering them useless [12, 107]. Therefore, we also performed pulse voltage sweeping to our devices, to reveal more insights about their resistive switching performance. The device EF was carried out using the algorithm presented in [112], performed in three voltage ramp stages (positive-negative-positive), each stage having a considerable effect on the device's resistance. Figure 4.5 (a) displays an example of a complete EF. The 3-stage EF was necessary to drop the device's resistance below 50 kOhm, which was a non-volatile regime where devices behaved more reliably. Different ramp polarity combinations were attempted, however, the above mentioned combination was chosen for achieving the highest EF yield. Following the EF, the devices were switched implementing the algorithm presented in [111]. The settings for the switching are depicted in Table 4.2. Devices from all categories, operated in different resistance regimes, but the most stable and repeatable ones usually operated in the range of 5-60 kOhm. Figure 4.5 (b) displays the mean switching voltages calculated from 5 typical (repeatable) devices from each stack category and whiskers represent the standard deviation of the switching voltages. It can be observed that the mean switching voltage and standard deviation decrease considerably for the devices T2 and T3.

Table 4.2: The settings used during electroforming and pulse voltage sweeping of the T0-T3 devices.

Parameter	Electroforming	Switching
Start write pulse amplitude (V)	0.2	0.2
Write pulse amplitude step (V)	0.2	0.1
End write pulse amplitude (V)	11	4
Write pulse width (ms)	0.1	0.1
Read pulse amplitude (V)	0.2	0.2
No. of write pulses	10	10
No. of read pulses	5	5
Series resistance (kOhm)	100	-
Resistance threshold (kOhm)	50	-

Figure 4.5 (c), (d), (e) and (f) display the resistive states of typical T0, T1, T2 and T3 devices, respectively, that operated within the range 5-20 kOhm. The gradual switching is dictated by the write pulse amplitude step which is 0.1 V in this case. As proposed in our previous work [124], a small write pulse amplitude step results in a smaller modification of the thin oxide gap between the conductive filament and the electrode, therefore creating these intermediate resistive states shown in Figure 4.5. Similarly, a higher write pulse amplitude step like 0.5 V, resulted in binary switching without intermediate resistive states [124].

4.6.3 Cycling Endurance of Multilayer RRAM Devices

The devices were tested for cycling endurance using the ArC ONE^{TM}, a custom-made PCB-based system for device testing and characterisation [113]. Programming pulses of fixed amplitude and width were applied in alternating polarities and the resistive state was assessed after each pulse at a read voltage of 0.2 V. As a result, two populations of measurements are de facto created: an 'HRS' population corresponding to read-outs following the positive (negative) polarity programming pulses and an 'LRS' population corresponding to the opposite polarity. The devices were robust and could maintain a satisfactory window between HRS and LRS. Two different kinds of flaws were identified. In some cases a write pulse failed to alter the resistive state and in other cases both HRS and LRS drifted towards higher resistance. To address these problems and assess the endurance of these devices in an automated and less user-invasive fashion, the collected raw data were post processed using MATLAB. Endurance performance was quantified using the following method: the user defined a minimum allowed HRS-LRS window ΔRS_{min} (in Ω) and then the algorithm would post-process the raw data. The algorithm would search pair-by-pair for the longest streak of continuous resistance reads for which $HRS_{min} - LRS_{max} \geq \Delta RS_{min}$. An example is shown in Figure 4.6. The cycling endurance results from 5 devices from each device stack were evaluated for the resistance windows: 1 kOhm, 3 kOhm, 10 kOhm and 30 kOhm and are depicted in Figure 4.7. Devices with 2 Al_2O_{3-y} layers performed on average better than the other combinations.

4.7 Discussion

During DC testing, T0 devices (TiO_{2-x}-based) showed a negative EF voltage of approximately -5.0 V (Figure 4.4 (a)), starting from a very high resistance in the range of GΩ. EF was achieved by a single negative polarity voltage sweep. T1, T2 and T3 devices comprised 1, 2 and 3 embedded Al_2O_{3-y} thin films, respectively. All configurations required EF to start switching between HRS and LRS, similarly to the T0 case. The EF voltages were slightly higher (4.2-7.5 %) compared to T0 devices (Figure 4.4 (b)), probably due to the very strong insulating nature of Al_2O_{3-y}. The EF was carried out as a single transition and not as a 2-step or a 3-step transition, regardless of the number of Al_2O_{3-y} layers the device comprised, is an indication that the Al_2O_{3-y} layers didn't act as barriers but as a source of ionic species. Subsequently, the devices operated by toggling their internal resistance with SET and RESET operations at positive and negative polarity, respectively. SET was abrupt and required a compliance current at 100 μA to prevent an irreversible hard breakdown of the device.

The abrupt nature of SET is indicative of an abrupt physical change occurring within the active layer, that could be explained with the formation of a conductive filament (CF) [125] in the active layer. This hypothesis is also corroborated by the presence of

the EF step in similar systems reported before [126, 19]. As discussed previously, from the exponential dependence of the I-V we can conclude that the filament does not have metallic properties but it can have semiconducting properties. Semiconducting filaments have also been reported previously in different oxide-based RRAM devices [72]. Another possibility is that there is a remaining oxide gap between the CF and the electrode. The carrier conduction through this gap possibly explains the non-linear dependence of the I-V curves. This argument has been previously reported for TiO_{2-x} systems [117]. The RESET operation is likely driven by thermal effects gradually disrupting the CFs, as also reported in similar oxide systems [72, 8]. Hence, the most feasible mechanism involves the drift of ions (oxygen vacancies) injected during the EF, creating a conductive path within the active layer.

The addition of the thin Al_2O_{3-y} layer in the device's active layer could be possibly adding Al cations in the ionic species facilitating the switching. The dissociation energy (D°_{298}) of the Al-O bonds is 501.9±10.6 $kJmol^{-1}$ compared to 666.5±5.6 $kJmol^{-1}$ of the Ti-O bonds [127], fact that could support the argument about the mobile Al cations. Moreover, it was previously suggested that the presence of Al_2O_{3-y} in a TiO_{2-x} matrix enhances the formation of oxygen vacancies resulting in lower switching voltages [124].

The EF in pulsed characterization follows a different pattern, as shown by Figure 4.5 (a). The triplet of pulsed voltage ramps is essential to achieve a complete EF for all device stack configurations. Following EF, the devices were able to perform a stable analog resistive switching. The presence of the EF still appears to be consistent with the observations during the DC electrical characterization. Therefore, the filamentary hypothesis for the resistive switching appears corroborated. The gradual modification of the resistance could be associated with the tuning of the oxide gap between the filament and the electrode, as we previously reported for a similar system [124].

The difference in EF between DC and pulsed operation could be sought in the different contributions of the electric field and Joule heating. During a DC voltage sweep, the voltage never drops to 0 between each step but continuously increases. The sweep is effectively a voltage staircase in which each step lasts for 1 ms. During pulsed operation, a non-invasive read pulse scheme is implemented to access the device's resistance. The reading scheme comprises 5 read pulses with a total pulse duration and inter-pulse delay, adding up to $\sim$ 30 ms between write pulses. The estimated total energy delivered to the device due to Joule heating is in the order of 10^{-5} J, taking into account a resistive state of 200 $k\Omega$ at -5 V with 1 ms step. Additionally, the energy calculated is likely to be underestimated since just voltages in the vicinity of the threshold voltage are considered. The same approach applied to pulsed operation leads to a value in the order of 10^{-10} J. The larger inter-pulse time during pulsed operation could favour the dissipation of this energy. On the contrary, a continuous staircase would favour the heat build-up in the system.

The difference in the available energy could result in different contributions from the electric field and heat. In the case of DC operation, the generated heat rapidly induces a soft-breakdown in the oxide, without the requirement for multiple steps. Also, the heat role is corroborated by the presence of a compliance current that limits the current flow in the device, therefore preventing a hard breakdown. The 30 ms delay, allow the heat to be dissipated, pointing to an electric field-driven EF. In addition, TiO_{2-x}-based systems have been reported previously as capable of electric field-based EF [128]. The multi-step nature of EF shown in Figure 4.5 (a) could be ascribed to the formation of multiple filaments within the oxide film. A similar mechanism has been suggested to explain the multiple steps achieved during switching of other oxide systems [129].

In conclusion, the device operation is regulated by the formation of a conductive path within the oxide layer, which is boosted by the presence of the Al_2O_{3-y} layer. Al_2O_{3-y} can increase the ion/oxygen vacancy concentration available in the active layer creating a conductive path achieved by inter-diffusion during the EF. Relevant differences in the EF operations are reported, involving different driving mechanisms. During pulsed operation, EF could be achieved due to electric field-driven phenomena with little effects due to Joule heating. However, during DC operation filament formation could me more affected by Joule heating.

4.8 Summary

In this chapter, it was demonstrated that the incorporation of ultra-thin Al_2O_{3-y} buffer layers in TiO_{2-x} RRAM can aid with reducing the devices' switching thresholds. The nm thin Al_2O_{3-y} did not introduce discontinuities or any other undesirable effects in the RRAM devices. The ultra-thin layers were detected in the bulk of the multilayer stacks, using XPS. XPS depth profiling characterisation of the multilayers, gave a qualitative indication of the Al_2O_{3-y} state by detecting Al $2p$ in the expected etching levels. The Al_2O_{3-y} layers acted in a rather homogeneous way and not as solid barriers inside the active layer.

The EF voltages using DC voltage sweeping slightly increased in all devices containing Al_2O_{3-y} layers, fact that could be attributed to the strong insulating properties of Al_2O_{3-y}. The switching voltages of the devices comprising Al_2O_{3-y} layers were +2.0/-2.0 V and +1.1/-1.1 V, tested with DC voltage sweeping and pulse sweeping, respectively. The Al_2O_{3-y} layers possibly played a double role, injecting excess oxygen vacancies but also enhancing a more repeatable and stable filament formation/eruption. Preliminary cycling endurance results suggested that Al_2O_{3-y} layers possibly enhanced the devices' endurance but more work on this matter has to be carried out to reveal the full potential of these devices. The non-volatile, analog mode of switching of the devices

is not limiting the devices' potential but can make them good candidates for a variety of applications in neuromorphic computing.

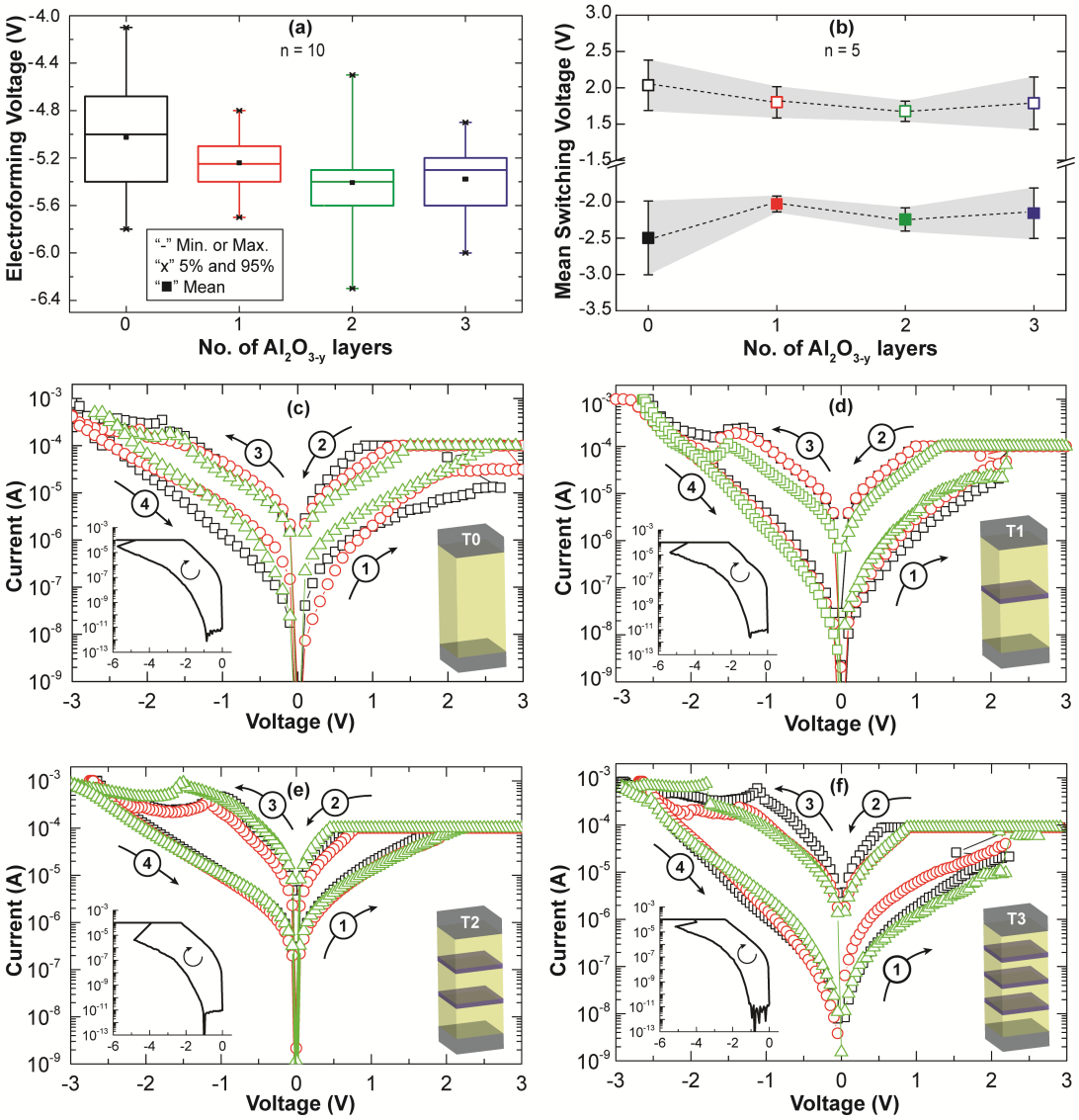

Figure 4.4: (a) Box plot of electroforming voltages (whiskers indicate the min/-max values, "x" markers the 5%/95% percentiles, upper/lower lines of each box the 25%/75% percentiles, inner line the median and square marker the mean), (b) mean SET and RESET voltage scatter plots (whiskers are indicating the standard deviation) concerning the number of Al_2O_{3-y} layers in each device configuration. (c), (d), (e) and (f) display I-V charactersitics obtained from the device stacks T0, T1, t2 and T3, respectively. The colours black-red-green of the I-V curves indicate the order of the measurement after the EF, as 1st-2nd-3rd. Insets portray the typical electroforming step of each device configuration.

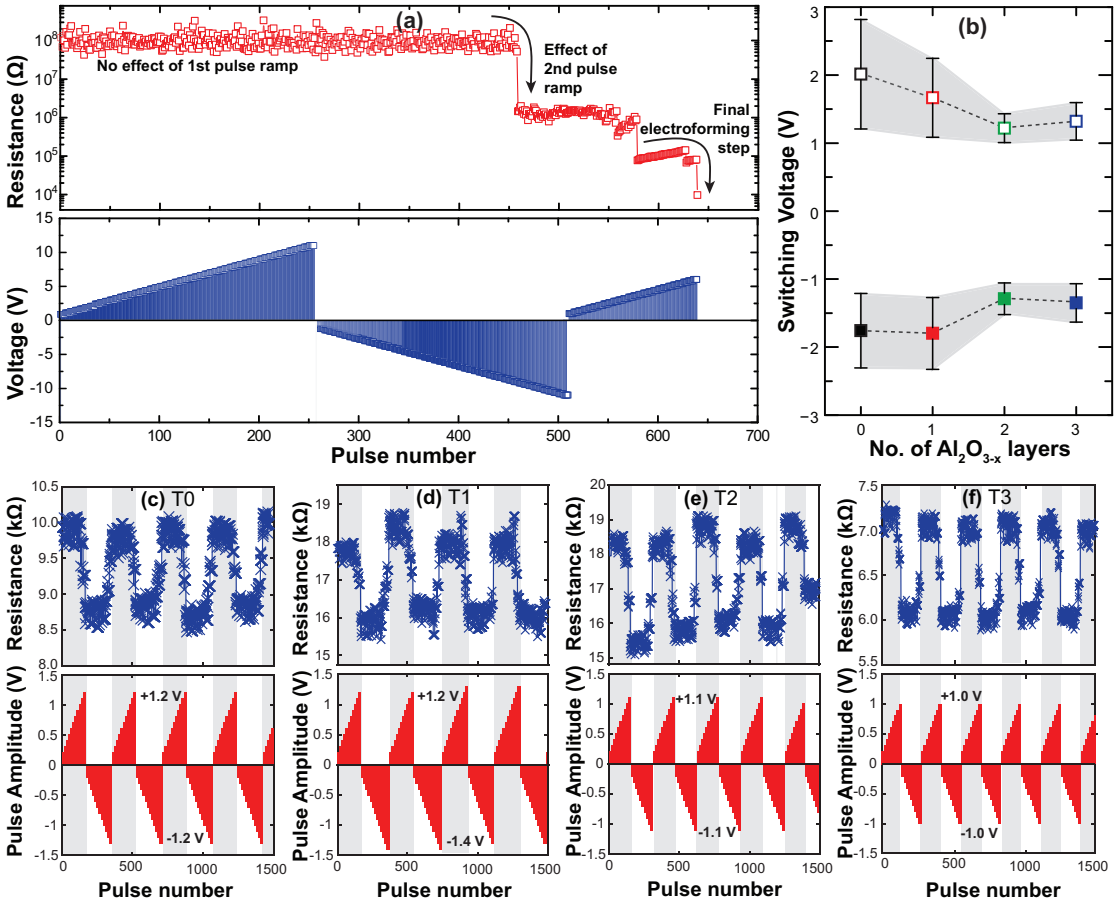

Figure 4.5: (a) Example of a three-stage EF, portraying the effect of each stage on the device's final resistance state and (b) the switching voltage scatter plot for all different device stack configurations. (c), (d), (e) and (f) are typical resistive state distributions from well-behaved devices T0, T1, T2 and T3, respectively. These devices were selected because they switched in similar resistance regimes.

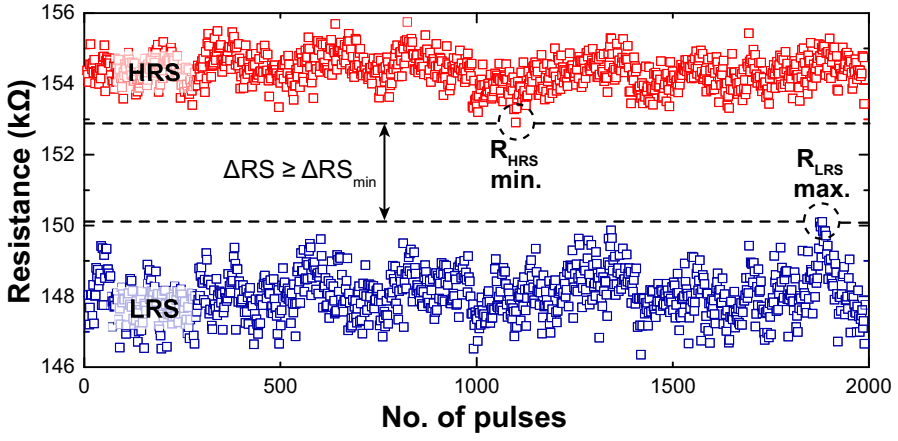

Figure 4.6: Example of the MATLAB algorithm concept of operation. Data from a T0 device are shown as an example.

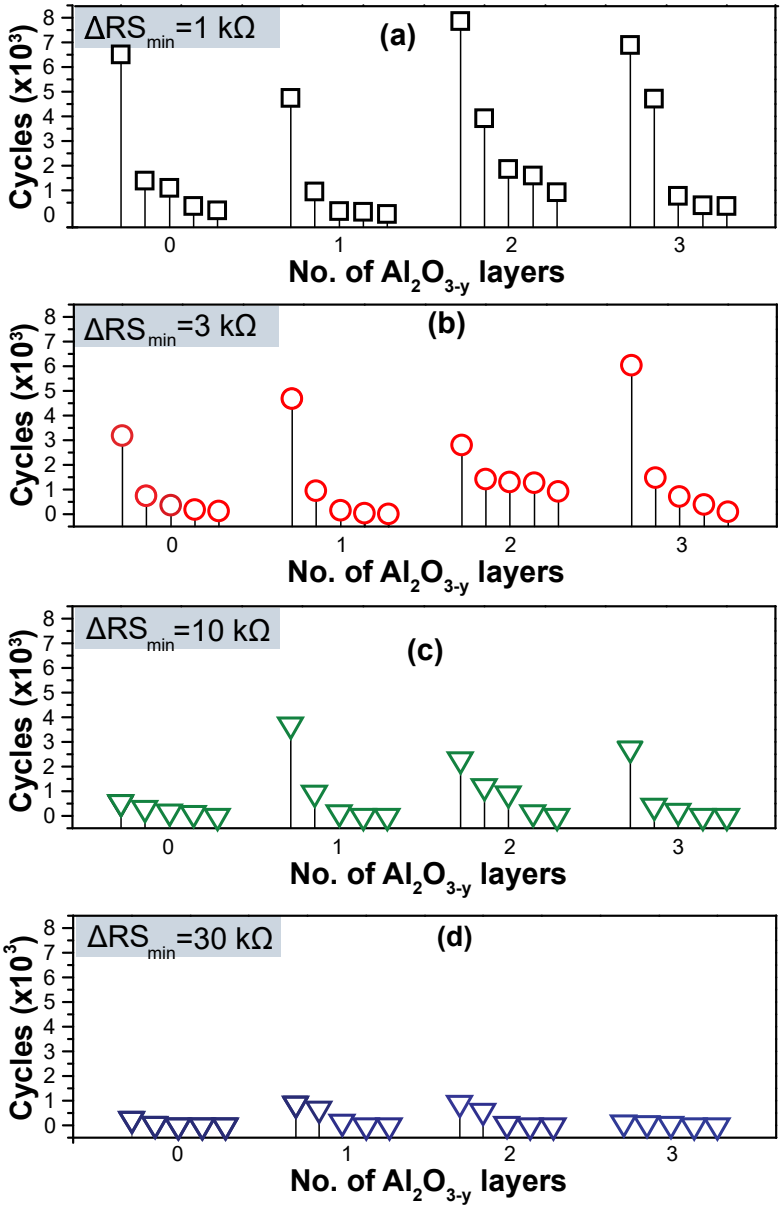

Figure 4.7: Cycling endurance results from samples T0-T3 for resistance windows: (a) 1 kΩ, (b) 3 kΩ, (c) 10 kΩ and (d) 30 kΩ.

Chapter 5

Resistive switching performance of Al:TiO_{2-x}-Nb:TiO_{2-x} bilayer RRAM devices

5.1 Introduction

In chapter 3 it was demonstrated how Al doping improves the performance of TiO_{2-x} RRAM devices. The 3+ oxidation state and ionic radius were the two basic criteria based on which Al was selected among other options available. The initial concept was that Al would introduce oxygen vacancies if Al ions were to replace Ti in the TiO_{2-x} matrix enabling p-type conductivity [79]. In the case of undoped TiO_{2-x}, each Ti cation is bound to four oxygen anions and in Al_2O_{3-x}, each Al is bound to three oxygen anions. In case of substitutional doping of Al in TiO_{2-x}, the Al coordination would still be 3, as it is strictly forbidden by the rules of coordination chemistry to exceed this number of bonds. The unbound oxygen would be free and the presence of Al would therefore create a p-doped active layer of TiO_{2-x}.

In that context, the idea to use a 5+ cation as a dopant in TiO_{2-x} occurred. V, Cr, Co, Ni, Cu and Nb are pentavalent and n-type dopants in TiO_{2-x}. Nb was selected as it had several similarities with Ti, it was readily available and easy to deposit with reactive sputtering. Interestingly, Nb had very similar ionic radius with the Ti, as shown in table 5.1. Moreover, Nb can have +3, +4 and +5 oxidation states and therefore can form conducting NbO, n-type NbO_2 (distorted rutile structure), insulating Nb_2O_5 (amorphous or crystalline), and several metastable oxides. The ionic 'compatibility' of Nb with Ti led to many ideas on possible device structures and possible interesting mechanisms that could benefit the devices' performance.

Table 5.1: The coordination and ionic radii of Ti and Nb (*) cations in various oxidation states.

Charge	Coordination	Ionic Radius (Å)
2	VI	0.86
3	VI	0.67 / 0.72*
4	IV	0.42
	V	0.51
	VI	0.605 / 0.68*
	VIII	0.74 / 0.79*
5	IV	0.48*
	VI	0.64*
	VII	0.69*
	VIII	0.74*

This chapter, aims to discuss the suitability of Nb-doped TiO_{2-x} thin films in RRAM devices as resistive switching cores. Furthermore, this chapter aims to study devices comprising Nb-doped TiO_{2-x} and Al-doped TiO_{2-x} thin films in a bilayer structure and the possibility of them showing a diode-like behaviour. RRAM devices that can have a p-n junction formed at the interface of the 2 doped TiO_{2-x} thin films (one n-type and the other p-type) still does not exist in literature and is a very intriguing concept. The interest of such a breakthrough would open the door of RRAM to more applications, like amplifiers and switches.

5.2 Deposition of Nb-doped TiO_{2-x} thin films with varying Nb content

The first step in this study was to create a series of Nb-doped TiO_{2-x} thin films and characterise the chemical composition, to optimise the recipe with the desired Nb-concentration. A series of Nb-doped TiO_{2-x} thin films were deposited by reactive sputtering from high purity Nb and Ti metal targets. The substrates were 1.5×1.5 cm p-type Si chips, rinsed with acetone and isopropanol before use. The Nb and Ti targets were fitted on the DC and RF magnetrons, respectively. The sputtering settings used for the deposition of these thin films are depicted in Table 5.2. It can be seen that the power applied on the Ti target remained stable, while the power at the Nb target varied to yield different Nb % at. concentrations. The gas flows shown in the table are supplied inside the target area, but additional oxygen plasma is supplied in the sputtering chamber by the plasma beam source. The actual temperature during the sputtering deposition was 85-88 °C, thus, the as-deposited thin films were amorphous.

Table 5.2: Sputtering settings during the deposition of the Nb-doped TiO_{2-x} thin films.

Parameters	Ti target	Nb target
Power (W)	2000	0-225
Pressure (mbar)	5 x 10^{-5}	
Temperature (°C)	85-88 (act.)	
O_2 flow (sccm)	8	-
Ar flow (sccm)	35	10

5.3 Analysis of Nb % at. concentration in the Nb-doped TiO_{2-x} thin films by XPS characterisation

The as-deposited thin films were measured using a Thermo Scientific Theta Probe Angle-Resolved X-ray Photoelectron Spectrometer with an Al K X-ray source (hv=1486.6 eV), operating at 2×10^9 mbar. The emission current and anode bias of the X-ray source were 6.7 mA and 15 kV, respectively. Core level and survey spectra were collected over an area of 400×400 μm^2 with pass energy of 200 and 50 eV, accordingly. The binding energy step was 0.1 eV for the survey spectra and 0.02 eV for the core level spectra. A survey spectrum, O $1s$, Ti $2p$, Nb $3d$ and C $1s$ core level spectra were recorded for each of the samples. C $1s$ was always present due to adventitious carbon and was used for charge shift correction.

Figure 5.1 (a) portrays the survey spectra recorded from each of the samples, with the main peaks detected, noted on the top. The charge shifting of C $1s$, that was always < 1.0 eV, was corrected to 285.0 eV. Following this correction all spectra were normalised with respect to O $1s$, being the peak with the highest intensity. Figure 5.1 (b) displays Nb $3d$ core level spectra recorded from each of the samples. With increasing power at the Nb target, the intensity of the Nb $3d$ increased, indicating an increasing Nb % at. concentration in the thin films. Moreover, from the survey spectra of Figure 5.1 (a), it can be seen that as the power at the Nb target increased, the intensity of the Ti $2p$ signal (binding energy range 456-466 eV) was suppressed.

Detailed peak fitting and quantification was performed in all data. Figure 5.2 (a), (b) and (c), display the fitting of Nb $3d$, Ti $2p$ and O $1s$, carried out for the most heavily doped sample, Nb-8. Nb $3d$ is a doublet with a 3/2 and a 5/2 spin-orbit splitting components, having 2.7 eV peak separation. These doublets, have also specific peak area ratio and equal FWHM, that were taken into account for the fitting. The main peaks, $3d_{3/2}$ and $3d_{5/2}$ appearing at 210.3 eV and 207.5 eV, represent Nb cations with 5+ oxidation state. The shoulder appearing at 205.8 eV, is also a $3d_{5/2}$ component and represents a small population of Nb cations with 4+ oxidation state. The $3d_{3/2}$ component for the 4+ oxidation state was not fitted. The contribution to that component was so small that this peak was not detected. The peak binding energies of Nb, were compared with

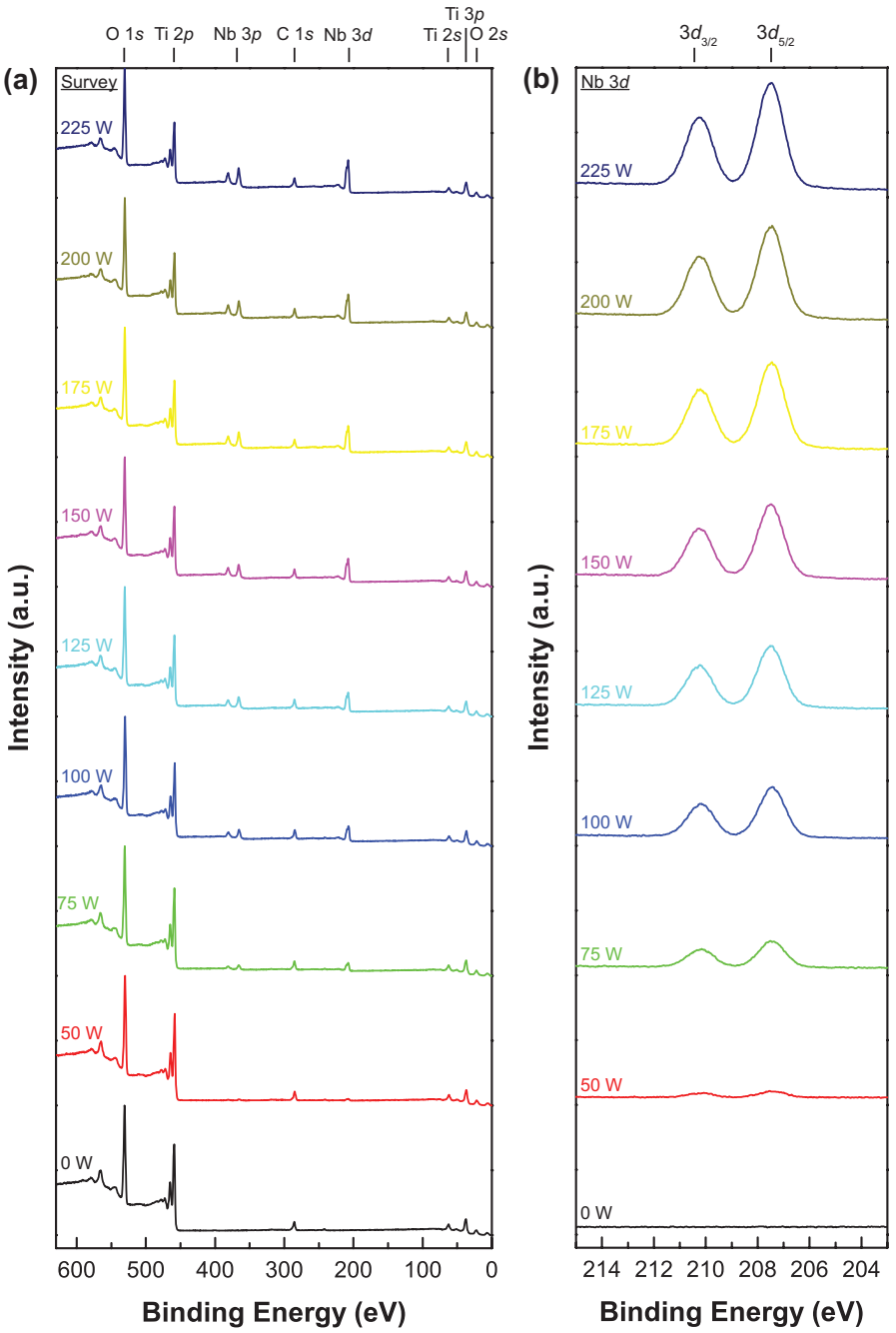

Figure 5.1: XPS (a) survey spectra from the Nb-doped TiO_{2-x} thin films deposited with varying power at the Nb target. Representative peaks from C, O and Ti are present in all spectra, while the Nb $3p$ and $3d$ core level peaks become more significant after 75 W power at the Nb target. (b) Nb $3d$ core level spectra, recorded from Nb-doped TiO_{2-x} thin films, showing the Nb $3d$ core level peak growing in intensity with increasing power at the Nb target.

equivalent data from literature [115]. The most important information from fitting this core-level were: (i) that the chemical environment of Nb was oxygen, (ii) the oxidation state of Nb was 5+ (Nb_2O_5) and (iii) that there is a small population of Nb with 4+ oxidation state. Therefore Nb is in the form of an oxide, very lightly reduced, that could

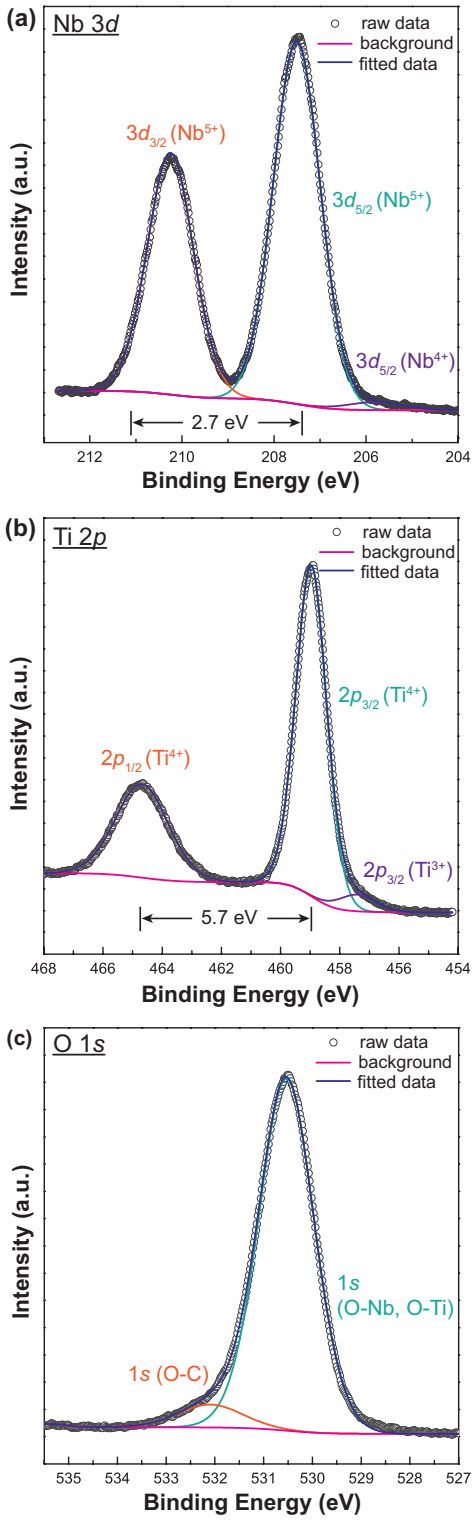

Figure 5.2: Detailed fitting of the (a) Nb 3d core level peak revealing a small population of Nb^{4+} species, (b) Ti 2p with a small population of reduced Ti^{3+} species and (c) O 1s core level spectra, deconvoluted in metal–bound and C–bound O. The spectra were recorded from the sample with the highest Nb 3d % at. concentration, Nb-8.

be represented in the form of Nb_2O_{5-y}.

Figure 5.2 (b) portrays the fitting carried out on the Ti $2p$ core level. Ti $2p$ is also a doublet with 1/2 and 3/2 spin-orbit splitting components, having a peak separation of 5.7 eV. The main peaks at 464.7 eV and 459.0 eV represent Ti cations with a 4+ oxidation state in the TiO_2 form. The shoulder at 457.4 eV, is the 3/2 spin-orbit splitting component, representing Ti cations with 3+ oxidation state in the reduced form TiO_{2-x}. Similarly to the Nb $3d$ core level, the 1/2 spin-orbit splitting component representing Ti cations in 3+ oxidation state is not detected, due to being very low in intensity.

Figure 5.2 (c) depicts the peak fitting carried out on the O $1s$ core level of the same sample. It was fitted as a single peak, as s orbital has a spherical shape and there are no different spin states. The peak at 530.5 eV stands for bonds of O with metal cations, Nb and Ti in this case. The fitted peak at 532.9 eV stands for O-C bonds and is related to oxygen anions bonded to organic adsorbates of the thin film surface. Since this oxygen is not related to the oxide under study, it was fitted but was not included in the quantification.

Table 5.3: XPS quantification table of the Ti, O, and Nb % at. concentration of each sample.

Sample ID	**Power at Nb target (W)**	**Ti at. %**	**O at. %**	**Nb at. %**	**Impurities**
Nb-0	0	24.8	56.9	0	18.3
Nb-1	50	24.0	57.6	0.5	17.9
Nb-2	75	22.4	56.3	2.1	19.2
Nb-3	100	20.6	56.6	4.1	18.7
Nb-4	125	19.9	58.0	5.1	17.0
Nb-5	150	18.9	57.8	6.1	17.2
Nb-6	175	18.4	58.1	7.0	16.5
Nb-7	200	17.5	57.6	7.6	17.3
Nb-8	225	16.7	57.3	8.5	17.6

The Nb, Ti and O atomic concentrations were calculated with a precision of ± 1 eV. For the doublets Ti $2p$ and Nb $3d$, although both peaks were fitted, only the peak with the highest intensity was quantified, to ensure their concentration is not over-quantified. As seen in Table 5.3, the total concentration of the three elements doesn't add up to 100% because adventitious carbon was taken into account in the quantification. The Nb concentration spans from 0 to 8.5 % at., while the Ti concentration gradually decreases from 24.8 to 16.7 % at., with increasing power at the Nb target.

5.4 Fabrication of Al- and Nb-doped bilayer TiO_{2-x} RRAM devices

RRAM devices were fabricated with optical lithography, using the same process that was described in Chapter 3. The 40×40 μm^2 devices comprised 10 nm Pt bottom and top electrodes, deposited by E-beam evaporation. The following active layers were deposited, with total thickness 45 nm each: (i) Al:TiO_{2-x}, (ii) Nb:TiO_{2-x} and (iii) Nb:TiO_{2-x}/Al:TiO_{2-x}. The later comprised equal thickness of each oxide, approximately 23 nm. A schematic representation of the device stacks are shown in Figure 5.3.

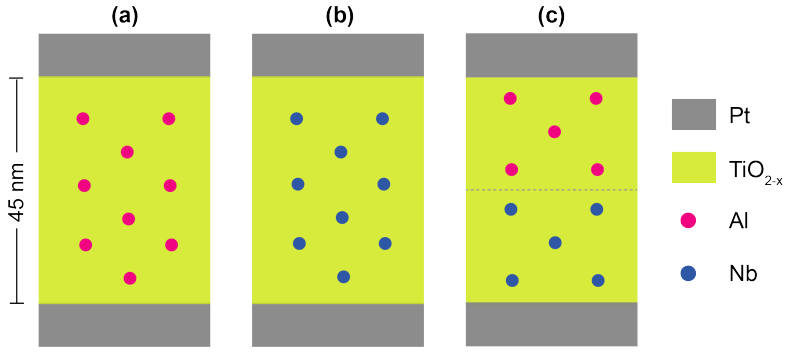

Figure 5.3: The fabricated device stacks: (a) Al:TiO_{2-x}, (b) Nb:TiO_{2-x} and (c) Nb:TiO_{2-x}/Al:TiO_{2-x}.

The Al:TiO_{2-x} thin active layer was co-sputtered from an Al and Ti targets , with 50 W applied at the Al target and 2000 W applied on the Ti target. Similarly, the Nb:TiO_{2-x} active layer was deposited with 90 W applied at the Nb target and 2000 W on the Ti target. The same settings were used for the bilayers but in that case, a lower sputtering time was set to yield lower thickness. The bilayer stack was formed by depositing the Nb:TiO_{2-x} thin film first and subsequently the Al:TiO_{2-x} thin film, without breaking the vacuum. It was assumed that since the devices are symmetric, there is no dependence of the order of the deposition and therefore the opposite stack was not fabricated.

5.5 DC characterisation of Al:TiO_{2-x} - Nb:TiO_{2-x} bilayer devices for diode-like conduction

The bilayer devices were tested for their DC-IV characteristic to investigate whether there is a p-n junction formed at the interface. When a bias is applied on a p-n junction, it behaves like a diode, the characteristic curve of which is shown in Figure 5.4 (a). Basic requirement of the p-n junction is that the two thin films that are in contact are p- and n- doped with Nb an Al, respectively.

Efforts to characterise the type of conductivity were carried out using the Van der Pauw technique. Square patterned thin films of the TiO_{2-x}, individually doped with Al and

Nb were deposited on glass substrate and Pt contacts were added on each corner with silver paint. The efforts to measure current and identify the type of carrier on each thin film failed for numerous reasons. The most significant was the fact that the thin films were too insulating and the current was so low that it was beyond the tool's capability to measure. Therefore, the only way forward was to test the bilayer devices and check the characteristic.

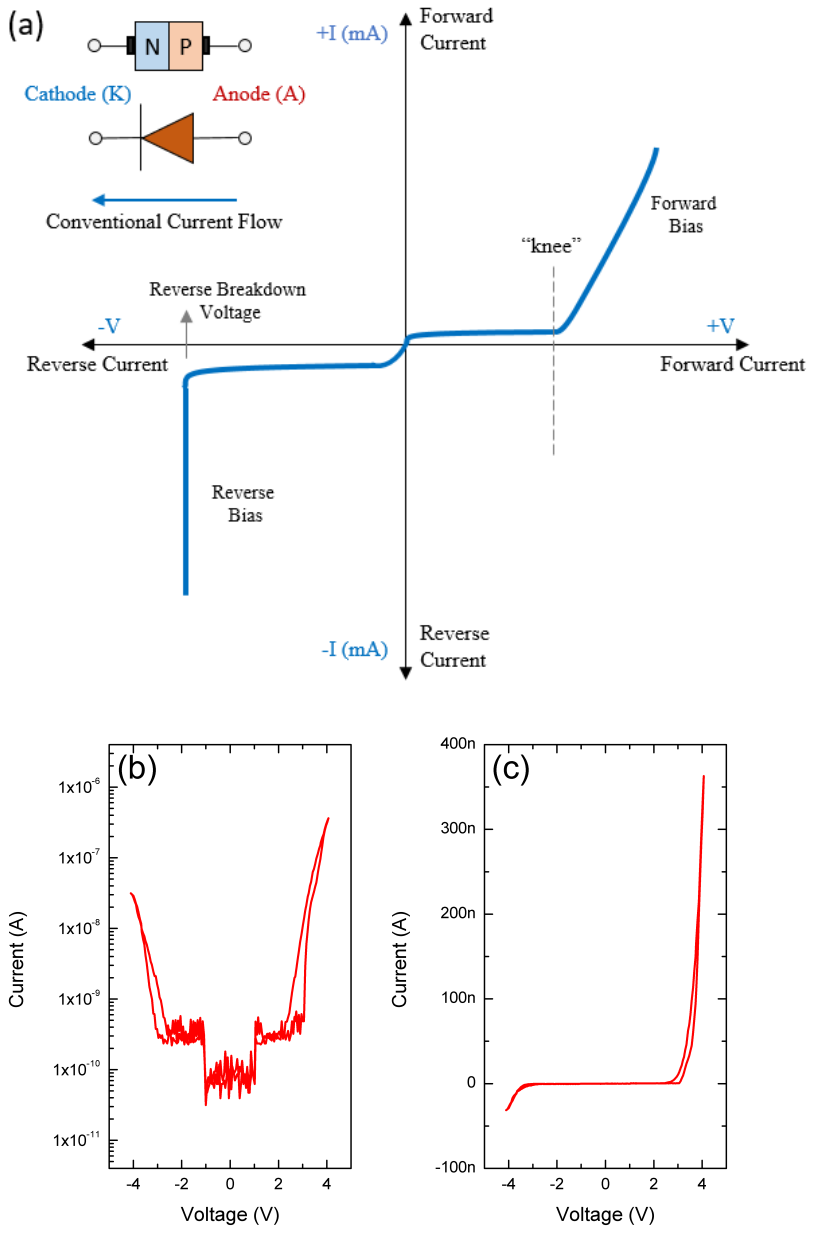

Figure 5.4: (a) Typical DC I-V characteristic of a diode, typical I-V obtained emperimentally from bilayer devices plotted on (b) logarithmic and (c) linear scale.

Bilayer devices were tested by sweeping the voltage from 0 to +4 V and back to 0 and then, from 0 to -4 V and back to 0. These devices in specific, had the Al:TiO_{2-x} thin

film deposited first and the Nb:TiO_{2-x} deposited subsequently on top. With the p-type material on top and with the bias applied always on the top electrode, a positive sweep would be the forward bias. During a forward bias, the holes of the p-type thin film would be pushed towards the interface and likewise, the electrons of the n-type thin film would be also pushed towards the interface, forming a small depletion zone. Below the threshold (the "knee" as indicated in figure 5.4 (a)) we would expect a low current flowing across the device. At the threshold voltage, the electrons and holes would start recombining and an increase in bias would be observed. However, as figure 5.4 (b) and (c) display the current is very low, in the nA range which is also the measurement limitation of the tool.

During a reverse bias (negative current on the top electrode - Nb:TiO_{2-x} thin film), the electrons and holes would be pushed towards the opposite direction, the electrodes, resulting in wider depletion zone. This p-n junction arrangement would result in the behaviour shown on figure 5.4 (a) for reverse biasing. However, this behaviour was not obtained experimentally proved either. The existence of the p-n junction was not proven, however, physical and practical explanations were investigated. The most possible scenario was that there was no p-n junction because there were no p- and n-type of thin films in the first place. Possibly, the method of deposition did not allow the "doped" ions Al and Nb to replace native Ti ions. On the contrary, the Al and Nb formed immediately oxides, as the deposition was carried out in an oxidising atmosphere.

The initial hypothesis about a p-n junction at the interface of the two oxides with diode behaviour has been experimentally disproved. The fabricated devices were still interesting for studying the switching behaviour of TiO_{2-x} RRAM. Nb was never used before as a dopant in TiO_{2-x} thin films deposited by reactive sputtering for RRAM or other electronic applications. A full testing routine was carried out in Al:TiO_{2-x}, Nb:TiO_{2-x} and bilayer devices with DC and pulsed sweeping.

5.6 DC characterisation of Al:TiO_{2-x}, Nb:TiO_{2-x} and bilayer devices

The devices were tested for their DC I–V characteristics with ArC ONE^{TM}, a custom-made PCB-based system for device testing and characterisation [113]. This system had a DC sweeping function, equivalent to a Keithley testing system that was ideal for quick and efficient testing of large batches of devices at a fraction of time. A probe card was used to allow on-wafer interfacing of an array of stand-alone devices. Applying a biasing scheme like EF or DC sweeping was a lot faster and efficient, as navigation from one device to another is usually a factor that makes the overall testing process slow. Another advantage was that by reading at once the whole array of devices, the devices in the

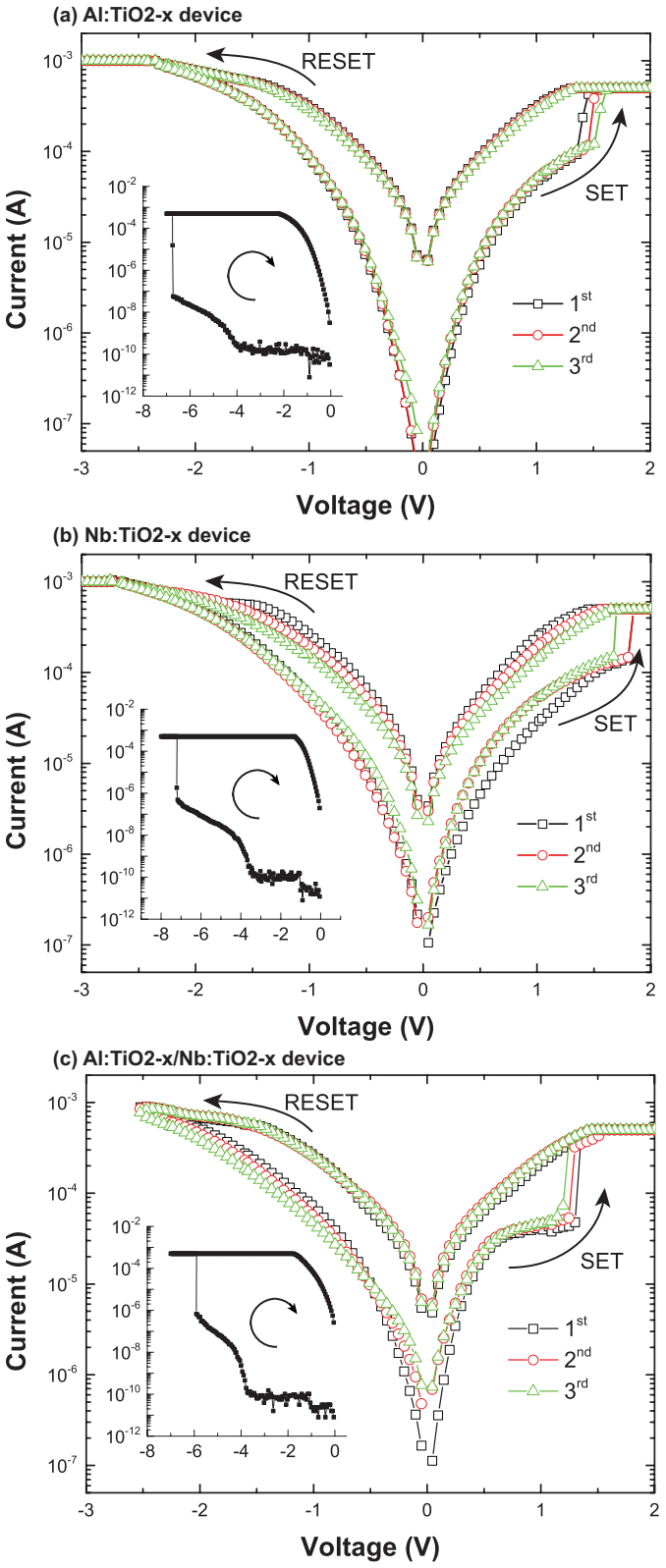

Figure 5.5: Typical DC electroforming (insets) and I-V characteristics for: (a) Al:TiO_{2-x}, (b) Nb:TiO_{2-x} and (c) Nb:TiO_{2-x}/Al:TiO_{2-x} devices. Each set of I-V characteristics comes from different devices of the same active layer to show the statistical significance of each switching behaviour.

preferred resistance state could be easily selected over others and tested efficiently at mouse-click.

Initially, all different device stacks were electroformed with a negative polarity voltage sweep, from 0 V to -8 V and back again to 0 V. A cut-off current of 5×10^{-4} A was used to protect the devices from high currents. The voltage step amplitude was 0.05 V and the width 10 ms, respectively. Figure 5.5 insets depict the stage of electroforming, which was similar in all devices, regardless the doping type. During the electroforming, the device resistance rapidly dropped from the GOhm range to 30-100 kOgm range as a single-step transition.

Following EF, the devices were tested by DC voltage sweeping for their I-V characteristic. The resistance switching was initiated with a positive voltage sweep from 0 V to +2 V and back to 0 V with a current cut-off of $5 \times 10^{-}4$. This was a SET, lowering the device's resistance. A subsequent negative sweep from 0 V to -3 V and back to 0 V with a current cut-off of 1 mA was increasing again the resistance of the device. This was the RESET. The SET process was abrupt, while the RESET was gradual. As discussed in the previous chapter, the abrupt nature of the SET is indicative of an abrupt physical change in the active layer, such as the formation of an conductive filament. On the other hand, the gradual nature of RESET is probably occurring due to thermal phenomena, such as the disruption of the conductive filament.

Figure 5.5 (a), (b) and (c) depict the first three I-V characteristics obtained from typical and repeatable devices with Al:TiO_{2-x}, Nb:TiO_{2-x} and Nb:TiO_{2-x}/Al:TiO_{2-x} active layers, accordingly. All of the devices follow the same physics mechanism that was proposed above, as there are not major changes in the I-Vs direction and shape. In the case of the bilayer devices, the current just before the SET occurs, shows a slight saturation from 0.6 V to 1.2 V. This effect could be associated to a filament extension in the area where both Al and Nb cations exist. The precise reason of this behaviour is still unclear.

Figure 5.6 (a) presents the EF statistics calculated for 10 devices from each category. EF occured at -7.6 V for the Al:TiO_{2-x} devices and at -6.6 V for the Nb:TiO_{2-x} and bilayer devices. The EF voltage of the Nb:TiO_{2-x} devices, dropped by 1 V, however, the spread of the data was higher, with a standard deviation of ± 1 V. The bilayer devices were electroformed at -6.6 V with ± 0.5 V standard deviation which was the best EF performance among the three device stacks.

The statistics for the DC voltage sweeping is summarised in Figure 5.6 (b). The displayed mean and standard deviation of SET and RESET voltages, were collected from three repeatable and stable devices from each stack category. The SET voltage of Nb:TiO_{2-x} and Nb:TiO_{2-x}/Al:TiO_{2-x} devices was 1.5 V and 1.4 V, respectively, compared to 1.8 V for the Al:TiO_{2-x} devices. Additionally, the standard deviation was lower for the Nb:TiO_{2-x} and Nb:TiO_{2-x}/Al:TiO_{2-x} devices at ± 0.1 V, compared to ± 0.3 V of the

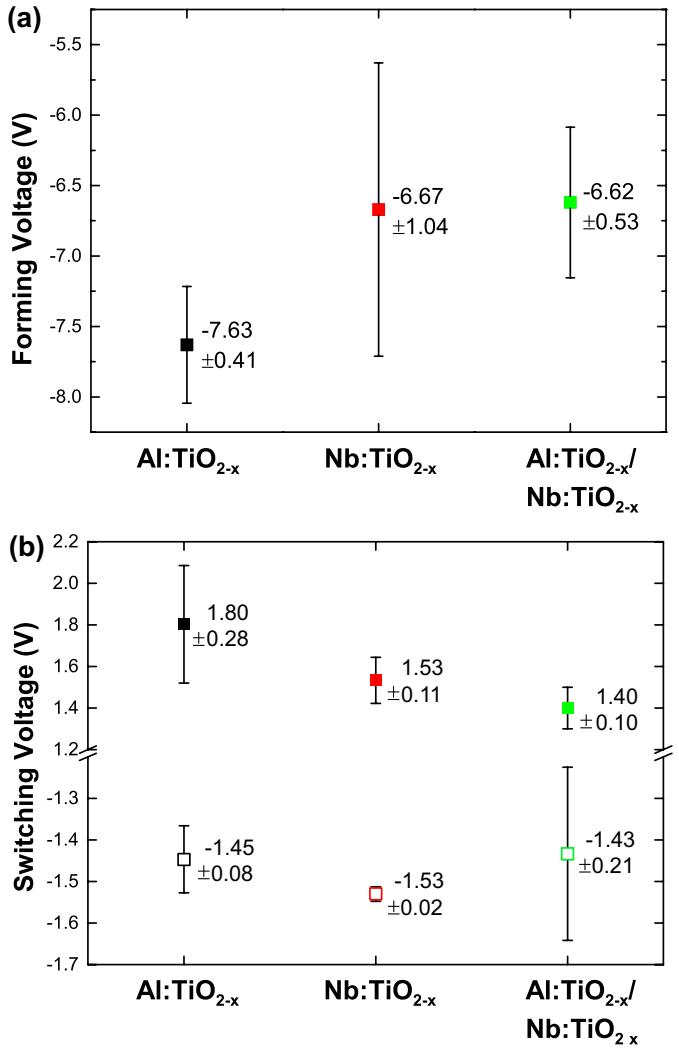

Figure 5.6: (a)Mean and standard deviation of DC electroforming voltages calculated for ten devices from each category and (b) mean and standard deviation of SET/RESET voltages calculated for three typical devices.

Al:TiO_{2-x} devices. The RESET voltage was very similar among the three categories, at -1.4 to -1.5 V. However, the standard deviation in the case of Nb:TiO_{2-x}/Al:TiO_{2-x} devices was much higher than the one in the case of Al:TiO_{2-x} and Nb:TiO_{2-x} devices. With a larger number of devices tested, the standard deviation could be more representative of the actual switching behaviour of the devices.

Interestingly, the Nb:TiO_{2-x} and Nb:TiO_{2-x}/Al:TiO_{2-x} showed a very similar performance in EF and DC voltage sweeping. More generally, the presence of foreign elements (at least at ±4 at. % concentration) did no cause major differences in the switching mechanism and performance. It is possible that after the filament formation which occurs with EF, the role of dopants is not significant and the SET and RESET operations are carried out with small modifications of the filaments at the interface of the oxide with the metal of the electrode. The Nb:TiO_{2-x}/Al:TiO_{2-x} has not induced any particular effect in EF or switching and it appears that the two layers behave in a homogeneous

manner.

5.7 Pulsed voltage characterisation of Al:TiO_{2-x}, Nb:TiO_{2-x} and bilayer devices

In addition to DC characterisation, pulsed voltage sweeping was carried out as an additional assessment of the resistance switching ability of the devices. The same testing system was used with the function that employs pulsed voltage schemes to toggle the devices' resistance between two distinct states. The devices were electroformed and tested for their switching performance using the algorithms presented in [112] and [111] accordingly. The same testing procedure using pulses was described in more detail in Chapter 4.

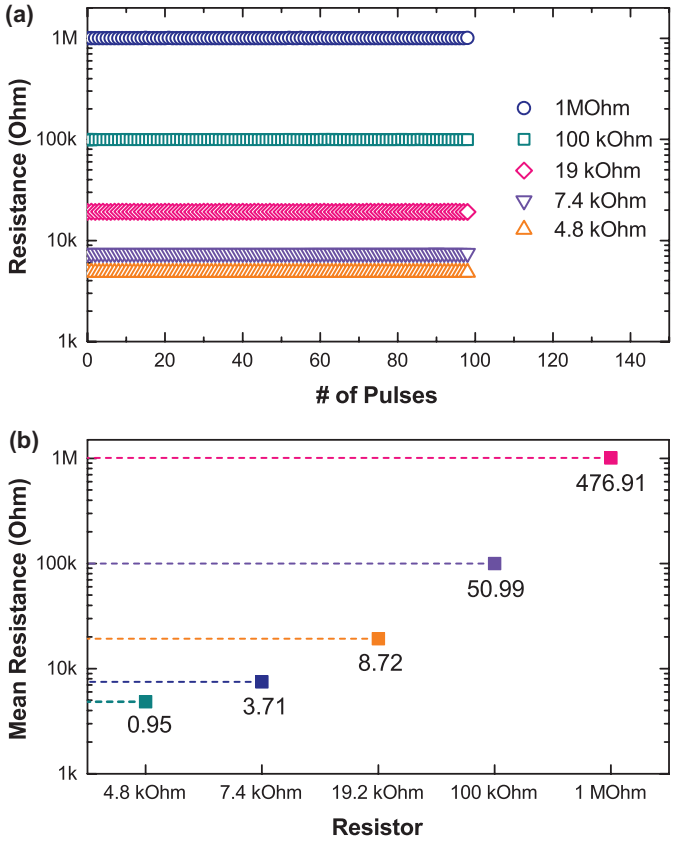

Figure 5.7: (a) 100 reads of five different resistors with 0.5 V pulses and (b) the resistance standard deviation extracted from resistance reads.

Before the devices' electrical characterisation, an assessment of the measuring system's precision in resistance measurement has been carried out. Five resistors were selected: 4.8 kOhm, 7.4 kOhm, 19 kOhm, 100 kOhm and 1 MOhm. The resistors were selected as such to cover the range of resistances that the current RRAM devices can obtain. Moreover, it was important to verify whether the system is capable of reading the devices'

Table 5.4: The settings used for pulsed electroforming and switching

Setting	Electroforming	Switching
Min. pulse amplitude (V)	0.5	0.2
Max. pulse amplitude (V)	10	0.1
Pulse amplitude step (V)	0.2	6
Pulse width (ms)	1	0.1
Polarity	+	-
Series resistance (kOhm)	100	-
Resistance threshold (%)	10	10
Interpulse time (ms)	1	1
Number of write pulses	10	10
Number of read pulses	5	5

resistance accurately, when the devices are at a high resistance regime as well as at a few kOhm regime. Each resistor was read 100 times and the data were analysed to calculate its mean and standard deviation. Figure 5.7 (a) depicts the raw data for each of the 5 resistors and (b) shows mean and standard deviation calculated for each of the resistors. It was observed that the higher the resistance, the more difficult it becomes to be read accurately. However, at high resistances like 1 MOhm, read standard deviation of ≈ 0.5 Ohm is not so significant. The settings that were used to electroform and switch the devices using pulses are shown in detail in Table 5.4.

Figure 5.8 (a) displays the EF results collected from 10 devices from each active layer category. The mean EF voltage was the same for Al:TiO_{2-x} and Nb:TiO_{2-x} devices at $\approx$ 7 V. The Al:TiO_{2-x}/Nb:TiO_{2-x} devices exhibited a lower mean EF voltage of 6.12 V, at the expense of slightly higher standard deviation of $\pm$1 V compared to $\pm$0.8 V and $\pm$0.6 V for the Al:TiO_{2-x} and Nb:TiO_{2-x} devices, respectively. The bilayers had the lowest EF voltages among all three device types, confirming the result from the DC EF. Figure 5.8 (b), portrays the mean and standard deviation of switching voltages collected from 5 repeatable devices from each active layer configuration. Among the three types of devices, Al:TiO_{2-x}-based devices had the worst performance in terms of mean switching voltage with $\pm$1.6 V and $\pm$0.7-0.8 V standard deviation of voltages. Nb:TiO_{2-x}-based devices on average switched with +1.6 V/-1.4 V and had lower standard deviation of $\pm$0.4 and $\pm$0.5 V, respectively. The bilayer devices exhibited had the best performance among the three types with switching voltages +1.4 V/-1.2 V and same standard deviation as the Nb:TiO_{2-x}-based devices. Overall, EF and switching voltage performance seemed to favour the bilayer devices, which however did not show any differences in the switching mechanism and behaved as a single continuous active layer.

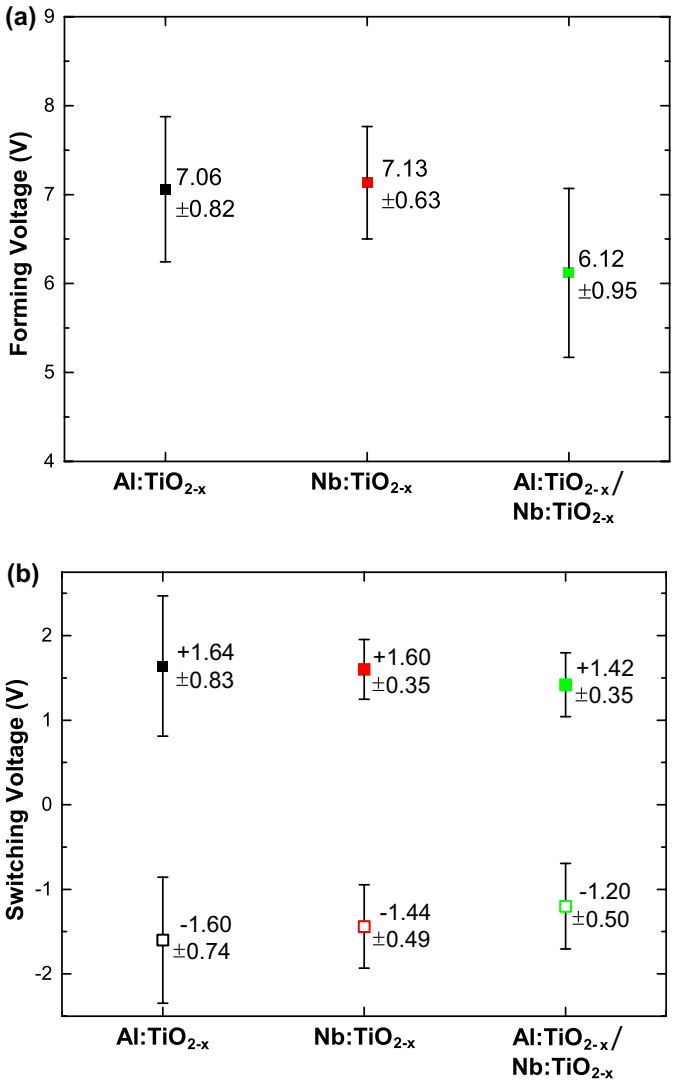

Figure 5.8: (a) Pulsed voltage EF mean and standard deviation calculated for 10 devices from each type and (b) mean and standard deviation of switching voltages using pulses from 5 devices from each type.

5.8 Retention of Al:TiO_{2-x}, Nb:TiO_{2-x} and bilayer devices

Reliable devices from all three active layers, were tested for their retention performance. For each active layer one device was selected and after it was driven to a specific resistance state it was tested for 9 hours by reading it's resistance every 15 minutes at room temperature. The selected devices, were previously electroformed and tested with pulsed sweeping, confirming a repeatable switching performance between two resistance states, over a long period of time. The selected resistance states were: 10 kOhm, 50 kOhm and 100 kOhm. The purpose of this test was to show, if the devices can preserve their state with time. These resistance states were selected in purpose, as it has been observed before that the higher the resistance is the more difficult it is for the devices

to maintain it. Additionally, the capacity of a device to maintain a state is an indicator of robustness and reliable performance.

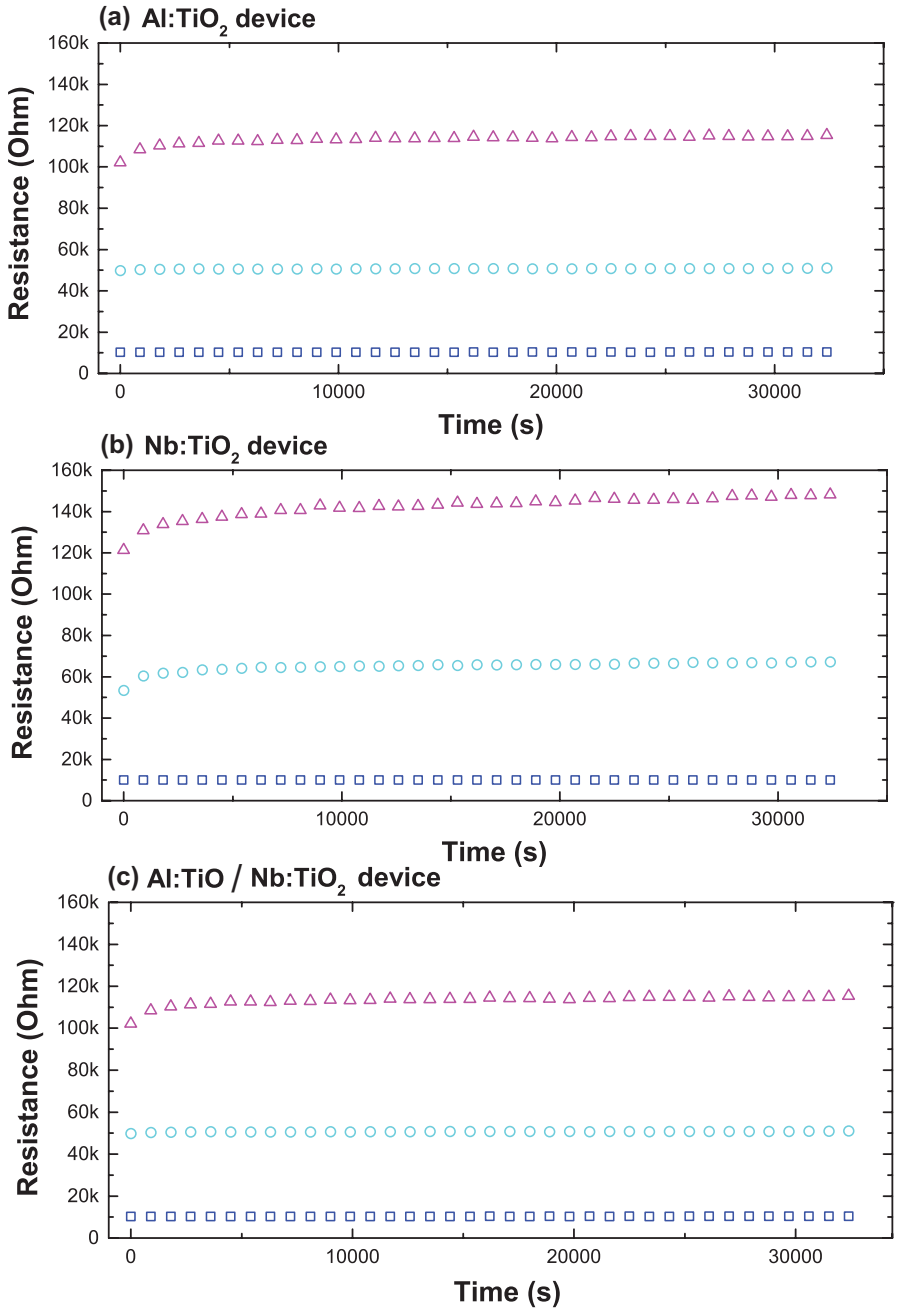

Figure 5.9: Retention results in room temperature for three different states from a typical and well-behaved device from (a) a Al:TiO_{2-x}, (b) a Nb:TiO_{2-x} and (c) a Al:TiO_{2-x}/Nb:TiO_{2-x} device.

Figure 5.9 (a), (b) and (c) portray the raw resistance reads for the three different states for the Al:TiO_{2-x}, Nb:TiO_{2-x} and Al:TiO_{2-x}/Nb:TiO_{2-x} devices, respectively. In all 3 devices the 100 Ohm state appeared to have drifted immediately after the first read. This resistance state eventually saturated at about 110-120 kOhm, with the Nb:TiO_{2-x} device being the only exception. Unfortunately, this device started from a state of 120

kOhm, 20 kOhm higher than the other two. After several trial tests, it became clear that at resistance states above 100 kOhm, it becomes very difficult to control the resistance of the device. This implied, that feeding devices of this resistance state with short pulses of 1.5-3 V, yielded in very abrupt resistance changes. These changes often led the devices to the GOhm range, making them more fragile.

In other cases, these instabilities dropped the devices' resistance to the irreversible regime <3 kOhm, where it was impossible to restore them to the useful and repeatable resistance range. In all 3 devices, the 10 and 50 kOhm were the most stable states, with only exception the Nb:TiO_{2-x} device, which experienced an abrupt 10 kOhm drift from the first resistance read. The stability of the two lower states, could be associated with thicker and more robust conductive filaments. These resistance states could be fine-tuned very easily, by sending appropriate pulses. Short pulses of 1.5-2 V amplitude that gradually increased in duration, was an effective pulsing scheme, to gradually modify the device's resistance with small steps. The resistance could be increased or decreased by appropriately applying pulses of positive or negative polarity.

The 100 kOhm resistance state possibly occurred due to the formation of thinner and more fragile filaments. Minor modifications on these fragile filaments could result in very dramatic changes of the device's resistance and fine-tuning of the resistance was almost impossible. It is possible that the gradual resistance drift that is observed in figure 5.9, is a slow physical change in the active layer that takes place anyway and it is not caused by the reading pulses. It could be possibly described as a natural decomposition of the filament that takes place over time. An experiment which would involve more frequent reading intervals could prove the latter argument.

The retention measurements are summarised in table 5.5. The mean, standard deviation and relative standard deviation are quoted for each device stack and resistance state. The deviation of resistance among different reads was associated with the level of resistance.

Table 5.5: Retention measurements on 3 different states for the Al:TiO_{2-x}, Nb:TiO_{2-x} and bilayer devices.

Resistance state		**Al:TiO_{2-x}**	**Nb:TiO_{2-x}**	**Al:TiO_{2-x} /Nb:TiO_{2-x}**
10 kOhm	**Mean**	10133	9984	10323
	SD	32	4	32
	RSD (%)	0.32	0.04	0.31
50 kOhm	**Mean**	54530	65110	50666
	SD	909	2516	200
	RSD (%)	1.67	3.86	0.39
100 kOhm	**Mean**	118879	142446	113401
	SD	2705	5484	2382
	RSD (%)	2.28	3.85	2.10

The relative standard deviation (%), reflected this and showed that at higher resistance levels, the variability the resistance that was read was higher.

5.9 Summary

In this chapter, it was demonstrated that Nb can be successfully introduced as a 5+ dopant in TiO_{2-x} thin films. Nb (n-type in TiO_{2-x}) was selected among others for its valency and ionic size, to complement previously developed Al:TiO_{2-x} (p-type) thin films in bilayer RRAM devices. The Nb % at. content of the TiO_{2-x} thin films was verified by XPS. The fabricated bilayer devices showed an abrupt EF followed by typical hysteretic I-V signatures, like their Al- and Nb-doped counterparts. The bilayer RRAM devices were fabricated to investigate the existence of a diode behaviour at the p-n junction formed at the interface of the Al- and Nb-doped thin films, however, this behaviour was not confirmed experimentally.

Al device configurations were tested to for their switching performance using both DC and pulsed voltage sweeping. Devices containing Nb, were electroformed on average with -6.6 V, compared to the Al-doped equivalent devices at -7.6 V. The mean SET voltage of Nb:TiO_{2-x} and bilayer devices dropped at 1.5 and 1.4 V, respectively, compared to 1.8 V for the Al-doped devices. From the pulsed voltage sweeping tests, the bilayer devices showed the lowest electroforming voltages with 6.1 V, compared to 7.0 V of the Al- and Nb-doped devices, however, at the expense of higher distribution of electroforming voltages. In terms of resistance switching using pulsed voltage ramps, the bilayer devices showed the most promising performance with switching voltages +1.4 V/-1.2 V. The Al- and Nb-doped devices followed with +1.6 V/-1.6 V and +1.6 V/-1.4 V, respectively.

Preliminary retention tests showed that all three device configurations were able to maintain their resistance state (10, 50 and 100 kOhm) at room temperature. The standard deviation of the resistance reads increased with increasing resistance, but the relative standard deviation showed that the bilayer devices were more robust in maintaining the resistance state, compared to the other two device configurations.

Chapter 6

Conclusion and Future Work

6.1 Contributions

Throughout this PhD programme, a number of Ti-based resistive random access memory (ReRAM) devices were fabricated. The chemical composition of the transition-metal-oxides that formed the ReRAM active layers, as well as the switching performance and the operation physics of these devices have been studied.

In Chapter 2, an overview of the materials that have been employed as active layers in ReRAM the past years, has been provided, giving emphasis to the ones that yielded the best device performance. Special focus has been put on TiO_{2-x} ReRAM, as it was the model oxide in this thesis, mostly for its known variety of oxygen-deficient phases, a key characteristic for ReRAM applications where ionic motion plays a crucial role in the device's switching dynamics. Additionally, an overview of the foreign elements used as dopants in TiO_{2-x} ReRAM for engineering the resistance switching dynamics, has been provided.

In Chapter 3, Al-doped TiO_{2-x} thin films with 4% at. Al were developed and inserted in ReRAM devices. Doping with Al improved the devices' performance by decreasing the electroforming and switching thresholds. In particular, Al:TiO_x-based devices were electroformed on average at -5.7 V compared to -6.4 V for their undoped counterparts. Both doped and undoped devices could support both analog and binary switching, subject to the pulsing scheme, in a repeatable manner for a large number of cycles. The required electroforming step, corroborated the filamentary switching theory. The analog mode of switching could be assigned to small modifications of the conductive filaments. The valence difference between the Al and Ti ions could be the key for the reduction of the oxygen vacancy formation energy, therefore lowering the EF and switching voltages.

In Chapter 4, multilayer thin films comprising Al_2O_{3-x} ultra-thin layers inserted between TiO_{2-x} thin films, were fabricated and characterised. The multilayer stacks were inserted in ReRAM devices and tested for their resistive switching performance, as an alternative approach to doping with Al. All device stacks, including the ones without Al_2O_{3-x}, electroformed and switched in a similar fashion, as dictated by the filamentary mechanism. The number of the incorporated Al_2O_{3-x} thin films, was found to affect the switching parameters of the devices, but not the mechanism. The mean electroforming voltage of devices containing 1, 2, and 3 Al_2O_{3-x} layers, was slightly increased due to the high resistivity of the Al_2O_{3-x}, at -5.2 V, -5.4 V and -5.3 V, respectively, compared to -5.0 V of the purely TiO_{2-x} based devices. However, the mean switching voltage thresholds and their variability dropped for the devices with 1 and 2 Al_2O_{3-x} layers, to +2.3 V/-1.5 V and +2.2 V/-1.7 V, from +2.5 V/-2.0 V for the the purely TiO_{2-x} based devices. Analog switching using appropriate pulsed voltage ramps was feasible, and showed that devices containing Al_2O_{3-x} layers were able to switch with pulsing schemes as low as +1.0 V/-1.0 V. Finally, preliminary endurance tests were carried out to confirm the robustness of the fabricated devices.

In Chapter 5, bilayer ReRAM devices comprising Al- and Nb-doped TiO_{2-x} thin films were fabricated and characterised. With Al and Nb being p-type and n-type dopants in TiO_{2-x}, respectively, the possibility of a diode behaviour at the p-n interface between the two layers was studied. The diode behaviour was not confirmed when the bilayer devices were tested with DC voltage sweeping.The carrier type in the doped thin films was not identified either, due to the limited measurement capability of the Van der Pau tool.

Apart from the bilayer devices, single doped devices with Al and Nb of equal % at. concentrations and sam active layer thickness were fabricated ad tested. Nb-doped and bilayer devices, were electroformed on average with -6.6 V, compared to the Al-doped equivalent devices at -7.6 V. The same device configurations exhibited a reduced mean SET voltage of 1.5 V and 1.4 V, respectively, compared to 1.8 V of the Al-doped devices. Tested with pulsed voltage sweeping, the bilayer devices showed the lowest electroforming voltages with 6.1 V, compared to 7.0 V of the Al- and Nb-doped devices, however, at the expense of higher distribution of electroforming voltages. In terms of resistance switching using pulsed voltage ramps, the bilayer devices showed the most promising performance with switching voltages +1.4 V/-1.2 V, against +1.6 V/-1.6 V and +1.6 V/-1.4 V of the Al- and Nb-doped devices, respectively. In preliminary retention tests, all three device configurations were able to sustain their resistance states (10, 50 and 100 kOhm) at room temperature for at least 9 hours. The standard deviation of the resistance reads increased with increasing resistance, but the relative standard deviation showed that the bilayer devices were more robust in maintaining the resistance state, compared to the other two device configurations.

6.2 Future work

This thesis was focused on amorphous TiO_{2-x} as it can be easily deposited with reactive sputtering at room temperature and it can be form a large number of oxygen deficient phases, ideal for ReRAM applications, where redox reactions play a key role in the device's operation. The ease of reduction, which is often spontaneous in TiO_{2-x}, is a material characteristic that can be associated to low switching voltages and generally low power operation. Crystalline TiO_{2-x} thin films could be undesirable for many ReRAM applications for several reasons. For example, the higher surface roughness of a crystalline TiO_{2-x} thin film would not be ideal for use in devices with small area, requiring very low active layer thickness. Furthermore, the crystallisation in TiO_{2-x} begins at about 600 °C which would make the processing of such devices CMOS incompatible. However, working with a crystalline TiO_{2-x} ReRAM, could allow for studying active layer with characterisation techniques that give a good resolution with crystalline materials, such as RAMAN spectroscopy and *in-situ* switching high-resolution scanning electron microscopy (SEM) and X-ray diffraction (XRD).

Possible ideas for continuing this work would be to investigate alternative ways to deposit crystalline TiO_2 thin films, doped with Al and Nb with substitutional doping. Atomic layer deposition can reach the crystallisation temperature required for Anatase or Rutile TiO_2. However, challenges such as the decomposition of the Ti precursors at high temperatures, often caused problems [130]. Only some reports involving halide precursors led to successful fabrication of Rutile, while all other reports usually mentioned amorphous or Anatase thin films. A promising plan would be to use ALD or CVD to deposit TiO_{2-x} on Ruthenium substrates. Ruthenium is a noble metal like Pt and therefore it could be an alternative electrode metal. The interesting fact about Ruthenium is that it forms RuO_{2-x} which adopts a Rutile phase. Using Ruthenium, oxidised as a Rutile-friendly substrate, Rutile TiO_{2-x} could be deposited with ALD at temperatures as low as 250 °C [131].

Following a successful crystalline TiO_{2-x} deposition, alternative ways of doping with foreign elements should be found. Ideally, Al and Nb should do substitutional doping to ensure the formation of p- and n- type conductivity. The real challenge would be to create the bilayer structure, something that was trivial with reactive sputtering. These are the main challenges that should be tackled, to realise ReRAM devices with diode behaviour. Although p- and n- conductivity in ReRAM is very challenging for all the reasons that were mentioned previously, such a contribution would be a fantastic breakthrough towards reconfigurable active electronics.

References

[1] B. Bhowmik, K. Dutta, a. Hazra, and P. Bhattacharyya, "Low temperature acetone detection by p-type nano-titania thin film: Equivalent circuit model and sensing mechanism," *Solid-State Electronics*, vol. 99, pp. 84–92, Sept. 2014.

[2] F. Bayata, B. Saruhan-Brings, and M. Ürgen, "Hydrogen gas sensing properties of nanoporous Al-doped titania," *Sensors and Actuators B: Chemical*, vol. 204, pp. 109–118, Dec. 2014.

[3] M. Kumar, L. Tan, N. Gosvami, and H. Gao, "Titania Nanofilm with Electrical Switching Effects upon Hydrogen/Air Exposure at Room Temperature," *The Journal of Physical Chemistry C*, vol. 113, pp. 6381–6389, Apr. 2009.

[4] N. G. Park, J. van de Lagemaat, and A. J. Frank, "Comparison of Dye-Sensitized Rutile-and Anatase-Based TiO_2 Solar Cells," *The Journal of Physical Chemistry B*, vol. 104, pp. 8989–8994, 2000.

[5] R. S. Mane, W. J. Lee, H. M. Pathan, and S.-H. Han, "Nanocrystalline TiO_2/ZnO Thin Films: Fabrication and Application to Dye-Sensitized Solar Cells," *Journal of Physical Chemistry B*, vol. 109, pp. 24254–24259, 2005.

[6] M. Zukalova, Z. Arnost, K. Ladislav, M. K. Nazeeruddin, P. Liska, and M. Gratzel, "Organized Mesoporous TiO_2 Films Exhibiting Greatly Enhanced Performance in Dye-Sensitized Solar Cells," *Nano Letters*, vol. 5, no. 9, pp. 1789–1792, 2005.

[7] Q. Yuan, Z. Wu, Y. Jin, F. Xiong, and W. Huang, "Surface Chemistry of Formaldehyde on Rutile TiO_2 (110) Surface: Photocatalysis vs Thermal-Catalysis," *Journal of Physical Chemistry C*, vol. 35, no. 118, pp. 20420–20428, 2014.

[8] K. Szot, M. Rogala, W. Speier, Z. Klusek, A. Besmehn, and R. Waser, "TiO_2-a prototypical memristive material.," *Nanotechnology*, vol. 22, p. 254001, June 2011.

[9] A. Sawa, "Resistive switching in transition metal oxides," *Materials Today*, vol. 11, no. 6, pp. 28–36, 2008.

[10] D. Acharyya, A. Hazra, and P. Bhattacharyya, "A journey towards reliability improvement of TiO_2 based Resistive Random Access Memory: A review," *Microelectronics Reliability*, vol. 54, pp. 541–560, Mar. 2014.

[11] D. Carta, A. P. Hitchcock, P. Guttmann, A. Regoutz, A. Khiat, A. Serb, I. Gupta, and T. Prodromakis, "Spatially resolved TiOx phases in switched RRAM devices using soft X-ray spectromicroscopy," *Scientific Reports*, vol. 6, p. 21525, feb 2016.

[12] D.-H. Kwon, K. M. Kim, J. H. Jang, J. M. Jeon, M. Lee, G. H. Kim, X.-S. Li, G.-S. Park, B. Lee, S. Han, M. Kim, and C. S. Hwang, "Atomic structure of conducting nanofilaments in TiO_2 resistive switching memory," *Nature Nanotechnology*, vol. 5, pp. 148–153, Jan. 2010.

[13] M. Arita, A. Takahashi, Y. Ohno, A. Nakane, A. Tsurumaki-Fukuchi, and Y. Takahashi, "Switching operation and degradation of resistive random access memory composed of tungsten oxide and copper investigated using in-situ TEM," *Scientific ReportsSSSSS*, vol. 5, p. 17103, Nov. 2015.

[14] H. Schroeder, R. Pandian, and J. Miao, "Resistive switching and changes in microstructure," *Physica Status Solidi (A)*, vol. 208, pp. 300–316, Feb. 2011.

[15] K. Szot, W. Speier, G. Bihlmayer, and R. Waser, "Switching the electrical resistance of individual dislocations in single-crystalline $SrTiO_3$," *Nature Materials*, vol. 5, pp. 312–320, Mar. 2006.

[16] S. Yu, X. Guan, and H. Wong, "On the Stochastic Nature of Resistive Switching in Metal Oxide RRAM: Physical Modeling, Monte Carlo Simulation, and Experimental Characterization," *Electron Devices Meeting (IEDM), 2011 IEEE International*, pp. 17.3.1–17.3.4, Sept. 2011.

[17] M. A. Alam, B. Weir, J. Bude, P. Silverman, and D. Monroe, "Explanation of Soft and Hard Breakdown and its Consequences for Area Scaling," *IEDM Tech Dig*, pp. 449–452, 1999.

[18] Q. Liu, J. Sun, H. Lv, S. Long, K. Yin, N. Wan, Y. Li, L. Sun, and M. Liu, "Real–time observation on dynamic growth/dissolution of conductive filaments in oxide–electrolyte–based reram," *Advanced Materials*, vol. 24, no. 14, pp. 1844–1849, 2012.

[19] J. J. Yang, F. Miao, M. D. Pickett, D. A. A. Ohlberg, D. R. Stewart, C. N. Lau, and R. S. Williams, "The mechanism of electroforming of metal oxide memristive switches," *Nanoscale Research Letters*, vol. 20, pp. 215201–215209, May 2009.

[20] M. A. Alam, S. Member, B. E. Weir, and P. J. Silverman, "A Study of Soft and Hard Breakdown Part I : Analysis of Statistical Percolation Conductance," *IEEE Transactions on Electron Devices*, vol. 49, no. 2, pp. 232–238, 2002.

[21] M. A. Alam, S. Member, B. E. Weir, and P. J. Silverman, "A Study of Soft and Hard Breakdown Part II : Principles of Area , Thickness , and Voltage Scaling," *IEEE Transactions on Electron Devices*, vol. 49, no. 2, pp. 239–246, 2002.

[22] M. Trapatseli, D. Carta, A. Regoutz, A. Khiat, A. Serb, I. Gupta, and T. Prodromakis, "Conductive Atomic Force Microscopy Investigation of Switching Thresholds in Titanium Dioxide Thin Films," *The Journal of Physical Chemistry C*, vol. 119, no. 21, pp. 11958–11964, 2015.

[23] L. Chua, "Memristor - The Missing Circuit Element," *IEEE Transactions on Circuit Theory*, vol. CT-18, pp. 507–519, Sept. 1971.

[24] A. Beck, J. G. Bednorz, C. Gerber, C. Rossel, and D. Widmer, "Reproducible switching effect in thin oxide films for memory applications," *Applied Physics Letters*, vol. 77, p. 139, Jan. 2000.

[25] W. Zhuang, W. Pan, B. Ulrich, J. Lee, L. Stecker, A. Burmaster, D. Evans, S. Hsu, M. Tajiri, A. Shimaoka, K. Inoue, N. Awaya, T. Naka, K. Sakiyama, Y. Wang, S. Liu, N. Wu, and A. Ignatiev, "Novell colossal magnetoresistive thin film nonvolatile resistance random access memory (RRAM)," *Electron Devices Meeting, 2002. IEDM '02. Digest. International*, pp. 1–4, Apr. 2002.

[26] J. G. Baek, S. Seo, M. J. Lee, D. H. Seo, D. S. Suh, J. C. Park, S. . Park, H. S. Kim, and M. S. Lee, "Highly Scalable Non-volatile Resistive Memory using Simple Binary Oxide Driven by Asymmetric Unipolar Voltage Pulses," *Electron Devices Meeting, 2004. IEDM Technical Digest. IEEE International*, pp. 23.6.1–23.6.4, Sept. 2004.

[27] D. B. Strukov, G. S. Snider, D. R. Stewart, and R. S. Williams, "The missing memristor found," *Nature*, vol. 453, pp. 80–83, May 2008.

[28] H. S. P. Wong, H.-Y. Lee, S. Yu, Y.-S. Chen, Y. Wu, P.-S. Chen, B. Lee, F. T. Chen, and M.-J. Tsai, "Metal-Oxide RRAM," *Proceedings of the IEEE*, vol. 100, pp. 1951–1970, June 2012.

[29] R. Waser and M. Aono, "Nanoionics-based resistive switching memories," *Nature Materials*, vol. 6, pp. 833–840, Nov. 2007.

[30] Y. Li, S. Long, Q. Liu, H. Lü, S. Liu, and M. Liu, "An overview of resistive random access memory devices," *Chinese Science Bulletin*, vol. 56, pp. 3072–3078, Oct. 2011.

[31] R. Waser, R. Dittmann, G. Staikov, and K. Szot, "Redox-Based Resistive Switching Memories - Nanoionic Mechanisms, Prospects, and Challenges," *Advanced Materials*, vol. 21, pp. 2632–2663, July 2009.

[32] J. J. Yang, D. B. Strukov, and D. R. Stewart, "Memristive devices for computing," *Nature Nanotechnology*, vol. 8, pp. 13–24, Dec. 2012.

[33] M.-J. Lee, C. B. Lee, D. Lee, S. R. Lee, M. Chang, J. H. Hur, Y.-B. Kim, C.-J. Kim, D. H. Seo, S. Seo, U.-I. Chung, I.-K. Yoo, and K. Kim, "A fast, high-endurance and scalable non-volatile memory device made from asymmetric Ta_2O_{5-x}/TaO_{2x} bilayer structures," *Nature Materials*, vol. 10, pp. 625–630, July 2011.

[34] J. J. Yang, "High switching endurance in TaO_x memristive devices," *Applied Physics Letters*, vol. 97, pp. 232102–232105, Mar. 2010.

[35] Z. Wei, Y. Kanzawa, K. Arita, K. Katoh, K. Kawai, S. Muraoka, S. Mitani, S. Fujii, K. Katayama, M. Iijima, T. Mikawa, T.Ninomiya, R. Miyanaga, Y. Kawashima, K. Stuji, A. Himeno, T. Okada, R. Azuma, K. Shimakawa, H. Sugaya, T. Takagi, R. Yasuhara, K. Horiba, H. Kumigashira, and M. Oshima, "Highly reliable TaO_x reram and direct evidence of redox reaction mechanism," *Electron Devices Meeting, 2008. IEDM 2008. IEEE International*, pp. 1–4, Sept. 2008.

[36] J. E. Stevens, A. J. Lohn, S. A. Decker, B. L. Doyle, P. R. Mickel, and M. J. Marinella, "Reactive sputtering of substoichiometric Ta_2O_x for resistive memory applications," *Journal of Vacuum Science {&} Technology A: Vacuum, Surfaces, and Films*, vol. 32, p. 21501, Jan. 2014.

[37] E.-K. Lai, W.-C. Chien, Y.-C. Chen, T.-J. Hong, Y.-Y. Lin, K.-P. Chang, Y.-D. Yao, P. Lin, S.-F. Horng, J. Gong, S.-C. Tsai, C.-H. Lee, S.-H. Hsieh, C.-F. Chen, Y.-H. Shih, K.-Y. Hsieh, R. Liu, and C.-Y. Lu, "Tungsten Oxide Resistive Memory Using Rapid Thermal Oxidation of Tungsten Plugs," *Japanese Journal of Applied Physics*, vol. 49, p. 04DD17, Apr. 2010.

[38] S. Kim, K. P. Biju, M. Jo, S. Jung, J. Park, J. Lee, W. Lee, J. Shin, S. Park, and H. Hwang, "Effect of scaling WO_x based rrams on their resistive switching characteristics," *IEEE Electron Device Letters*, vol. 32, pp. 671–673, May 2011.

[39] Q. Zhou and J. Zhai, "HfO_x bipolar resistive memory with robust endurance using ZrN_x as buttom electrode," *Applied Surface Science*, vol. 284, pp. 644–650, Nov. 2013.

[40] C.-H. Cheng and A. Chin, "Evaluation of Temperature Stability of Trilayer Resistive Memories Using Work-Function Tuning," *Applied Physics Express*, vol. 6, p. 41203, Apr. 2013.

[41] W. Chien, Y. Chen, E. Lai, Y. Yao, P. Lin, S. Horng, J. Gong, T. Chou, H. Lin, M. Chang, Y. Shih, K. Hsieh, R. Liu, and C.-Y. Lu, "Unipolar switching behaviors of rto WO_x rram," *IEEE Electron Device Letters*, vol. 21, pp. 126–128, Jan. 2010.

[42] H. Y. Lee, Y. S. Chen, P. S. Chen, T. Y. Wu, F. Chen, C. C. Wang, P. J. Tzeng, M. J. Tsai, and C. Lien, "Low-Power and Nanosecond Switching in Robust Hafnium Oxide Resistive Memory With a Thin Ti Cap," *IEEE Electron Device Letters*, vol. 31, pp. 44–46, Jan. 2010.

[43] M. D. Pickett and R. S. Williams, "Sub-100 fJ and sub-nanosecond thermally driven threshold switching in niobium oxide crosspoint nanodevices," *Nanotechnology*, vol. 23, p. 215202 (9pp), May 2012.

[44] F. Zhang, X. Li, B. Gao, B. Chen, P. Huang, Y. Fu, Y. Chen, L. Liu, J. Kang, N. Singh, L. Guo-Qiang, and D.-L. Kwong, "Complementary Metal Oxide Semiconductor Compatible Hf-Based Resistive Random Access Memory with Ultralow Switching Current/Power," *Japanese Journal of Applied Physics*, vol. 51, p. 04DD08, Apr. 2012.

[45] L. Zhong, P. a. Reed, R. Huang, C. H. De Groot, and L. Jiang, "Amorphous SiC based non-volatile resistive memories with ultrahigh ON/OFF ratios," *Microelectronic Engineering*, vol. 119, pp. 61–64, 2014.

[46] Y.-T. Wu, S. Jou, and P.-J. Yang, "Resistance switching of thin AlO_x and cu-doped-AlO_x films," *Thin Solid Films*, vol. 544, pp. 24–27, Oct. 2013.

[47] A. C. Torrezan, J. P. Strachan, G. Medeiros-Ribeiro, and R. S. Williams, "Sub-nanosecond switching of a tantalum oxide memristor," *Nanotechnology*, vol. 22, no. 48, p. 485203, 2011.

[48] R. Huang, L. Zhang, D. Gao, Y. Pan, S. Qin, P. Tang, Y. Cai, and Y. Wang, "Resistive switching of silicon-rich-oxide featuring high compatibility with CMOS technology for 3D stackable and embedded applications," *Applied Physics A*, vol. 102, pp. 927–931, Mar. 2011.

[49] C. Hermes, R. Bruchhaus, and R. Waser, "Forming-Free TiO_2-Based Resistive Switching Devices on CMOS-Compatible W-Plugs," *IEEE Electron Device Letters*, vol. 32, pp. 1588–1590, Nov. 2011.

[50] A. Templeton, X. Wang, S. J. Penn, S. J. Webb, L. F. Cohen, and N. M. Alford, "Microwave Dielectric Loss of Titanium Oxide," *Journal of American Ceramic Society*, vol. 83, pp. 95–100, Jan. 2000.

[51] J. Choi, H. Park, and M. Hoffmann, "Combinatorial doping of TiO_2 with Platinum (Pt), Chromium (Cr), Vanadium (V), and Nickel (Ni) to achieve enhanced photocatalytic activity with visible light irradiation," *Journal of Materials Research*, vol. 25, pp. 149–158, Jan. 2010.

[52] J. Carneiro, V. Teixeira, A. Portinha, L. Dupák, A. Magalhães, and P. Coutinho, "Study of the deposition parameters and Fe-dopant effect in the photocatalytic

activity of TiO_2 films prepared by dc reactive magnetron sputtering," *Vacuum*, vol. 78, pp. 37–46, Apr. 2005.

[53] W. Zhang, S. Zhu, Y. Li, and F. Wang, "Photocatalytic Zn-doped TiO_2 films prepared by DC reactive magnetron sputtering," *Vacuum*, vol. 82, pp. 328–335, Nov. 2007.

[54] K.-C. Chang, R. Zhang, T.-C. Chang, T.-M. Tsai, J. C. Lou, J.-H. Chen, T.-F. Young, M.-C. Chen, Y.-L. Yang, Y.-C. Pan, G.-W. Chang, T.-J. Chu, C.-C. Shih, J.-Y. Chen, C.-H. Pan, Y.-T. Su, Y.-E. Syu, Y.-H. Tai, and S. M. Sze, "Origin of Hopping Conduction in Graphene-Oxide-Doped Silicon Oxide Resistance Random Access Memory Devices," *IEEE Electron Device Letters*, vol. 34, pp. 677–679, May 2013.

[55] G. Congedo, C. Wiemer, A. Lamperti, E. Cianci, Aless, ro Molle, F. G. Volpe, S. Spiga, and A. Molle, "Atomic layer-deposited al-HfO_2/SiO_2 bi-layers towards 3d charge trapping non-volatile memory," *Thin Solid Films*, vol. 533, pp. 9–14, Apr. 2013.

[56] I.-C. Yao, D.-Y. Lee, T.-Y. Tseng, and P. Lin, "Fabrication and resistive switching characteristics of high compact Ga-doped ZnO nanorod thin film devices," *Nanotechnology*, vol. 23, p. 145201 (8pp), Mar. 2012.

[57] S. Chae, J. Lee, S. Kim, S. Lee, S. Chang, C. Liu, B. Kahng, H. Shin, D.-W. Kim, C. Jung, S. Seo, M.-J. Lee, and T. Noh, "Random Circuit Breaker Network Model for Unipolar Resistance Switching," *Advanced Materials*, vol. 20, pp. 1154–1159, Mar. 2008.

[58] H. Zhang, Bin Gao, B. Sun, G. Chen, L. Zeng, L. Liu, X. Liu, J. Lu, R. Han, J. Kang, and Bin Yu, "Ionic doping effect in ZrO_2 resistive switching memory," *Applied Physics Letters*, vol. 96, pp. 1–3, Jan. 2010.

[59] B. M. Long, S. Mandal, J. Livecchi, and R. Jha, "Effects of mg-doping on HfO_2-based reram device switching characteristics," *IEEE Electron Device Letters*, vol. 34, pp. 1247–1249, Oct. 2013.

[60] R. W. Mott, N. F., Gurney, *Electronic Processes in Ionic Crystals*. New York: Dover Publications, Inc., 2nd ed., 1964.

[61] W. D. J. Callister, *Material Science and Engineering: An Introduction*. John Wiley & Sons, Inc., 7th ed., 2007.

[62] J.-Y. Lin and B.-X. Wang, "Room-temperature voltage stressing effects on resistive switching of conductive-bridging ram cells with cu-doped SiO_2 films," *Advances in Materials Science and Engineering*, vol. 2014, pp. 1–7, Jan. 2014.

[63] H. Li, Q. Chen, X. Chen, Q. Mao, J. Xi, and Z. Ji, "Improvement of resistive switching in ZnO film by Ti doping," *Thin Solid Films*, vol. 537, pp. 279–284, June 2013.

[64] T.-M. Tsai, K.-C. Chang, T.-C. Chang, G.-W. Chang, Y.-E. Syu, Y.-T. Su, G.-R. Liu, K.-H. Liao, M.-C. Chen, H.-C. Huang, Y.-H. Tai, D.-S. Gan, C. Ye, H. Wang, and S. M. Sze, "Origin of hopping conduction in sn-doped silicon oxide rram with supercritical CO_2 fluid treatment," *IEEE Electron Device Letters*, vol. 33, pp. 1693–1695, Dec. 2012.

[65] K.-C. Chang, C.-H. Pan, T.-C. Chang, T.-M. Tsai, R. Zhang, J.-C. Lou, T.-F. Young, J.-H. Chen, C.-C. Shih, T.-J. Chu, J.-Y. Chen, Y.-T. Su, J.-P. Jiang, K.-H. Chen, H.-C. Huang, Y.-E. Syu, D.-S. Gan, and S. M. Sze, "Hopping effect of hydrogen-doped silicon oxide insert rram by supercritical CO_2 fluid treatment," *IEEE Electron Device Letters*, vol. 34, pp. 617–619, May 2013.

[66] L. Lamagna, A. Molle, C. Wiemer, S. Spiga, C. Grazianetti, G. Congedo, and M. Fanciulli, "Atomic layer deposition of al-doped ZrO_2 thin films as gatedielectric for $In_{0.53}Ga_{0.47}As$," *Journal of Electrochemical Society*, vol. 159, pp. 220–224, June 2012.

[67] S. Spiga, R. Rao, L. Lamagna, C. Wiemer, G. Congedo, A. Lamperti, A. Molle, M. Fanciulli, F. Palma, and F. Irrera, "Structural and electrical properties of atomic layer deposited al-doped ZrO_2 films and of the interface with tan electrode," *Journal of Applied Physics*, vol. 112, p. 14107, Jan. 2012.

[68] A. Younis, D. Chu, and S. Li, "Bi-stable resistive switching characteristics in Ti-doped ZnO thin films," *Nanoscale Research Letters*, vol. 8, pp. 1–6, Apr. 2013.

[69] D. Xu, Y. Xiong, M. Tang, and B. Zeng, "Coexistence of the bipolar and unipolar resistive switching behaviors in vanadium doped ZnO films," *Journal of Alloys and Compounds*, vol. 584, pp. 269–272, Jan. 2014.

[70] J.-S. Huang, L.-M. Chen, T.-Y. Lin, C.-Y. Lee, and T.-S. Chin, "Nonpolar electrical switching behavior in cu–Si(Cu)O_x–pt stacks," *Thin Solid Films*, vol. 544, pp. 134–138, Oct. 2013.

[71] D. Xu, Y. Xiong, M. Tang, and B. Zeng, "Top electrode-dependent resistance switching behaviors of lanthanum-doped ZnO film memory devices," *Applied Physics A*, vol. 114, pp. 1377–1381, Mar. 2014.

[72] D. Ielmini, R. Bruchhaus, and R. Waser, "Thermochemical resistive switching: materials, mechanisms, and scaling projections," *Phase Transitions*, vol. 84, pp. 570–602, July 2011.

[73] F. Chudnovskii, L. Odynets, a.L. Pergament, and G. Stefanovich, "Electroforming and Switching in Oxides of Transition Metals: The Role of MetalInsulator Transition in the Switching Mechanism," *Journal of Solid State Chemistry*, vol. 122, no. 1, pp. 95–99, 1996.

[74] D. S. Jeong, R. Thomas, R. S. Katiyar, J. F. Scott, H. Kohlstedt, a. Petraru, and C. S. Hwang, "Emerging memories: resistive switching mechanisms and current status.," *Reports on progress in physics. Physical Society (Great Britain)*, vol. 75, p. 076502, July 2012.

[75] J. J. Yang, J. Borghetti, D. Murphy, D. R. Stewart, and R. S. Williams, "A Family of Electronically Reconfigurable Nanodevices," *Advanced Materials*, vol. 21, pp. 3754–3758, Oct. 2009.

[76] A. Janotti, J. Varley, P. Rinke, N. Umezawa, G. Kresse, and C. Walle, "Hybrid functional studies of the oxygen vacancy in TiO_2," *Physical Review B*, vol. 81, Feb. 2010.

[77] U. Diebold, "The surface science of titanium dioxide," *Surface Science Reports*, vol. 48, pp. 53–229, Jan. 2003.

[78] J. Nowotny, T. Bak, M. K. Nowotny, and L. R. Sheppard, "Chemical diffusion in metal oxides. example of TiO_2," *Ionics*, vol. 12, no. 3, pp. 12–227, 2006.

[79] L. Zhao, S.-G. Park, B. Magyari-Kope, and Y. Nishi, "Dopant selection rules for desired electronic structure and vacancy formation characteristics of TiO_2 resistive memory," *Applied Physics Letters*, vol. 102, p. 83506, Jan. 2013.

[80] F. A. Grant, "Properties of Rutile (Titanium Dioxide)," *Reviews of Modern Physics*, vol. 31, pp. 646–674, July 1959.

[81] S. Andersson, "Identification of Titanium Oxides by X-Ray Powder Patterns," *Acta Chemica Scandinavica*, vol. 11, pp. 1653–1657, July 1957.

[82] W. Zhang, Y. Li, S. Zhu, and F. Wang, "Surface modification of TiO_2 film by iron doping using reactive magnetron sputtering," *Chemical Physics Letters*, vol. 373, pp. 333–337, May 2003.

[83] M. Mazur, D. Kaczmarek, J. Domaradzki, D. Wojcieszak, P. Mazur, and E. Prociow, "Structural and surface properties of TiO_2 thin films doped with neodymium deposited by reactive magnetron sputtering," *Materials Science-Poland*, vol. 31, pp. 71–79, Jan. 2013.

[84] X. Zhong-Wen, X. Chen, N. Wu, and A. Ignatiev, "Bipolar resistive switching in Cr-doped TiO_2," *Chinese Physics B*, vol. 20, pp. 97703–97705, Aug. 2011.

[85] R. C. Pullar, S. J. Penn, X. Wang, I. M. Reaney, and N. M. Alford, "Dielectric loss caused by oxygen vacancies in titania ceramics," *Journal of the European Ceramic Society*, vol. 29, pp. 419–424, Feb. 2009.

[86] Y.-C. Huang, H.-M. Lin, and H.-C. Cheng, "Superior resistive switching characteristics of Cu-TiO_2 based RRAM cell," *IEEE 5th International Nanoelectronics Conference (INEC)*, pp. 236–239, Jan. 2013.

[87] L. Liu, Y. Chen, J. Kang, Y. Wang, D. Han, X. Liu, and X. Zhang, "Unipolar resistive switching and mechanism in gd-doped-TiO_2 based resistive switching memory devices," *Semiconductors Science Technology*, vol. 26, pp. 115009 (6pp)–7, Oct. 2011.

[88] J. Song, A. Inamdar, B. Jang, K. Jeon, Y. Kim, K. Jung, Y. Kim, H. Im, W. Jung, H. Kim, and J. P. Hong, "Effects of Ultrathin Al Layer Insertion on Resistive Switching Performance in an Amorphous Aluminum Oxide Resistive Memory," *Applied Physics Express*, p. 091101(4pp), Aug. 2010.

[89] D. L. Xu, Y. Xiong, M. H. Tang, B. W. Zeng, J. Q. Li, L. Liu, L. Q. Li, S. A. Yan, and Z. H. Tang, "Bipolar resistive switching behaviors in Cr-doped ZnO films," *Microelectronic Engineering*, vol. 116, pp. 22–25, Mar. 2014.

[90] M. Lanza, G. Bersuker, M. Porti, E. Miranda, M. Nafria, and X. Aymerich, "Resistive switching in hafnium dioxide layers: Local phenomenon at grain boundaries," *Applied Physics Letters*, vol. 101, no. 19, p. 193502, 2012.

[91] M. H. Lee and C. S. Hwang, "Resistive Switching Memory: Observations with Scanning Probe Microscopy," *Nanoscale*, vol. 3, pp. 490–502, Jan. 2011.

[92] F. Nardi, D. Deleruyelle, S. Spiga, C. Muller, B. Bouteille, and D. Ielmini, "Switching of Nanosized Filaments in NiO by Conductive Atomic Force Microscopy," *Journal of Applied Physics*, vol. 112, p. 064310, Jan. 2012.

[93] U. Celano, Y. Yin Chen, D. J. Wouters, G. Groeseneken, M. Jurczak, and W. Vandervorst, "Filament Observation in Metal-Oxide Resistive Switching Devices," *Applied Physics Letters*, vol. 102, no. 12, p. 121602, 2013.

[94] K. Terabe, T. Hasegawa, T. Nakayama, and M. Aono, "Quantized Conductance Atomic Switch," *Nature*, vol. 433, no. 1, pp. 47–50, 2005.

[95] I. Valov, I. Sapezanskaia, A. Nayak, T. Tsuruoka, T. Bredow, T. Hasegawa, G. Staikov, M. Aono, and R. Waser, "Atomically Controlled Electrochemical Nucleation at Superionic Solid Electrolyte Surfaces," *Nature Materials*, vol. 11, no. 6, pp. 530–535, 2012.

[96] B. J. Choi, D. S. Jeong, S. K. Kim, C. Rohde, S. Choi, J. H. Oh, H. J. Kim, C. S. Hwang, K. Szot, R. Waser, B. Reichenberg, and S. Tiedke, "Resistive switching mechanism of TiO_2 thin films grown by atomic-layer deposition," *Journal of Applied Physics*, vol. 98, no. 3, p. 033715, 2005.

[97] R. Münstermann, J. J. Yang, J. Strachan, G. Medeiros-Ribeiro, R. Dittmann, and R. Waser, "Morphological and electrical changes in TiO_2 memristive devices induced by electroforming and switching," *physica status solidi (RRL) - Rapid Research Letters*, vol. 4, pp. 16–18, Feb. 2010.

[98] B. R. Dittmann, R. Muenstermann, I. Krug, D. Park, T. Menke, J. Mayer, A. Besmehn, F. Kronast, C. M. Schneider, and R. Waser, "Scaling Potential of Local Redox Processes in Memristive $SrTiO_3$ Thin-Film Devices," *Proceedings of the IEEE*, vol. 100, no. 6, pp. 1979–1990, 2012.

[99] Y. Kim, J. H. Jang, S.-J. Park, S. Jesse, L. Donovan, A. Y. Borisevich, W. Lee, and S. V. Kalinin, "Local probing of electrochemically induced negative differential resistance in TiO_2 memristive materials," *Nanotechnology*, vol. 24, p. 085702 (8pp), Jan. 2013.

[100] B. Singh, B. R. Mehta, D. Varandani, A. V. Savu, and J. Brugger, "Cafm investigations of filamentary conduction in Cu_2O reram devices fabricated using stencil lithography technique," *Nanotechnology*, vol. 23, pp. 495707(10pp)–11, Nov. 2012.

[101] L. Yang, C. Kuegeler, K. Szot, A. Ruediger, and R. Waser, "The influence of copper top electrodes on the resistive switching effect in TiO_2 thin films studied by conductive atomic force microscopy," *Applied Physics Letters*, vol. 95, no. 1, p. 013109, 2009.

[102] R. Muenstermann, T. Menke, R. Dittmann, and R. Waser, "Coexistence of filamentary and homogeneous resistive switching in fe-doped $SrTiO_3$ thin-film memristive devices," *Advanced materials*, vol. 22, pp. 4819–4822, Nov. 2010.

[103] C. Moreno, C. Munuera, X. Obradors, and C. Ocal, "The memory effect of nanoscale memristors investigated by conducting scanning probe microscopy methods," *Beilstein Journal of Nanotechnology*, vol. 3, pp. 722–730, Jan. 2012.

[104] Y. Kim, S. Kelly, A. Morozovska, E. Rahani, E. Strelcov, E. Eliseev, S. Jesse, M. Biegalski, N. Balke, N. Benedek, D. Strukov, J. Aarts, I. Hwang, S. Oh, J. S. Choi, T. Choi, B. H. Park, V. B. Shenoy, P. Maksymovych, and S. V. Kalinin, "Mechanical Control of Electroresistive Switching," *Nano Letters*, vol. 13, pp. 4068–4074, Sept. 2013.

[105] M. H. Lee, K. M. Kim, S. J. Song, S. H. Rha, J. Y. Seok, J. S. Jung, G. H. Kim, J. H. Yoon, and C. S. Hwang, "Surface redox induced bipolar switching

of transition metal oxide films examined by scanning probe microscopy," *Applied Physics A*, vol. 102, pp. 827–834, Jan. 2011.

[106] H. Schroeder and D. S. Jeong, "Resistive switching in a Pt/TiO2/Pt thin film stack – a candidate for a non-volatile ReRAM," *Microelectronic Engineering*, vol. 84, pp. 1982–1985, Sept. 2007.

[107] D. Carta, G. Mountjoy, A. Regoutz, A. Khiat, A. Serb, and T. Prodromakis, "X-ray Absorption Spectroscopy Study of TiO_{2-x} Thin Films for Memory Applications," *The Journal of Physical Chemistry C*, vol. 119, pp. 4362–4370, 2015.

[108] R. Muenstermann, T. Menke, R. Dittmann, and R. Waser, "Coexistence of Filamentary and Homogeneous Resistive Switching in Fe-Doped SrTiO3 Thin-Film Memristive Devices," *Advanced Materials*, vol. 22, pp. 4819–4822, Nov. 2010.

[109] Y.-L. Chung, P. Lai, Y.-C. Chen, and J.-S. Chen, "Schottky Barrier Mediated Single-Polarity Resistive Switching in Pt Layer-Included TiO_2 Memory Device," *Applied Materials & Interfaces*, vol. 3, pp. 1918–1924, May 2011.

[110] K. Szot, R. Dittmann, W. Speier, and R. Waser, "Nanoscale resistive switching in $SrTiO_3$ thin films," *physica status solidi (RRL) Rapid Research Letters*, vol. 1, pp. R86–R88, Mar. 2007.

[111] A. Serb, A. Khiat, and T. Prodromakis, "An rram biasing parameter optimizer," *Electron Devices, IEEE Transactions on*, vol. 62, pp. 3685–3691, Nov 2015.

[112] I. Gupta, A. Serb, R. Berdan, A. Khiat, A. Regoutz, and T. Prodromakis, "A Cell Classifier for RRAM Process Development," *IEEE Transactions on Circuits and Systems II: Express Briefs*, vol. 62, no. 7, pp. 676–680, 2015.

[113] R. Berdan, A. Serb, A. Khiat, A. Regoutz, C. Papavassiliou, and T. Prodromakis, "A μ–Controller-Based System for Interfacing Selectorless RRAM Crossbar Arrays," *IEEE Transactions on Electron Devices*, vol. 62, no. 7, pp. 2190–2196, 2015.

[114] K. Djebaili, Z. Mekhalif, A. Boumaza, and A. Djelloul, "XPS, FTIR, EDX, and XRD Analysis of Al_2O_3 Scales Grown on PM2000 Alloy," *Journal of Spectroscopy*, vol. 2015, p. 16, 2015.

[115] A. V. Naumkin, A. Kraut-Vass, S. W. Gaarenstroom, and C. J. Powell, "NIST X-ray Photoelectron Spectroscopy Database."

[116] G. Hwan Kim, J. Ho Lee, J. Yeong Seok, S. Ji Song, J. Ho Yoon, K. Jean Yoon, M. Hwan Lee, K. Min Kim, H. Dong Lee, S. Wook Ryu, T. Joo Park, and C. Seong Hwang, "Improved endurance of resistive switching TiO_2 thin film by hourglass shaped magneli filaments," *Applied Physics Letters*, vol. 98, no. 26, 2011.

[117] L. Qingjiang, I. Salaoru, C. Papavassiliou, X. Hui, and T. Prodromakis, "Memory impedance in TiO_2 based metal-insulator-metal devices," *Scientific Reports*, vol. 4, p. 6, 2014.

[118] B. Magyari-Köpe, D. Duncan, L. Zhao, and Y. Nishi, "Doping technology for rram: Opportunities and challenges," *2016 International Symposium on VLSI Technology, Systems and Applications (VLSI-TSA)*, pp. 1–2, April 2016.

[119] L. Goux, A. Fantini, G. Kar, Y. Y. Chen, N. Jossart, R. Degraeve, S. Clima, B. Govoreanu, G. Lorenzo, G. Pourtois, D. J. Wouters, J. A. Kittl, L. Altimime, and M. Jurczak, "Ultralow sub-500na operating current high-performance tin/Al_2O_3/HfO_2/hf/tin bipolar rram achieved through understanding-based stack-engineering," in *VLSI Technology (VLSIT), 2012 Symposium on*, pp. 159–160, June 2012.

[120] S. Chakrabarti, D. Jana, M. Dutta, S. Maikap, Y. Y. Chen, and J. R. Yang, "Impact of alox interfacial layer and switching mechanism in w/alox/taox/tin rrams," in *2014 IEEE 6th International Memory Workshop (IMW)*, pp. 1–4, May 2014.

[121] Y.-S. Chen, P.-S. Chen, H.-Y. Lee, T.-Y. Wu, K.-H. Tsai, F. Chen, and M.-J. Tsai, "Enhanced endurance reliability and low current operation for alox/hfox based unipolar {RRAM} with ni electrode," *Solid-State Electronics*, vol. 94, pp. 1 – 5, 2014.

[122] L.-G. Wang, X. Qian, Y.-Q. Cao, Z.-Y. Cao, G.-Y. Fang, A.-D. Li, and D. Wu, "Excellent resistive switching properties of atomic layer-deposited Al_2O_3/HfO_2/Al_2O_3 trilayer structures for non-volatile memory applications," *Nanoscale Research Letters*, vol. 10, no. 1, p. 135, 2015.

[123] H. Wu, X. Li, M. Wu, F. Huang, Z. Yu, and H. Qian, "Resistive switching performance improvement of Ta_2O_{5-x}/TaO_y bilayer ReRAM devices by inserting AlO_δ barrier layer," *IEEE Electron Device Letters*, vol. 35, pp. 39–41, Jan 2014.

[124] M. Trapatseli, A. Khiat, S. Cortese, A. Serb, D. Carta, and T. Prodromakis, "Engineering the switching dynamics of TiO_2-based RRAM with Al doping," *Journal of Applied Physics*, vol. 120, p. 025108, 2016.

[125] K. M. Kim, D. S. Jeong, and C. S. Hwang, "Nanofilamentary resistive switching in binary oxide system; a review on the present status and outlook," *Nanotechnology*, vol. 22, p. 254002, June 2011.

[126] K. M. Kim, T. H. Park, and C. S. Hwang, "Dual conical conducting filament model in resistance switching TiO_2 thin films," *Scientific Reports*, vol. 5, no. 7844, pp. 2237–2251, 2015.

[127] Y.-R. Luo, *Comprehensive Handbook of Chemical Bond Energies.* Taylor and francis Group, 2007.

[128] S. Cortese, M. Trapatseli, A. Khiat, and T. Prodromakis, "On the origin of resistive switching volatility in ni/TiO_2/ni stacks," *Journal of Applied Physics*, vol. 120, no. 6, 2016.

[129] Q. Liu, C. Dou, Y. Wang, S. Long, W. Wang, M. Liu, M. Zhang, and J. Chen, "Formation of multiple conductive filaments in the cu/zro2:cu/pt device," *Applied Physics Letters*, vol. 95, no. 2, 2009.

[130] S. K. Kim, K. M. Kim, D. S. Jeong, W. Jeon, K. J. Yoon, and C. S. Hwang, "Titanium dioxide thin films for next-generation memory devices," *Journal of Materials Research*, vol. 28, no. 3, p. 313325, 2013.

[131] S. K. Kim, W.-D. Kim, K.-M. Kim, C. S. Hwang, and J. Jeong, "High dielectric constant tio2 thin films on a ru electrode grown at 250c by atomic-layer deposition," *Applied Physics Letters*, vol. 85, no. 18, pp. 4112–4114, 2004.

[132] S. Berg and T. Nyberg, "Fundamental understanding and modeling of reactive sputtering processes," *Thin Solid Films*, vol. 476, pp. 215–230, Apr. 2005.

Appendix A

Characterisation techniques

This appendix briefly summarises the operation principles of the experimental methods that were used to carry out this study.

A.1 Reactive Sputtering

Reactive sputtering is a process in which a target of a specified chemical composition (e.g. elemental Ti) is sputtered in the presence of a mixture of gases (usually Ar and O_2) that react with the target material to form a coating with a different chemical composition (e.g. TiO_2). The deposition can be either time or thickness controlled. The deposition occurs in Argon ambient which as a noble gas exhibits very low chemical reactivity, enhances the deposition rate and sustains the oxygen plasma at a lower pressure. During the sputtering process, atoms are ejected from the metal target (cathode) under the application of a static magnetic field and they are deposited on the substrate (anode) (Figure A.1(a)).

The system comprises two magnetrons accommodating one target each that can be either DC or AC power assisted and it has the capability to sputter from one target at a time or from both targets simultaneously (dual magnetron reactive sputtering). The system is equipped with an RF plasma source that generates very dense plasma to support the coating and improve the quality of the deposited film. The sputtering process takes place in a closed chamber where a pump is used to maintain the pressure in the range of 10^{-7} mbar. The vacuum is needed in order to keep impurities away from the deposited film and also to ensure that there are enough electron-atom collisions that will preserve plasma density to high level. Figure A.1(b) illustrates the reactive sputtering system that has been used to deposit the thin films for this study.

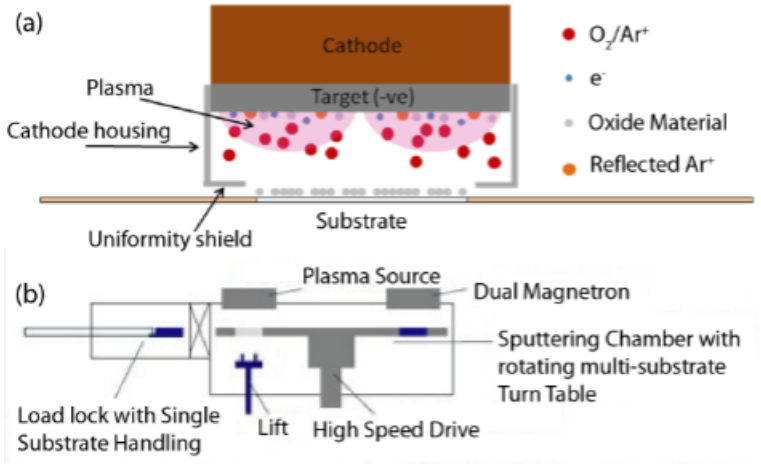

Figure A.1: (a) An illustration of the principles of Sputtering (From the Tool's WI) and (b) Helios® Plasma assisted Reactive Magnetron Sputtering system from Leybold Optics.(Courtesy of Bhler Ltd)

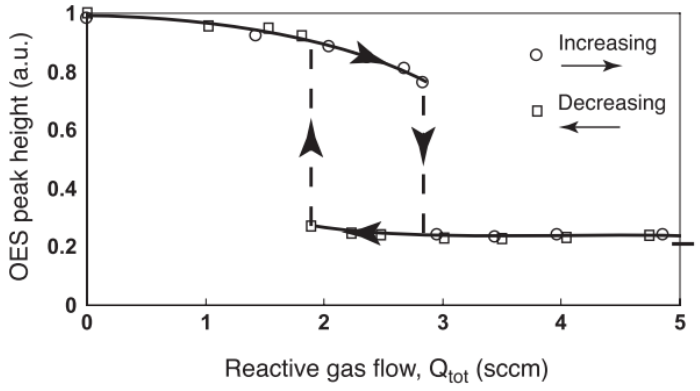

Figure A.2: Typical experimental curve for a reactive sputtering process. The optical emission (OES) from sputtered metal atoms represents the sputter erosion rate. Q_{tot} is expressed in standard cubic centimeters per minute (sccm).

By adjusting the oxygen flow, the stoichiometry of the sputtered film can be controlled. However, there is a trade-off between the deposition rate and the oxygen flow and this is illustrated as a hysteresis loop (Figure A.2) [132]. At very low oxygen flow the deposition rate is higher and the sputtered film has a more metallic character. At very high oxygen flow, the deposition rate drops because of target poisoning (compound formation on the target) but then the stoichiometry of the sputtered film improves. The process conditions should be carefully optimised so that both high deposition rate and high quality of the sputtered film is guaranteed.

A.2 Spectroscopic Ellipsometry

Ellipsometry is a powerful technique that allows the evaluation of materials properties, such as: thickness, roughness, uniformity, chemical composition, optical constants (n,k), etc. A laser beam of known polarity is incident on a surface (the one that is under examination) and it is then reflected with a different polarity (Figure A.3). The difference between the two polarities is detected by the ellipsometer and modelled by the software to give the calculated values of the properties that the user requires.

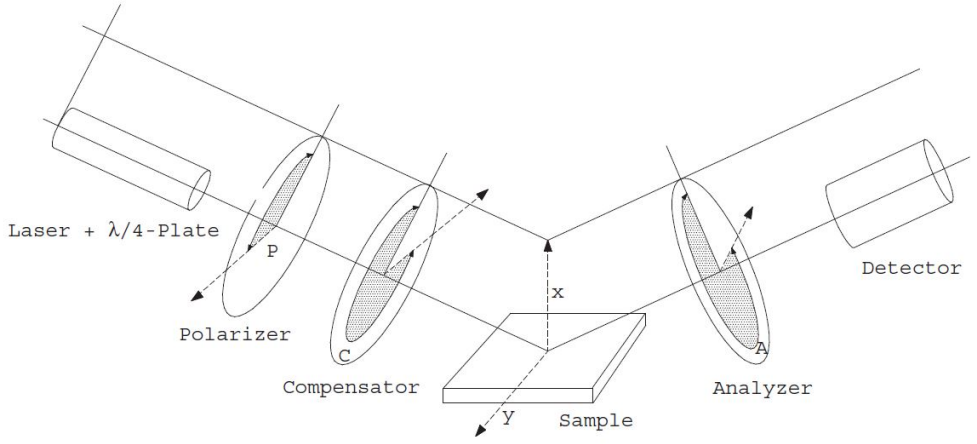

Figure A.3: A typical ellipsometry configuration, where linearly polarized light is reflected from the sample surface and the sample response is determined by measuring the polarization change. (Courtesy of J.A. Woollam Co.)

A.3 Atomic Force Microscopy (AFM)

In AFM, a probe connected to a feedback system is scanning the sample surface and can provide the user with a surface topography. The interactions between the surface and the tip of the probe are sensed and correlated to the distance between the probe and the sample. The main components of an AFM system are the probe and the scanner. While the probe intimately interrogates various qualities of the surface, the scanner controls the precise position of the probe with relation to the surface, both vertically and laterally. There are many different AFM modes, each of them tailored for studying different material properties like: magnetic properties, electrical properties and mechanical properties (elasticity, stiffness, roughness, etc).

A.3.1 Tapping Mode

Tapping mode, is usually employed to study sensitive materials, like biological specimens as in this method the probe is scanning very close to the surface by gently tapping

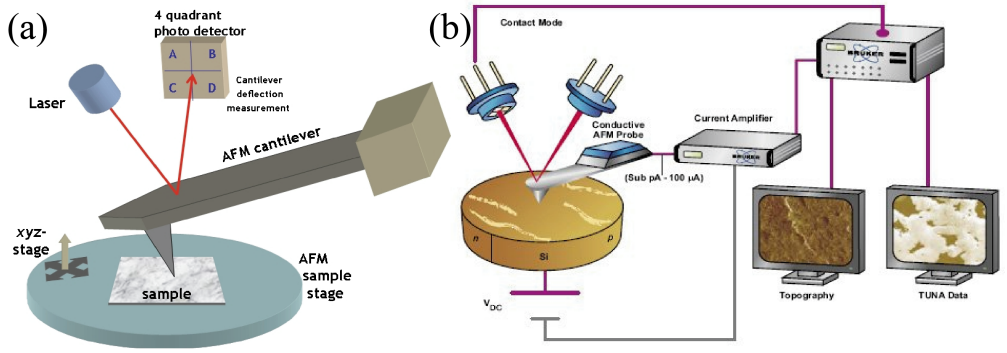

Figure A.4: An illustration of the AFM operation principle (a) in tapping mode (courtesy: Opensource Handbook of Nanoscience and Nanotechnology) and (b) conductive mode (courtesy: Brucker AFM probes)

it. The changes in the tip oscillation are monitored and at the same time controlled by the feedback loop, so that information regarding the topography are obtained (Figure A.4(a)). Another useful feature of this technique is phase imaging, which is simply the delay of the cantilever oscillation signal due to adhesion or viscoelastic properties of the material. Moreover, phase is useful in recording topometric variations on the sample (like slope), a capacity that was utilised during the characterisation of the annealed TiO_{2-x} thin films.

A.3.2 Contact Mode

In contact mode AFM, the probe is touching the sample surface. Practically it is preferred for hard surfaces as it gives good quality of topographies, however the scanning settings should be carefully optimised in order to make sure that the applied force on the tip is not scratching the sample surface. More over contact mode tips are worn out more easily because they are in constant contact with the sample surface.

A.3.3 Conductive Mode

Some AFM systems can be used in conductive mode. In that case, a metal coated tip is used and bias is applied between the sample and the tip with the later being connected to virtual ground. The response of the sample to the bias is recorded by the computer and a current map is generated simultaneously with the topography of the sample (Figure A.4(b)). This technique can be very useful with when applied to oxide thin films as the changes of the thin film resistivity can be mapped during the electrical stressing.

A.4 X-ray Photoelectron Spectroscopy

The X-ray Photoelectron Spectroscopy (XPS) is a surface sensitive technique for the analysis of surface chemistry. A typical XPS system like the one in figure A.5(a), includes a loadlock, a chamber containing a sample holder mounted on a stepper, a microscope, an X-ray gun, a flood gun, a hemispherical analyser and a detector. The operation principle of this technique is more or less the photoelectric effect (Figure A.5(b)). More precisely, the sample is exposed to soft X-ray radiation under vacuum and the ejected core electrons are filtered by the analyser with respect their energies and then collected by the detector so that the elemental composition of the surface is determined.

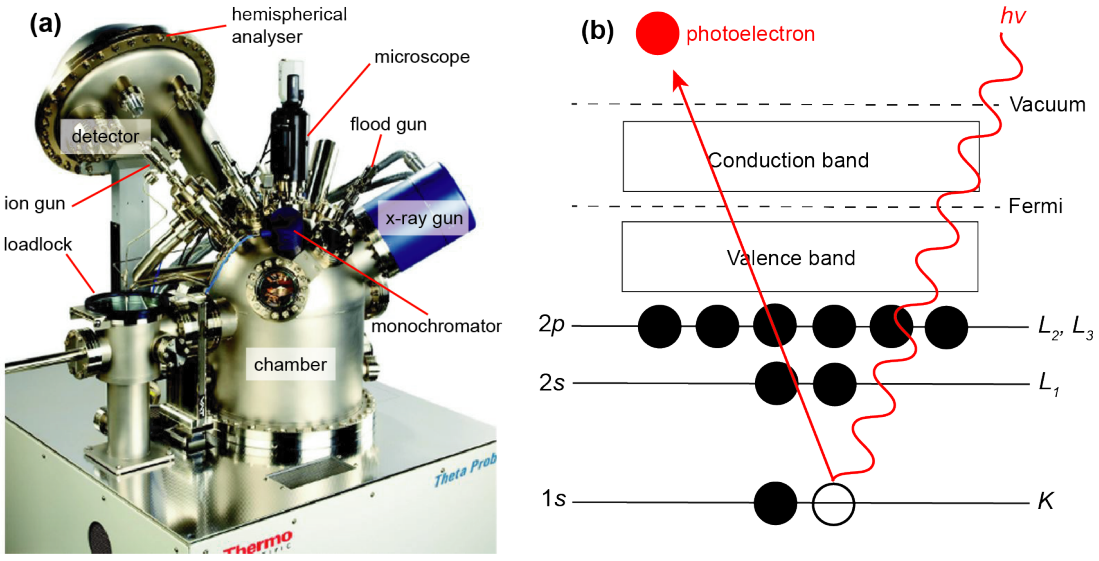

Figure A.5: (a) The Theta Probe Angle-Resolved XPS system by Thermo Scientific Inc. and (b) the XPS principle.

The core level electrons are quantised and as a result, the acquired energy spectra is exhibiting resonant peaks characteristic of the electronic states of the atoms on the surface. The sampling depth of XPS is limited to 5 nm because electrons from deeper layers of the material experience energy losses due to scattering effects. The relationship between the X-ray photons and the emitted photoelectrons is described by the equation $KE = hv - BE - \varphi$ where KE stands for the photoelectron kinetic energy, hv is the energy of the X-ray photon, BE is the binding energy of the photoelectron and φ is the work function of the X-ray gun material.

In principle, the position of the photoelectric lines represent the binding energies of the core electronic states. When the environment of these atoms change, e.g. coordination, these photoelectric lines shift accordingly. The sample resistivity can be an issue with this technique as the emitted photoelectrons are leaving accumulated static charge on the surface. If the charge supply is not fast enough, a retarding field is created acting on

the electrons escaping the surface. As a result the photoelectric peaks are shifted and the collected data are not trustworthy. Charge compensation methods are used when the samples are insulating, like metal clamps or flood gun. As XPS is a quantitative technique, the number of electrons that are recorded for a given transition is proportional to the number of atoms on the surface. In that sense, the spectra can be analysed and quantified so that information for the exact chemical composition of the sample is extracted.

List of Publications

Journal publications

1. S. Stathopoulos, A. Khiat, **M. Trapatseli**, S. Cortese, A. Serb, I. Valov, T. Prodromakis, "Multibit memory operation of metal-oxide bi-layer memristors," *Scientific Reports*, vol. 7, no. 1, pp. 17532, 2017. DOI: 10.1038/s41598-017-17785-1.

2. L. Michalas, **M. Trapatseli**, S. Stathopoulos, S. Cortese, A. Khiat, T. Prodromakis, "Interface Asymetry Induced by Symmetric Electrodes on Metal-Al: TiO_x-Metal Structures," *IEEE Transactions on Nanotechnology*.2017. DOI: 10.1109/TNANO.2017.2777698.

3. **M. Trapatseli**, S. Cortese, A. Serb, A. Khiat, T. Prodromakis, "Impact of ultrathin Al_2O_{3-y} layers on TiO_{2-x} ReRAM switching characteristics," *Journal of Applied Physics*, vol. 121, no. 18, pp. 184505, 2017. DOI: 10.1063/1.4983006.

4. S. Cortese, **M. Trapatseli**, A. Khiat, T. Prodromakis, "On the origin of resistive switching volatility in Ni/TiO_2/Ni stacks," *Journal of Applied Physics*, vol. 120, no. 6, pp. 065104, 2016. DOI: 10.1063/1.4960690.

5. **M. Trapatseli**, A. Khiat, S. Cortese, A. Serb, D. Carta, T. Prodromakis, "Engineering the switching dynamics of TiO_x-based RRAM with Al doping," *Journal of Applied Physics*, vol. 120, no. 2, pp. 025108, 2016. DOI: 10.1063/1.4958672.

6. **M. Trapatseli**, D. Carta, A. Regoutz, A. Khiat, A. Serb, I. Gupta, T. Prodromakis, "Conductive Atomic Force Microscopy Investigation of Switching Thresholds in Titanium Dioxide Thin Films," *The Journal of Physical Chemistry C*, vol. 119, no. 21, pp. 11958–11964, 2015. DOI: 10.1021/acs.jpcc.5b01672.

Conference publications

1. L. Michalas, **M. Trapatseli**, S. Stathopoulos, S. Cortese, A. Khiat, T. Prodromakis, "Effects of electrodes on the electrical properties of Al:TiO_x thin films for ReRAM applications," International Conference on Memristive Materials, Devices & Systems (MEMRISYS 2017), Athens, Greece, 2017.

2. S. Cortese, **M. Trapatseli**, A. Khiat, T. Prodromakis,"Heat-dependent effects in Bipolar Resistive Switching," International Conference on Memristive Materials, Devices & Systems (MEMRISYS 2017), Athens, Greece, 2017.

3. S. Cortese, **M. Trapatseli**, A. Khiat and T. Prodromakis, "A TiO_2-based volatile threshold switching selector device with 10^7 non linearity and sub 100 pA off current," in *2016 International Symposium on VLSI Technology, Systems and Application (VLSI-TSA)*, pp. 1–2, Hsinchu, Taiwan, 2016. DOI: 10.1109/VLSI-TSA.2016.7480484.

4. **M. Trapatseli**, A. Khiat, A. Serb, D. Carta, and T. Prodromakis,"Al doping Engineered Electroforming and Switching Dynamics of TiO_x ReRAM devices," European Materials Research Society (EMRS Spring Meeting 2016), Lille, France, 2016.

5. **M. Trapatseli**, A. Khiat, A. Serb, D. Carta, and T. Prodromakis,"Al doping Engineered Electroforming and Switching Dynamics of TiO_x ReRAM devices," European Materials Research Society (EMRS Spring Meeting 2016), Chania, Greece, 2016.

6. **M. Trapatseli**, D. Carta, A. Regoutz, A. Khiat, A. Serb, I. Gupta and T. Prodromakis,"Conductive Atomic Force Microscopy Investigation of Switching Thresholds in Titanium Dioxide Thin Films," European Materials Research Society (EMRS Spring Meeting 2015), Lille, France, 2015.